Broadband intense THz fields from laser plasma interactions

Anastasios D. Koulouklidis

Department of Materials Science and Technology
University of Crete

This dissertation is submitted for the degree of
Doctor of Philosophy

Heraklion, 13th December 2016

Acknowledgements

First and foremost I would like to express the deepest appreciation to my supervisor Professor Stelios Tzortzakis for his guidance and support during all these years of my PhD thesis. His unwavering enthusiasm for physics and his constant encouragement kept me constantly engaged with my research. Without his guidance and persistent help this dissertation would not have been possible.

I would like to especially thank Maria Massaouti for her help during my first year in the lab. Her guidance was valuable and l gained knowledge that helped me during my experimental work. Thank you Maria.

My appreciation also extends to another member of my scientific committee, Professor Dimitris Papazoglou. He was always ready to invest time to discuss with me about life and science while at the same time he was willing to help with any technical problems that came up.

I would like to thank my co-authors Andrei Gorodetsky and Vladimir Fedorov for their help and theoretical support on this work making the direct comparison between experiment and theory possible.

Among my present and past colleagues I would like to especially thank Paris Panagiotopoulos, Christiana Alaxandridi, Andreas Lemonis and Lampros Papoutsakis for the help they provided me and for all the laughs we had throughout these years.

Furthermore, I would like to thank Mixalis Loulakis for his guidance during my first training in the lab. Thanks to him, the maintenance of the laser system made our experimental work easier. But apart from this he proved to be a good and trustworthy friend. Thank you Mixalis.

I also wish to sincerely thank Christina Daskalaki. We started together this journey and she has been a great collaborator in the lab and a real friend in life. The support and the encouragement that she provided me during these years were priceless. Christina, many thanks to you, for everything.

I would also like to thank all my friends. Those here in Heraklion for all the great moments we had in Crete but also those in the rest of Greece for the joy and the fun we had despite the distance.

Last but not least, I would like to thank my parents, Daniel and Anna and my sister Vicky. They have always been there standing by me and constantly providing their support.

Abstract

The THz frequency range is one of the most interesting regions of the electromagnetic spectrum. THz radiation lies between the far-infrared and the microwave region, in a frequency interval from 0.1 THz to 75 THz. Historically, this part of the spectrum remained in the dark and it was known as the "THz gap" due to the lack of coherent sources in this frequency range. Nevertheless since the last two decades numerous works have been done on coherent sources and making it possible to access the THz frequency region of the electromagnetic spectrum and reveal its unique properties.

Many non-metallic and non-polar materials are transparent to THz radiation, while at the same time THz radiation is non-ionizing (photon energies of few meV) and is absorbed heavily by water. Apart form water, many other molecules have strong absorption features in this frequency range, due to vibrational and rotational transitions. These transitions are specific to each molecule exhibiting this way fingerprints which allow their spectroscopic identification. These unique properties of this radiation, suggest the development of promising applications ranging from spectroscopic characterization materials to imaging for medical and security reasons.Moreover, nowadays sources capable to produce intense THz pulses are available paving the way towards nonlinear studies and electron acceleration to relativistic velocities taking advantage of the high field strength and long wavelengths.

This dissertation is focused on the generation of intense, broadband THz pulses through laser plasma interactions. The scheme used is two-color filamentation in air, under which the fundamental and the second harmonic of an ultrashort pulsed laser are combined and focused into air forming a filament, which produces intense THz pulses in the far field. We propose a comprehensive physical model explaining the conical character of broadband terahertz generation from such sources while at the same time we experimentally investigate its validity by tuning in a controlled way the emission properties. To fully characterize our sources, we devise a method to reconstruct broadband THz wavepackets that are strongly distorted during propagation in dispersive and lossy media. Our approach implements an experimental procedure along with an algorithm that allows one to gain access to the lost information of the THz pulse.

Beyond the characterization of the sources we propose novel approaches to enhance the THz emission. These include,firstly the use of abruptly autofocusing beams for generating strong THz beams at well-defined remote locations, having first verified the required harmonics generation from such beams. We show that indeed, such a beam can lead to efficient THz generation resulting in a 5.3-times enhanced THz wave pulse energy compared to normal Gaussian-beam-induced plasma under the same conditions. We believe this work will inspire a new direction for controlling THz radiation from laser-induced plasma and pave the way for THz remote spectroscopy. Secondly, THz emission through two color filamentation scheme in transparent solids is for the first time studied. We present our experimental results that verify the above statement. Finally, we examine how the effect of the repetition rate of the excitation laser source can affect the plasma and consequently the THz emission. We present an enhancement of 70% in the emitted THz amplitude for higher repetition rates.

Table of contents

Chapter 1

Introduction

1.1 Basics of THz radiation

Terahertz (THz) radiation (1 THz= 10^{12}Hz) is the electromagnetic radiation covering the region of the spectrum between infrared and microwave, typically, 30 µm - 3 mm in wavelength or 0.1 - 10 THz in frequency and can be seen in Fig. 1.1. The corresponding photon energy ranges from 0.4 meV to 120 meV, while an equivalent black body radiation covers temperatures between 4 K to 1200 K. Historically, THz technologies were used mainly within the astronomy community for studying the background of cosmic far-infrared radiation and by the laser-fusion community for the diagnostics of plasmas. Traditionally, THz is known as too high frequency to be generated by solid-state devices because the wavelength is too

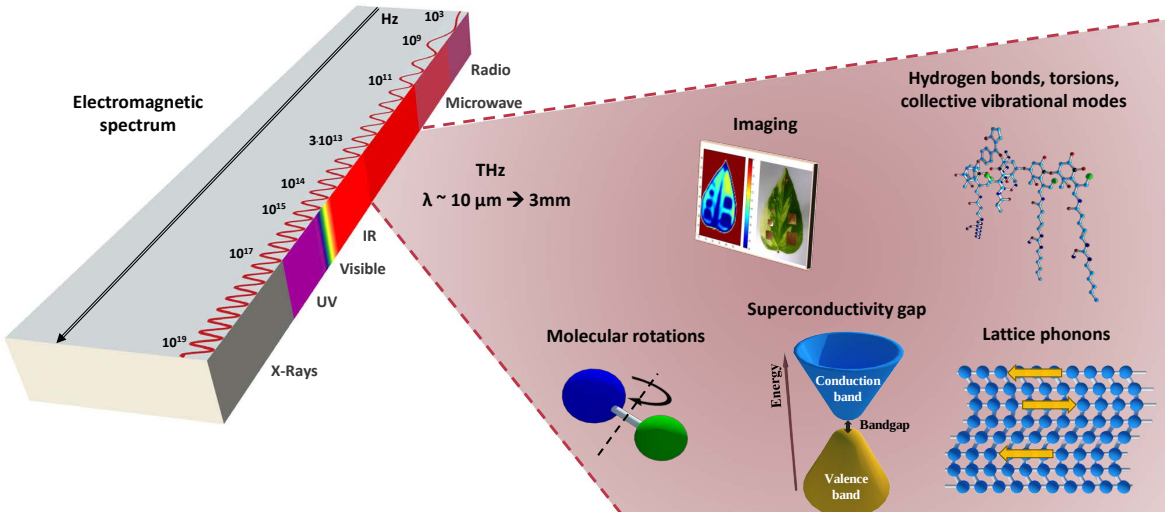

Fig. 1.1 The electromagnetic spectrum in frequency. The THz region is depicted in dark red and some of its potential applications and corresponding spectroscopic modes are presented.

long for any thermal devices to emit the radiation effectively while on the other hand, the electron velocities prevent electronic devices to operate above a few hundred GHz. Because of this lack of adequate sources, the THz band has remained one of the most untapped and least understood regions of the electromagnetic spectrum, compared to the relatively well developed science and technology in the microwave and optical frequencies [1, 2]. In order to overcome the above limitations, two approaches for practical THz generation have been established, up-conversion and down-conversion. In microwave communities, efforts have been made to up-convert the frequency from multi-GHz to THz while on the other hand, photonics scientists have been struggling to achieve THz frequencies by down-conversion for many decades. Assisted by the development of femtosecond lasers since the 1980s [3], broadband THz generation and detection has become more accessible in the laboratory [4]. Moreover, various materials have been developed for THz filters, wave plates and polarizers [5] resulting into THz technologies that are now widely applied to study various phenomena in physical, chemical and biological systems filling this way the so called "THz gap" on the electromagnetic spectrum [6].

1.1.1 THz waves properties

Various THz applications can be found from pure science to industry [6]. Metals are highly reflective at THz frequencies due to their high electrical conductivities. However, dielectric materials such as paper, plastics, clothes, wood, and ceramics, usually opaque at optical wavelengths, are transparent at THz frequencies because THz waves are less affected by Mie scattering due to their long wavelengths. In addition, THz waves have low photon energy which prevents them from ionizing biological tissues unlike X-rays [7]. Moreover, THz radiation is strongly absorbed by water since it can excite rotational modes in water molecules [8], preventing it from penetrating the human body. These properties make THz radiation an excellent tool for imaging applications and non-invasive THz screening [9, 10]. Apart form water, many other molecules have strong absorption features in this frequency range, due to vibrational and rotational transitions. These transitions are specific to each molecule exhibiting this way fingerprints which allow their spectroscopic identification [11–13]. In general, THz pulses can be coherently detected, by the sampling measurement of their electric field giving a direct access to the amplitude and the phase of the radiation. Thus, simultaneous acquisition of absorption and dispersion of many materials is easily established [14, 15].

For security purposes, detection systems which can image inside closed boxes or envelopes and even identify unknown materials by using these THz spectroscopic fingerprints already exist, while under the same working principle many airports are equipped with THz

body scanners, contributing to flight safety [16–18]. Food industry also benefits from the unique properties of THz radiation. During the last years there has been a constantly growing concern among regulatory agencies and consumers about the wide use of drugs, such as antibiotics, in animal breeding, and the potential presence of these residues in related food products. THz spectroscopy is a simple and sensitive technique that could potentially be used for quality control directly on the production line [19–21].

Numerous of solid state phenomena also lie within the THz range. For example the band gaps of superconductors, the phonon modes of most semiconductors and crystals have frequencies in the THz region [22–24]. In addition, THz pump-probe experiments and nonlinear THz studies can reveal carrier dynamics in semiconductors or provide a material's unique properties such as the transient dielectric constant [25, 26]. In addition, many natural phenomena occur at the THz frequency range. For simple molecules such as carbon monoxide, the transition frequency between its rotational levels lies at THz frequencies while for much bigger and complicated molecules such as proteins, the timescales of their vibrational motions are on the order of picoseconds, corresponding to THz periods [27, 28]. THz radiation is also applied to study wave packet dynamics of Rydberg atoms as the binding energy of their electrons is of the order of meV, corresponding to THz photon energies [29].

Finally, recent developments for the generation of intense THz source have enabled many new applications spanning from THz-enhanced attosecond pulse generation [30] to switching and controlling of magnetic domains [31–33]. Also there is a strong interest in electron acceleration using strong THz pulses. The desire to realize electron acceleration schemes that can surpass the approximately 50 MeV/m maximum acceleration gradient of conventional radio-frequency (RF) technology has spurred much research into the use of alternative regions of the electromagnetic spectrum [34] in order to achieve higher accelerating gradients. Electron accelerators driven with optical or infrared sources have demonstrated accelerating gradients orders of magnitude above that achievable with conventional RF structures [35, 36]. However, laser-driven wakefield accelerators require intense femtosecond sources and direct laser-driven accelerators suffer from low bunch charge, sub-micron tolerances and sub-femtosecond timing requirements due to the short wavelength of operation [37]. On the other hand, Terahertz-driven accelerating structures can enable high-gradient electron/proton accelerators with simple accelerating structures, high repetition rates and significant charge per bunch. Thus there is a growing interest on using such structures driven by intense THz pulses as linear accelerators taking advantage of their long wavelength combined with their GV/m field possible with optically generated THz sources [38]. Such accelerators eventually could be used to generate relativistic electron beams and using more intense THz sources will be able to reach GeV/m accelerating gradients. As shown in the examples above,

the generation of intense THz radiation is of considerable interest in many academic and industrial areas.

1.2 THz generation mechanisms

Despite a wide range of applications and needs, there have not been many suitable sources for THz study. But during the last years, there has been notable progress in developing tabletop intense THz pulse sources by taking advantage of femtosecond lasers. Such sources include ultrafast photoconductive antennas, optical rectification in nonlinear crystals and plasma based sources, and are widely adopted techniques in the THz community.

1.2.1 THz generation from photo conductive antennas

The use of photoconductive antennas (PC) is probably the most widely used method for the generation of THz pulses. A PC antenna consists of two metal electrodes that are deposited on a semi-insulating semiconductor substrate with a gap between these two electrodes.To generate THz pulses a voltage is applied across the electrodes. Since the substrate is semi-insulating, electric energy is stored in the gap area. Ultrafast laser pulses act like transient switches to open this reservoir of electric energy and release it in the form of THz pulses. When a PC antenna made of semiconductor is exposed to light, there is an increase of the number of free carriers generated by photons and thus its photoconductivity is increased [39]. The photon energy must be large enough to overcome the bandgap of the material.

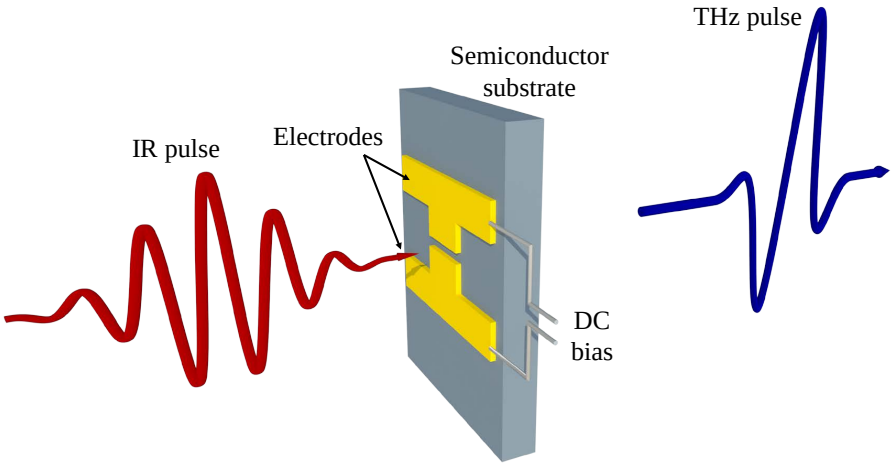

Fig. 1.2 A biased photoconductive antenna illuminated by an ultrashort pulse generating THz pulses.

Figure 1.2 illustrates the THz pulse emission from a PC antenna. The femtosecond laser pulses with photon energy larger than the bandgap of the material generate free electrons

and holes in the gap between two electrodes. Then, those free carriers can be accelerated by the DC bias. The charge density decreases on the time scale of carrier lifetime because of the trapping of carriers in the defects. Since electrons usually have much higher mobility than holes, the contribution of holes can be ignored in most cases. The time-varying current arising from the acceleration and decay of free carriers generates sub-picosecond pulses of electromagnetic radiation. The current density is then described as:

$$J(t) = N(t)e\mu E_b \tag{1.1}$$

where N is density of photocarriers, e denotes the elementary charge, μ is the mobility of electron, and E_b is the bias electric field. The photocarrier density N is a function of time, whose format is determined by the laser pulse shape and the carrier lifetime. Since the photocurrent varies in time, it generates an electromagnetic pulse, whose electric field is approximately [40]:

$$E_{THz} = \frac{1}{4\pi\varepsilon_0}\frac{A}{c^2 z}\frac{\partial J(t)}{\partial t} = \frac{Ae}{4\pi\varepsilon_0 c^2 z}\frac{\partial N(t)}{\partial t}\mu E_b \tag{1.2}$$

where A is the gap area illuminated by the laser source and z is the distance from the source to the detection point. Equation 1.1is derived by assuming the field point is located at normal to the PC antenna and the distance between the field point and the source is much larger than the dimension of the PC antenna. The THz pulse energy comes from the electric energy stored across the gap rather than the optical pulse energy. In principle, the pulse energy of THz radiation is not limited by the pulse energy of excitation laser and optical to THz quantum conversion efficiency greater than one is possible. However, the pulse energy of THz radiation has a very immediate relationship with the excitation laser pulse energy. In fact the excitation acts as a trigger to release the stored energy into THz radiation. The more photocarriers being generated, the more stored energy is converted into THz radiation. Under weak excitation condition, pulse energy of the THz wave is proportional to pulse energy of the excitation laser. In reality, linear relationships between the biased field and THz field, as well as between the excitation pulse energy and THz field, is only true under weak excitation and low bias field. When the substrate of the PC antenna is excited, it is no longer a semi-insulating material, but rather a conductive medium. As a result, the induced field screens the biased field, and the photo current is modified:

$$J(t) = \frac{\sigma(t)E_b}{\frac{\sigma(t)n_0}{1+n}+1} \tag{1.3}$$

where σ is the conductivity of the substrate, n_0 denotes the impedance of air, which is $n_0 = 377\Omega$, and n is the refractive index of the substrate. The substrate conductivity σ is induced by the excitation laser, and can be considered as $\sigma \propto I_0$ where I_0 is the laser intensity. Combining the last two equations gives:

$$E_{THz} \propto \frac{d\sigma(t)}{dt} \frac{1}{[1+\frac{\sigma(t)n_0}{1+n}]^2} \propto \frac{I_0}{(1+kI_0)^2} \tag{1.4}$$

Here $k = \kappa(t)n_0/(1+n)$, where $\kappa(t)$ denotes the ratio between $\sigma(t)$ and I_0.The above equation clearly shows that when the excitation laser is strong enough, the impedance of the substrate becomes comparable to the air, and the THz field becomes saturating to the excitation laser power. Increasing the bias field also has a limitation, since a high electric field may cause dielectric breakdown in the substrate. Breakdown of a PC antenna in THz wave generation can be grouped into two categories: field induced breakdown and thermal induced breakdown. Field induced breakdown happens when the biased field is higher than the breakdown field of the semiconductor material (i.e. $4x10^5$V/cm for GaAs). It usually happens instantly with field-induced avalanche. Thermal induced breakdown is caused by heating of the substrate by photocurrent flow in the substrate (as well as photon absorption of the excitation laser). Heating of the substrate reduces its resistance, which leads to even higher current flow. The thermal induced breakdown is a slow process, and usually takes seconds to even minutes.

As shown in Eq. 1.2, the THz yield depends on the substrate properties and electrode size/design. Although there have been interesting reports on maximizing the THz yield using large area photoconductors or multiple arrays antennas, the output is relatively small compared to other methods including optical rectification or two-color laser mixing in air [41][42]. Its performance depends on many factors. The substrate material, the geometry of the active area, the geometry of antenna, and the excitation laser pulse are some of them. Materials with a short carrier lifetime, such as low-temperature grown gallium arsenide (LT-GaAs) or doped silicon, are usually selected as the substrate in order to increase the response speed of the PC antenna. The response speed is essential to generate and detect THz pulses containing high frequency components. The carrier lifetime of LT-GaAs is in the sub-picosecond range, which results from a high concentration of defects. This ultrashort carrier lifetime which determines the switch-off time of the PC antennas is essential for THz pulse generation. The switch-on time of PC antennas is determined by the function of the laser pulse duration. Higher carrier mobility is also a desired attribute since it results in the high efficiency of THz wave generation. High dark resistance is required for the substrate in order to have sufficient breakdown voltage across the antenna. The active area of the PC

antenna, which is the gap area with laser excitation, is another crucial aspect of a PC antenna, since that is the active area to generate and detect THz waves. Careful design of the field distribution in the gap can increase the breakdown field and allow the PC antenna to generate more intense THz pulses. Distribution of excitation light within the gap is also important. PC antennas with smaller gaps are more sensitive, especially when low excitation power is used. However, larger gaps allow higher excitation power and bias voltage to be applied on the PC antenna, thus generating higher power THz waves. Larger active area can also help to lower the screening effect. Shape of the antenna is crucial to optimize coupling of THz waves between the device and free space. In terms of frequency response, various antennas are divided into two groups: resonant and non-resonant antennas. The former has a resonant frequency, which emits THz waves around a certain central-frequency. The dipole-antenna is the most widely used resonant antenna, which emits THz waves with a central wavelength of $\lambda_n = 2L/m$. Here λ_n is wavelength in the substrate, and the response wavelength in the free space is $\lambda = \lambda_n n$, where n is refractive index of the substrate. L denotes the width of the antenna from one side of the anode to the other side of the cathode and m can be any positive integer. A non resonant antenna has a variable width, and leads to a broader frequency response range. Geometries of a non resonant antenna include bowtie, spiral, and logarithmic periodic antennas. Optics, such as hyper-hemispherical silicon lenses are very often used to enhance the coupling efficiency.

1.2.2 THz generation through optical rectification

THz radiation can be generated through optical rectification (OR) in non-centrosymmetric crystals using infra-red (IR) femtosecond pulses. It is a process where a series of difference frequency generation (DFG) processes occur between components of the same pulse. Optical rectification is a second-order nonlinear optical effect. Typically, femtosecond laser pulses are used to generate THz radiation from electro-optic (EO) crystals via this scheme. Because a femtosecond pulse is a broadband pulse (many frequency components), any two frequency components contribute to the difference-frequency generation, and the overall result is the weighted sum of all the contributions. One femtosecond laser pulse is enough to stimulate optical rectification radiation, making the experimental implementation quite easy as can be seen in Fig 1.3. Mathematically, the polarization P can be expanded into a power series of the electric field E [43]:

$$\boldsymbol{P(t)} = \chi^{(1)}(t)\boldsymbol{E(t)} + \chi^{(2)}(t)\boldsymbol{E(t)E(t)} + \chi^{(3)}(t)\boldsymbol{E(t)E(t)E(t)}\ldots \tag{1.5}$$

where $\chi^{(n)}(t)$ is the nth-order nonlinear susceptibility tensor. Optical rectification comes from the second term of the above equation. If the incident light is plane wave, then E can be expressed as:

$$\mathbf{E(t)} = \int_0^\infty E(\omega) exp(-i\omega t) d\omega + c.c \ldots \tag{1.6}$$

By substituting the second equation into the first one, the polarization for optical rectification is given by:

$$\begin{aligned} P_{OR}^{(2)} &= 2\chi^{(2)} : \int_0^\infty \int_0^\infty E(\omega_1) E^*(\omega_2) exp[-i(\omega_1 - \omega_2)t] d\omega_1 d\omega_2 \\ &= 2\chi^{(2)} : \int_0^\infty \int_0^\infty E(\omega + \Omega) E^*(\omega) exp[-i(\Omega)t] d\Omega d\omega \end{aligned} \tag{1.7}$$

where Ω is the frequency difference of two optical frequency components. In the far field, the radiated electric field $E_r(t)$ is proportional to the second derivative of $P_{OR}^{(2)}$ with respect to time t:

$$E_r(t) \propto \frac{\partial^2}{\partial^2 t} P_{OR}^{(2)}(t) \tag{1.8}$$

The crystal structure affects the susceptibility tensor $\chi^{(2)}$. The far-field waveform of the radiation can be calculated using the above equation for a given crystal structure and incident light. Radiation efficiency, waveform, and frequency distribution are strongly affected by many factors, such as material, orientation and thickness of the crystal as well as absorption, dispersion, diffraction, phase matching, and saturation. The most important factor for a nonlinear process such as THz generation from optical rectification is phase matching. Only when phase matching is satisfied, all three waves participating in the optical rectification process can keep in phase and lead to maximum energy conversion along the light propagation. Phase mismatch leads to a phase walk off while propagating. The coherence length is defined by the interaction length when the phase change reaches π:

$$\delta \kappa L_c = \pi. \tag{1.9}$$

Where $\delta\kappa = \kappa_1 - \kappa_2 - \kappa_{THz}$. To generate THz efficiently from a bulk crystal, the thickness of the crystal cannot be selected longer than the coherence length in order to avoid conversion cancellation due to phase mismatch. Since the optical pulse has a much higher frequency than the THz pulse, the THz pulse only sees the profile of the optical pulse rather than the oscillations. This means phase matching is satisfied in THz wave generation when the group velocity of the optical beam equals phase velocity of the THz beam. To have maximum energy conversion, the optical pulse should have a constant temporal delay according to the THz pulse along the entire interaction length.

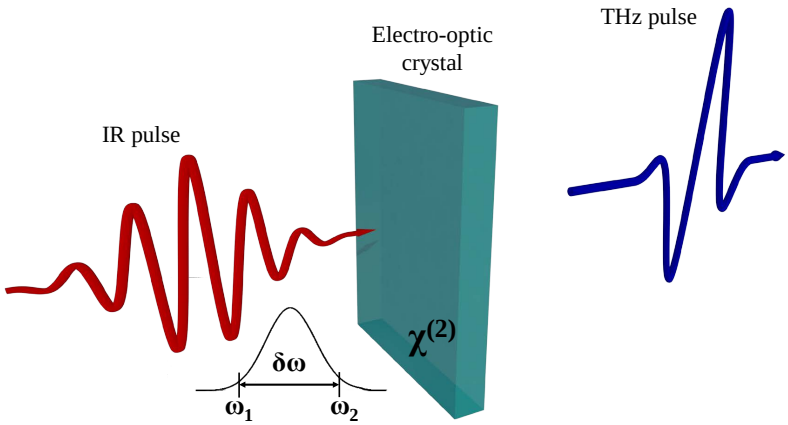

Fig. 1.3 THz pulse generated through optical rectification in a non-linear crystal.

According to the excitation wavelength and properties of the nonlinear material, optical rectification can happen under three different conditions. If the photon energy of the excitation beam is higher than the band gap of the nonlinear material, the optical beam will be absorbed within a fairly short distance. In this case, usually phase matching is not very important, since the interaction range is much shorter than the coherence length. Even with a short absorption distance, there is typically strong THz generation due to a resonating enhanced nonlinear process. When the photon energy is less than the band gap of the nonlinear material, the excitation laser is able to propagate through the nonlinear crystal for a long distance. THz generation is also different with different phase matching conditions. If phase matching is satisfied in optical rectification, the generated THz field will continually increase along the entire length of the nonlinear crystal. Therefore, strong THz wave generation is expected. If phase matching is not satisfied, generated THz waves will be canceled after each coherence length and THz radiation efficiency will be low. Only THz waves generated within a very short range close to both surfaces of the nonlinear crystal may not have been fully canceled due to velocity mismatch between the optical and THz pulse. In this case, two THz pulses with reverse polarity may be observed. When selecting nonlinear crystals for THz wave generation, three major factors need to be considered: nonlinearity of the material, absorption of both optical and THz waves in the material, and the coherence length of the optical rectification process. To obtain maximum conversion efficiency from pump light to THz radiation, it is important to select proper crystal cutting and orientation. Zinc telluride (ZnTe) and gallium phosphide (GaP) are some of the common materials used to realize OR-based THz sources because phase matching can be achieved using a collinear geometry for 800 nm and 1 μm, respectively. In [44], generation of 1.5 μJ THz pulses from a large-aperture ZnTe crystal was demonstrated. However, both crystals exhibit large two-photon absorption of the IR due to their relatively small band gap, which places an upper limit to the conversion

efficiency. Organic crystals can have very large nonlinearities. THz generation efficiencies of up to 3% have been demonstrated in DAST, OH1 and DSTMS crystals [45][46][47]. Though, pumping with longer wavelengths (1.2-1.5 um) is required in order for the coherent length to be maximized.

Another popular material for THz generation is lithium niobate (LN) LiNbO3 which has low THz absorption, large bandgap, large damage threshold, and high nonlinearity [48]. Unfortunately, the phase matching condition is far from ideal since the THz phase index in LN is significantly mismatched to the IR group index. This means that the THz wave generated in a LiNbO3 crystal by a femtosecond laser pulse is lagging behind the pulse, forming a "Cherenkov" cone of THz radiation. A well-known analogy of the Cherenkov radiation is the sonic boom of a supersonic object: as the object, or the source of the sound waves, moves faster than the waves, the collapsed waves form a shock front in the shape of a cone. The shock wave is emitted under a constant angle θ_c with the object trajectory, given by $cos\theta_c = u_{wave}/u_{object}$. Similarly, in a LiNbO3 crystal, a femtosecond laser pulse with a small beam size acts like a point source moving faster than the THz waves. It is obvious that alternative phase matching techniques are required. Quasi-phase-matching by propagation through periodically poled (PP) material (e.g. PPLN) [49] or by laser beam shaping [50][51] has achieved efficiencies of up to 0.045%, but the THz pulses produced are multiple cycle instead of single cycle, limiting the peak in-tensity.

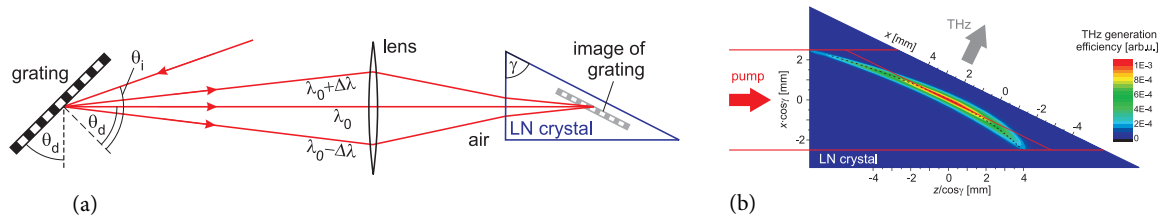

Fig. 1.4 (a) Pulse front tilt setup (b) spatial distribution of THz generation efficiency [52].

The tilted-pulse-front-pumping (TPFP) technique proposed by Hebling et al. [53] and presented in Figure 1.4, is the predominant method of phase matching OR in LN. With the use of a diffraction grating, the intensity pulse front of the femtosecond laser is tilted relative to the propagation direction in an angle is equal to the Chrenkov angle ($\theta_c \simeq 63^o$). The THz wave will coherently build up and achieve a long interaction length, leading to extremely efficient conversion.

1.3 THz waves detection

Just as there are many different methods for generating THz radiation, there are also a number of different ways in which THz waves can be detected. THz detection systems can be divided into two categories, the incoherent and the coherent detection systems. The first ones allow only the signal's amplitude detection and are broadband detection systems such as pyroelectric detector, bolometer, Golay cells. Their main advantage is the relative operation simplicity without the need of adjustment in wide frequency band. The later ones allow detecting not only the amplitude of the signal but also its phase such as heterodyne receiver, photoconductive antennas, electro-optic sampling and Air Biased Coherent Detection (ABCD). This feature is important from the point of view of increasing the information received from the object under study. It also allows us to realize higher detector sensitivity and spectral resolution characteristics.

1.3.1 Pyroelectric detection

Pyroelectricity is the ability of certain anisotropic materials to generate an electrical voltage when they are heated or cooled. Their change in temperature modifies the positions of the atoms within the crystal structure, such that the polarization of the material changes. This change in polarization may be observed as an electrical signal if electrodes are placed on opposite faces of a thin slice of the material to form a capacitor as is shown in Figure 1.5 The sensor will only produce an electrical output signal when there will be a change in the

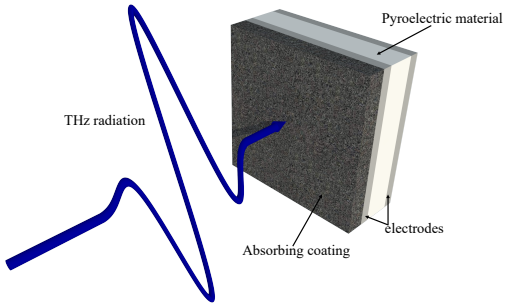

Fig. 1.5 Pyroelctric detection of THz radiation.

temperature. If the temperature stays constant, the pyroelectric voltage gradually disappears due to leakage current. Pyroelectric effect is sensitive only to heat, not to wavelength and wavelength selection is made through selection of appropriate window material.

Finally, pyroelectricity can be visualized as one side of a triangle, where each corner represents energy states in the crystal: kinetic, electrical and thermal energy. The side connecting the thermal and electric energies represents the pyroelectric effect. The side connecting the electrical and mechanical energies represents the piezoelectric effect and the side linking mechanical and thermal energies represents the thermo-electric effect. For terahertz applications that do not require high sensitivity, pyroelectric detectors have been offered [54]. Ferroelectric materials such as Lithium Tantalate, exhibit a large spontaneous electrical polarization varying with temperature.

1.3.2 Heterodyne detection

Heterodyne detection is a coherent detection method by non-linear mixing with radiation of a reference frequency. In this method, a weak input signal which is most commonly either radio waves or light is mixed with some strong local oscillator wave which is the reference signal. Then the input signal and the local oscillator are superimposed at a frequency mixer. The mixer, which is commonly a (photo-) diode, has a non- linear response to the amplitude,

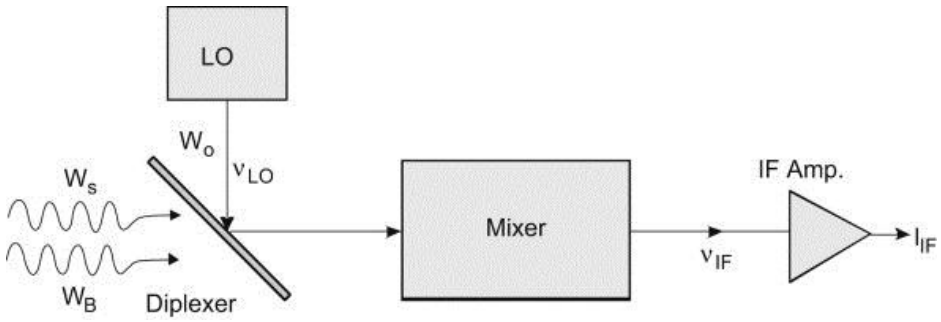

Fig. 1.6 Heterodyne detection of THz waves

that is, at least part of the output is proportional to the square of the input. Finally, the resulting mixing product is then detected, often after filtering out the original signal and the local oscillator frequency. A schematic representation of a heterodyne detection system is illustrated in Figure 1.6. The received signal can be represented as:

$$E_{sig}\cos(\omega_{sig}t+\phi) \tag{1.10}$$

and the signal from the local oscillator can be represented as:

$$E_{LO}\cos(\omega_{LO}t) \tag{1.11}$$

Approximately, the output I of the detector is proportional to the square of the amplitude:

$$I \propto \left(E_{sig}\cos(\omega_{sig}t+\phi)+E_{LO}\cos(\omega_{LO}t)\right)^2 \tag{1.12}$$

The output I of the detector has high frequency ($2\omega_{sig}$ and $2\omega_{LO}$) and constant components. In heterodyne detection, the high frequency components and usually the constant components are filtered out, leaving the intermediate frequency at ω_{sig}-ω_{LO}. The amplitude of this last component is proportional to the amplitude of the signal radiation. With appropriate signal analysis the phase of the signal can be recovered as well.

1.3.3 Photoconductive antennas

Photoconductive antennas are widely used not only for generating THz radiation but also for their coherent detection. For this purpose, a photoconductive antenna with an identical structure to an antenna emitter can be used as shown in Figure 1.7. The only major difference

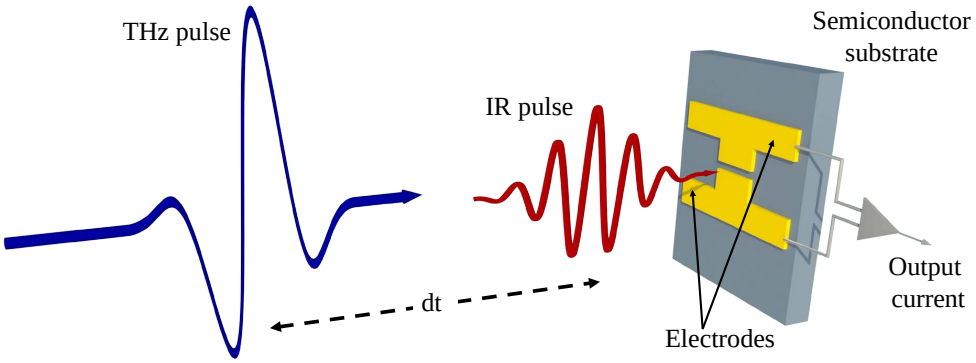

Fig. 1.7 THz detection using photoconductive antenna.

is that as a detector, the two electrodes of the antenna are connected to a current sensor in order to measure the transient current generated by an optical pulse and biased by the THz field. In the THz detection system by controlling the time delay between the THz pulse and the optical probe pulse, the electric field across the strip line of the photoconductive antenna at any given time is sampled by the optical probe pulse which serves to generate transient photo carriers in the substrate at that specific time. This measurable average current is in the order of several hundred picoamperes down to tens of nanoamperes. The induced THz field current is[40]:

$$\overline{J} = \overline{N}e\mu E(\tau) \tag{1.13}$$

Here $\overline{N}$ denotes the average electron density, and τ is the temporal delay between probe and the THz pulse. By scanning the temporal delay, the THz pulse waveform, as a function of τ,

is recorded. Typically the period of the THz oscillation is about one picosecond (ps). The measurement provides information not only about the amplitude, but also for the phase of the THz pulse.

1.3.4 Electro-optic sampling

Electro-optical (EO) sampling can be considered as a reciprocal process of the optical rectification. In EO sampling, the THz field is measured by modulating a probe laser beam inside an EO crystal, where it changes the polarization ellipsoid of the refractive index of the EO crystal [55–57]. The linearly polarized probe beam co-propagates inside the crystal with the THz beam, and its phase is modulated by the refractive index change induced by the electric field of the THz pulse. The existance of the THz field changes the birefringence of the EO crystal, i.e. causing the refractive index difference for polarizations along different axes of the crystal. The electric field induced birefringence changes polarization of the probe beam. This polarization change is converted to intensity change by an analyzer, for example a Wollaston prism. Usually a pair of balanced photodiodes is used to suppress the common laser noise while the signal is doubled. For a zincblade crystal, such as ZnTe, when an electric field is applied, its ellipsoid of the refractive index is

$$\frac{x^2+y^2+z^2}{n_o^2}+2\gamma_{41}E_x yz+2\gamma_{41}E_y xz+2\gamma_{41}E_z xy=1 \tag{1.14}$$

where n_o is refractive index of the crystal without electric field, x,y,z are coordinate units of the ellipsoid, and E_x,E_y,E_z are applied electric field along corresponding axes, respectively. γ_{41} is EO coefficient of the crystal. A phase delay Γ can be calculated according to change of the refractive index

$$\Gamma=\frac{2\pi d}{\lambda}\Delta n \tag{1.15}$$

where $d$is thickness of the EO crystal and $\Delta n$is difference between long and short axes of the ellipsoid. Here the process is assumed to be phase matched. If only normal incidence is considered. The phase delay in (100), (110), and (111) orientation ZnTe crystal is

$$\Gamma=\begin{cases} 0 & \text{for (100) crystal} \quad (1.16a)\\ \dfrac{\pi d n_o^3\gamma_{41}E}{\lambda}\sqrt{1+3\sin^2\phi} & \text{for (110) crystal} \quad (1.16b)\\ \dfrac{\pi d n_o^3\gamma_{41}E}{\lambda}\sqrt{\dfrac{8}{3}} & \text{for (111) crystal} \quad (1.16c)\end{cases}$$

In linear EO processes, the field induced phase delay is proportional to the applied electric field; thus, the EO coefficient of certain EO crystals can be represented by half wave field E_π of the crystal, which is defined as the minimum electric field which gives π phase delay in certain EO crystal with unit thickness. As a result, the maximum phase delay a THz field may generate in the EO crystal is

$$\Gamma = d\pi \frac{E_{THz}}{E_\pi} \tag{1.17}$$

There are two most commonly used methods to measure phase delay of the probe laser beam. They are cross and balanced measurement. The latter one gives higher signal and directly measures the field of the THz field, while the former method is simpler in experimental setup. Figure 1.9 shows the concept of balanced measurement. A linearly polarized probe beam

	ZnTe	GaAs	InP	GaP	ZnS
E_π ($l = 1$ mm) (kV/cm)	89.0	161	153	252	388
Field sensitivity (mV/cm$\sqrt{\text{Hz}}$)	3.20	5.80	5.51	9.07	12.2
NEP (10^{-16}W/Hz)	0.27	0.89	0.80	2.2	5.2
V_{TO} (THz)	5.3	8.0	10.4	11	10.8
$\sqrt{\varepsilon}$	3.18	3.63	3.54	3.34	2.88
N	2.85	3.63	3.54	3.18	2.32
Phase-matching wavelength (nm)	822	1,405	1,230	1,030	470
Frequency of TO photon (THz)	5.3	7.6	10.0	10.8	9.8

Fig. 1.8 Properties of various electro optic crystals.

is modified to elliptical polarization through the EO process. A quarter-waveplate is used to bias the polarization of the probe beam, which can be put either in front of or after the EO crystal. An analyzer is used to split the biased probe beam into s and p polarization components. A pair of balanced photo detectors is used to measure difference in s and p polarization components. When no THz field is applied, s and p polarization components will

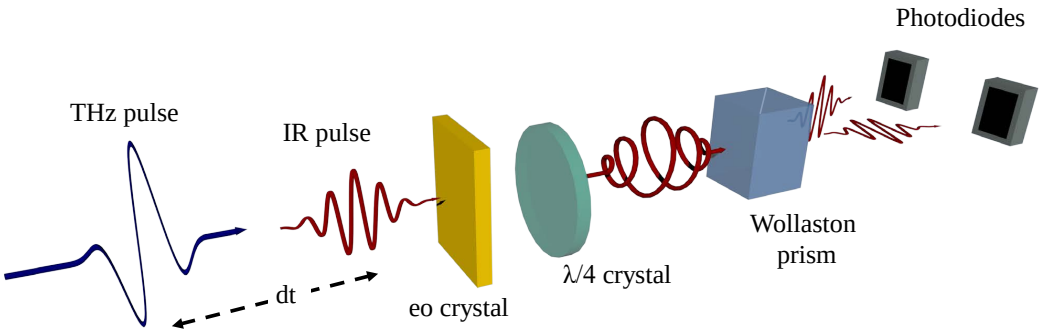

Fig. 1.9 THz detection using balanced detection method

have the same intensity after the analyzer; therefore, the balanced detector gives no signal. The presence of a THz electric field changes polarization of the probe beam, generating a measurable signal in the balanced detector. If the input beam is x polarized, then the output light can obtained by the following expression

$$\begin{pmatrix} E_X \\ E_y \end{pmatrix} = \begin{pmatrix} \cos\frac{\pi}{4} & -\sin\frac{\pi}{4} \\ \sin\frac{\pi}{4} & \cos\frac{\pi}{4} \end{pmatrix} \begin{pmatrix} \exp(\imath\Gamma) & 0 \\ 0 & 1 \end{pmatrix} \begin{pmatrix} \cos\frac{\pi}{4} & \sin\frac{\pi}{4} \\ -\sin\frac{\pi}{4} & \cos\frac{\pi}{4} \end{pmatrix} \begin{pmatrix} E_0 \\ 0 \end{pmatrix} \tag{1.18}$$

The signal of the balanced detector is

$$S = I_0 \sin 2\phi \sin\Gamma \approx I_0 \Gamma \sin 2\phi \tag{1.19}$$

where I_0 is intensity of the probe laser and ϕ is the angle between probe beam polarization and the long axis of ellipsoid induced by THz field. Equation (1.19) indicates that, in a balanced measurement, the signal is linearly proportional to the electric field of the THz radiation but at higher level of electric field, the linear proportionality does not hold anymore.

A cross measurement is similar to balanced measurement except there is no quarter-wave-plate. The analyzer is set cross-polarized to the polarizer located before the EO crystal. Probe beam leaking through the analyzer is detected using a single optical detector. Without THz field, in principle, probe beam does not leak through the analyzer and the recorded signal is 0. If a THz field is applied to modify the polarization of the probe beam, the leaked signal will become larger.

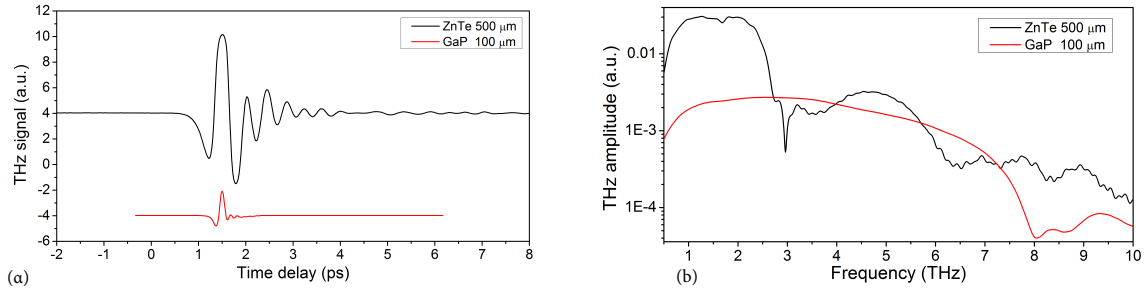

Fig. 1.10 (a) Typical THz electric fields recorded in our laboratory using electro optic detection with two different crystals, a ZnTe and a GaP with thicknesses 500 um and 100 um respectivley. (b) Their corresponding spectrum.

It is worth noticing that the above discussion on EO sampling is based on the steady electric field assumption. For a transient electric field such as a THz pulse, phase matching should be considered. Being the reciprocal process of optical rectification, EO sampling shares the same phase-matching condition. Two main factors limit the bandwidth of THz radiation in optical rectification and EO sampling: the pulse duration of the excitation laser

pulse and phase matching conditions. Another factor that also limits the useful spectrum is the transverse optical (TO) phonon resonances. In ZnTe crystals the first phonon resonance is located at 5.3 THz and in GaP at 11 THz [58]. These intense resonances apart from the absorption increase around them (which breaks the uniformity of the spectrum), they result in a rapid destruction of phase-matching limiting the detection bandwidth.

Electro optic detection is one of our main detection schemes in our laboratory. Fig. 1.10 shows a typical THz signal emitted by our two color source, as recorded using two different electro optic crystals, a 500 um ZnTe and a 100 um GaP. Since our source is ultra broadband, emitting up to 35 THz, one can clearly see the effect of the detection crystal on the recorded field and subsequently on the spectrum.

1.3.5 Air Biased Coherent Detection (ABCD)

Ambient air can be used to sense broadband terahertz waves by measuring the terahertz field induced optical second harmonic light (TFISH), generated through a third-order nonlinear process [59]. ABCD is a pump-probe technique and a schematic representation of it be seen in FIgure 1.11. A properly synchronized probe IR pulse at ω frequency is recombined with the THz pulse and are together focused in ambient air between two elctrodes that are AC biased, generating a TFISH signal which is then collected by a photomultiplier (PMT).The use of a PMT is essential since the 2ω signal generated is extremely weak.

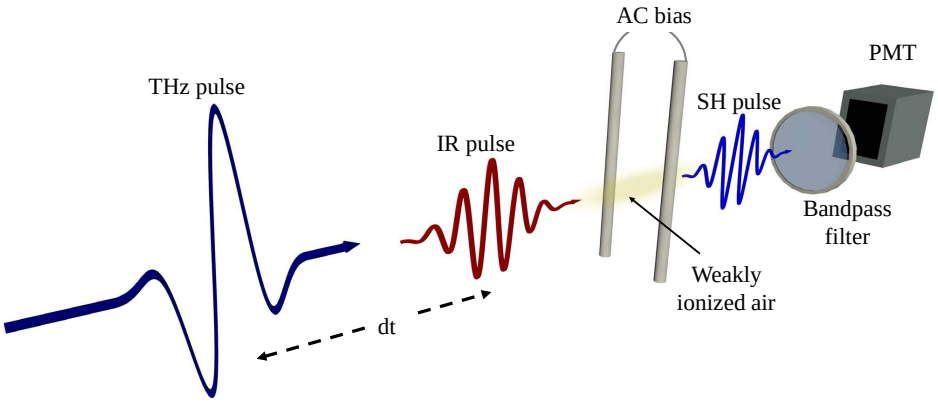

Fig. 1.11 Schematic representation of Air Biased Coherent Detection technique.

The AC bias, as will be described below, generates an extra second harmonic signal that mixes with the terahertz field induced second harmonic pulse. The second harmonic field generated by the TFISH process can be described as:

$$E_{2\omega}^{THz} \propto \chi^{(3)} E_{THz} E_{\omega} E_{\omega} \propto \chi^{(3)} E_{THz} I_{\omega} \tag{1.20}$$

where $E_{2\omega}$, E_{ω} and E_{THz} are the electric field amplitudes of 2ω, ω and terahertz waves, respectively while $\chi^{(3)}$ is the third-order susceptibility of the gas. Since $E_{2\omega} \propto E_{THz}E_{\omega}E_{\omega}$, it follows that the intensity of the second-harmonic signal measured by the PMT is proportional to the intensity of the terahertz wave: $I_{2\omega} \propto I_{THz}$. The measured signal predicted in Eq.1.20 is incoherent, therefore, the phase information is lost and that limits the possible applications of the technique.

The AC external bias that is introduced to the optical focus, generates a bias field induced second harmonic pulse that acts as a local oscillator (LO) and has a field amplitude designated by $E_{2\omega}^{LO}$ [60]. When the SH LO contribution is included into the analysis, the total SH intensity in the time average values over one period of E-field oscillation has the form:

$$I_{2\omega} \propto (E_{2\omega})^2 = (E_{2\omega}^{THz} + E_{2\omega}^{LO})^2 = (E_{2\omega}^{THz})^2 + (E_{2\omega}^{LO})^2 + 2E_{2\omega}^{THz}E_{2\omega}^{LO}cos\phi \tag{1.21}$$

where ϕ is the phase difference between the $E_{2\omega}^{THz}$ and $E_{2\omega}^{LO}$ which is either 0 or π depending on the direction of the bias field. Terahertz field induced second harmonic pulse $E_{2\omega}^{THz}$ and the AC $E_{2\omega}^{LO}$ bias induced second harmonic can be written as:

$$\begin{aligned} E_{2\omega}^{THz} &\propto \chi^{(3)} I_{\omega} E_{THz}, \\ E_{2\omega}^{LO} &\propto \chi^{(3)} I_{\omega} E_{bias} \end{aligned} \tag{1.22}$$

where E_{bias} is the bias electric field. Using the above equation, Eq.1.20 can be written as:

$$I_{2\omega} \propto (\chi^{(3)} I_{\omega})^2 (E_{THz})^2 + (E_{bias})^2 \pm 2E_{bias}E_{THz}. \tag{1.23}$$

Since the phase of the bias-induced second harmonic is modulated, the process can be interpreted in terms of heterodyne detection. Assuming a constant carrier-envelope phase of the laser pulse, the second harmonic pulses form a frequency comb. The phase modulated pulses have a frequency comb shifted by the modulation frequency and, thus, when the intensity is measured, the detector acts as a mixer, providing the difference frequencies of the two combs. Only the cross term is present at the modulation frequency, while the other terms exist only on the even harmonics and, thus, lock-in amplification easily isolates the signal proportional to E_{THz}.Under the above description the measured second harmonic intensity will be:

$$I_{2\omega} \propto 4[(\chi^{(3)} I_{\omega})]^2 E_{bias}E_{THz}. \tag{1.24}$$

and we can see that the intensity of the second harmonic pule depends now on the electric field the THz pulse allowing it this way to be coherently detected.

Interestingly, at the beginning of the techniques development [61], the white light (and specifically the 2ω component) generated from the laser-induced air plasma at the beam focus through self-phase modulation and self-steepening, was used as local oscillator. Required though more power in the probe beam in order to achieve coherent detection. The technique was called ABCD as an acronym of Air Breakdown Coherent Detection.

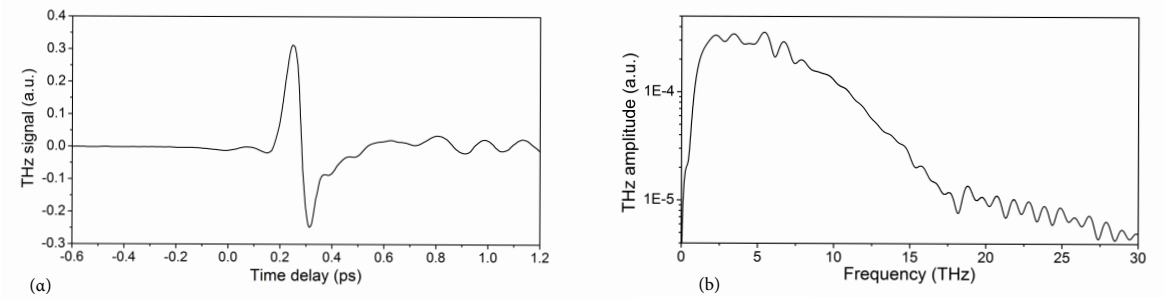

Fig. 1.12 (a) Typical THz electric field recorded in our laboratory using ABCD scheme and (b) its corresponding spectrum.

ABCD is also implemented in our laboratory as a detection technique. In Fig.1.12 (a) is shown a typical THz signal generated from our two-color plasma in air and detected through ABCD, along with its corresponding spectrum (b). From the spectrum one can see the ultra broadband nature of our source revealed by the above technique. Unlike the case of electro-optic sampling in a crystal, there are no phonon modes to introduce dispersion or absorption into the detection region. On the other hand, although ABCD is a coherent and broadband detection scheme, still has some limitations. Firstly, it is less sensitive than electro optic sampling so the SNR is lower compared to electro optic crystals and secondly, it's detection bandwidth strongly depends on the probe pulse duration.

1.3.6 THz Michelson interferometry

A detection technique capable to detect the whole THz spectrum without any limitations is Michelson interferometry. On the other hand, contrary to coherent detection methods, it cannot measure explicitly the phase of a THz pulse. A Fourier transform spectrometer is essentially a Michelson interferometer. It operates by separating the radiation from a source into two beams and then coherently recombining them to produce the output beam. A typical THz Michelson interferometer can be seen in Fig.1.13. A Si wafer or a pellicle beam splitter is used in order to create the two arms of the interferometer. while the one arm remains fixed, the other one is movable. The combined beam is then focused by an off-axis parabolic mirror into a pyroelectric detector. Interference effects are produced by varying the relative length

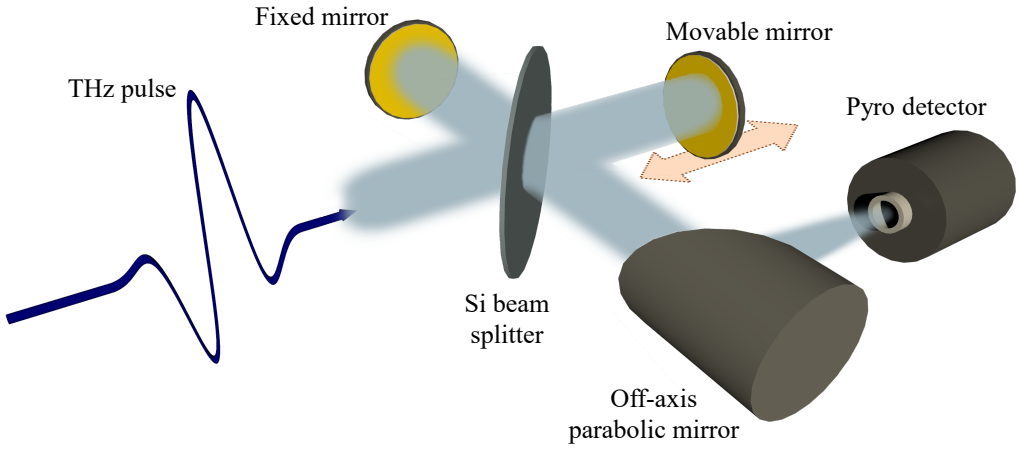

Fig. 1.13 THz Michelson interferometric setup.

of optical paths traveled by the separate beams. When used without any samples in the beam paths, the signal output of the (power) detector at a given path difference δ is [62]

$$I(\delta) \propto \int_0^\infty S(\sigma)[1+cos(2\pi\sigma\delta)]d\sigma \tag{1.25}$$

where S is the detector response at wavenumber σ $1/\lambda$. The Fourier transform of this function gives the system efficiency as a function of frequency:

$$S(\delta) \propto \int_{-\infty}^{\infty} [I(\delta) - \frac{1}{2}I(0)]cos(2\pi\sigma\delta)d\delta \tag{1.26}$$

It is thus possible to use Fourier transform spectroscopy to determine the spectral content of a THz pulse, or, by placing an object in the combined light path and measuring response ratios, to determine the spectral transmission of optical elements.

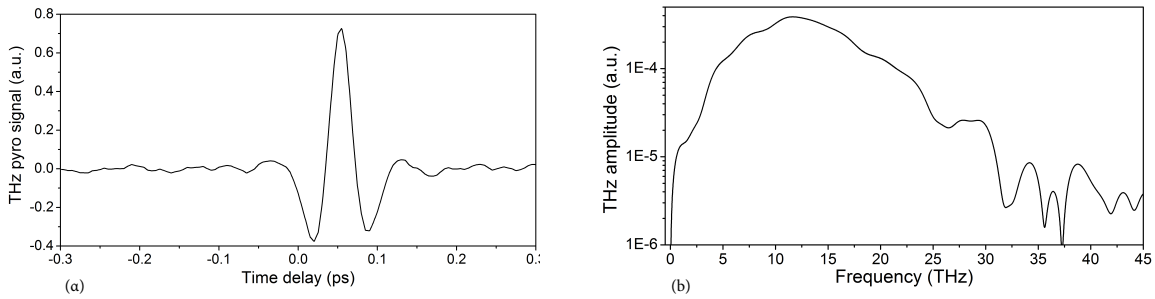

Fig. 1.14 (a)THz Michelson interferogram and (b) its spectrum after applying a Fourier transform.

Fig.1.14 shows an interferogram of a THz pulse generated from our two color source in our laboratory. As was mentioned before, the bandwidth of our source spans up to 35 THz. From the interferometric signal is obvious that the full bandwidth of the THz pulse is revealed contrary to all the other detection techniques.

1.4 High peak power sources

THz pulsed techniques were first developed for systems employing high-repetition-rate (i.e.100 MHz) fs pulse lasers. However, soon after the technique was adapted to low-repetition-rate amplified laser systems (with pulse energies typically in the uJ–mJ range) in order to gain access to higher THz pulse energies. Upon tight focusing of the THz radiation, electric fields of hundreds of KV/cm or even reaching MV/cm are now available [63] which would be sufficient to access physical phenomena in a regime where they depend nonlinearly on the electric field [64–66]. Moreover, at higher level of energy, THz pump/THz-probe

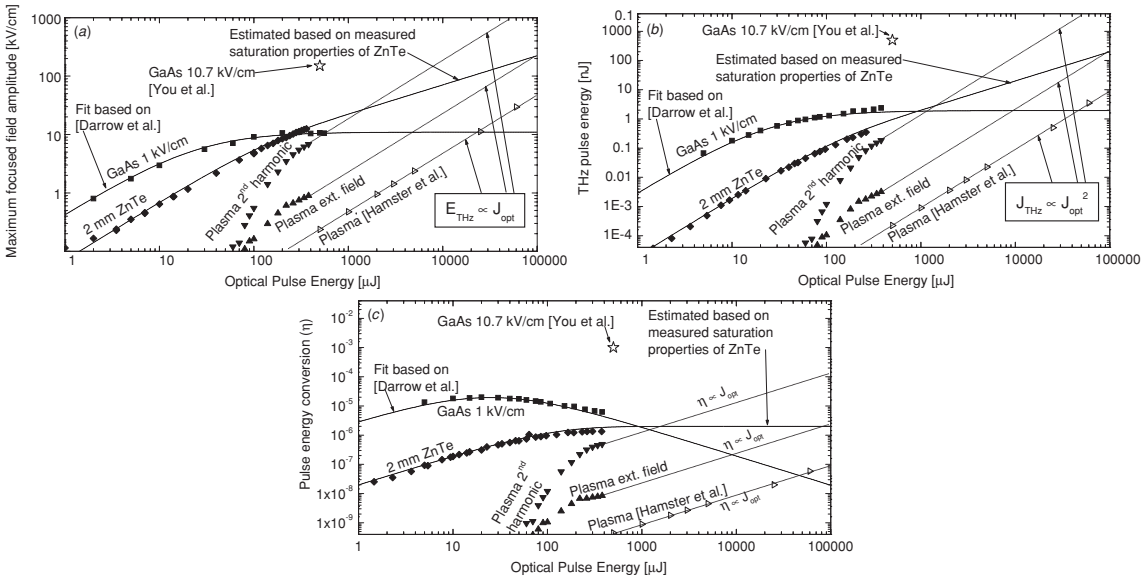

Fig. 1.15 Comparison of (a) the focused peak electric field, (b) the THz-pulse energy and (c) the energy conversion efficiency. Taken from [67].

experiments offer the ability to study various interesting phenomena in semiconductors not accessible in the past [68]. It becomes obvious that there is a strong interest towards intense THz generation. The two main generation techniques previously described in this chapter, systematically lead to saturation at certain level of laser input energy. Consequently one approach to increase the yielded THz pulse energy is to extend the size of the emitter [69, 70]. Nevertheless, scaling-up the size of the emitter does not resolve the problem of damage

threshold occurring in materials. A very different class of THz emitters which are suitable for use with amplifier laser systems is based on laser-generated plasmas [71, 72]. The basic concept of these emitters is to focus a short high-energy laser pulse alone or mixed with its second harmonic in a gaseous medium and form a plasma filament. Such THz source appears to be one of the most promising in terms of yielded THz energy [67] and is mainly used in our laboratory. The projection for higher input laser pulse energy (see Fig.1.15) clearly suggested that plasma 2nd harmonic source can reach the level of uJ per pulse something already achieved using laser pulse energies up to 60mJ [73].

1.5 Thesis outline

The work in this thesis, was performed between November 2011 and October 2016, and its purpose is twofold. Firstly, is focused on the understanding and improvement of THz sources based on two color-plasma interactions in order to control their emission properties, while at the same time valuable information lost due to detection limitations is also addressed. On the other hand, during this period, THz plasma sources seemed to reach a saturation point regarding the generation efficiency. The reason for that is that in order to scale up the energy of the THz pulses coming out from a plasma source, one needs to increase further the input laser power and ideally to switch to higher wavelengths. This implies the need of even more powerful amplified laser systems. Thus it was obvious that there was a need for different approaches towards enhancement of the emitted radiation either by tailoring the laser beam itself or by seeking for alternative media capable to retain the broadband characteristics of plasma sources. At the same time, one could take advantage of the easier plasma formation in condensed matter compared to air, along with the higher non-linear refractive index, avoiding in this way big amplified laser systems.

The rest of the thesis is organized as follows. A review of the filamentation process is presented in the beginning of Chapter 2. Continuing in the same chapter, we present a description of THz generation through two-color filamentation comparing the two main generating mechanisms. At this point, we start presenting our contribution to the field. First we propose an experimental procedure under which the dominating mechanism during THz generation through two-color filamentation can be revealed. Next, we propose a comprehensive two-dimensional model of two-color filament THz generation, that addresses shortfalls of previous proposed models and is verified by our experimental findings and various experimental findings from the literature.

Chapter 3 focuses on the detection challenges, discussing in more detail the effect of bandwidth loss of the techniques available today for coherent THz detection resulting in

significant loss of information. In order to resolve this problem, we derive theoretically the scaling laws of the THz spectral bandwidth produced from two-color laser filaments as a function of the input laser pulse duration and find the spectrum loss-less limits for electro optic detection. At the same time, a simple experimental procedure allows us to use the above laws to recover the lost information. Using our innovative approach we are able to fully restore the original THz wave packet using only electro optic detection.

The last chapters of this thesis illustrate our contribution towards the enhancement of the THz radiation emitted from plasma interactions. Specifically, in Chapter 4 we propose an alternative approach of THz generation from plasma sources that can produce enhanced THz wave pulses. This approach is based on the use of exotic beams like abruptly autofocusing (AAF) beams, in order to produce the required plasma channel. We believe that the unique characteristics of such beams, will inspire a new direction for controlling THz radiation from laser-induced plasmas and pave the way to THz remote spectroscopy. During the above work, another aspect of two-color generated plasma channels needed to be addressed. In the traditional scheme were Gaussian beams are used, mixing the fundamental with its second harmonic is a relatively easy task utilizing a beta barium borate (BBO) crystal. On the other hand, switching to exotic waves such us AAF beams, second harmonic generation in the crystal is not a trivial task. The difficulties range from the generation itself to the spatio-temporal overlap of the two beams on the plasma channel. So in the first part of the chapter, we present a study on harmonics generation of AAF beams, a work that allows us to continue with the rest of the chapter as described in the beginning.

Finally, Chapter 5 discusses preliminary studies on novel approaches for increasing the power of the THz radiation, using either solid state media or high repetition rate laser sources. Specifically, we report for the first time, THz generation through two-color filamentation in transparent solids while we investigated the effect of increasing the repetition rate of the excitation laser beam on the THz emission through laser plasma interactions in air. We observed an enhancement of 70% in the emitted amplitude of the THz radiation as the repetition rate increases from 250 Hz to 25 kHz. The perspective of the above ideas is to facilitate the generation of broadband THz pulses using high repetition rate oscillators instead of big amplified laser systems.

References

[1] Luc Vinet and Alexei Zhedanov. *Principles of Terahertz Science and Technology*, volume 7. Springer US, Boston, MA, nov 2009.

[2] Sergey Ganichev and Willi Prettl. *Intense Terahertz Excitation of Semiconductors*. Oxford University Press, dec 2005.

[3] Ch Fattinger and D. Grischkowsky. Terahertz beams. *Applied Physics Letters*, 54(6):490–492, 1989.

[4] Yong Sing You. *Physical mechanism of terahertz generation in two-color photoionization*. PhD thesis, 2014.

[5] B Ferguson and X C Zhang. Materials for terahertz science and technology. *Nature Materials*, 1(1):26–33, 2002.

[6] Masayoshi Tonouchi. Cutting-edge terahertz technology. *Nat Photon*, 1(2):97–105, 2007.

[7] B. B. Hu and M. C. Nuss. Imaging with terahertz waves. *Optics Letters*, 20(16):1716–1718, 1995.

[8] Martin van Exter, Ch Fattinger, and D Grischkowsky. Terahertz time-domain spectroscopy of water vapor. *Optics Letters*, 14(20):1128, 1989.

[9] Ruth M. Woodward, Vincent P. Wallace, Richard J. Pye, Bryan E. Cole, Donald D. Arnone, Edmund H. Linfield, and Michael Pepper. Terahertz pulse imaging of ex vivo basal cell carcinoma. *Journal of Investigative Dermatology*, 120(1):72–78, 2003.

[10] Anthony J. Fitzgerald, Bryan E. Cole, and Philip F. Taday. Nondestructive analysis of tablet coating thicknesses using Terahertz pulsed imaging. *Journal of Pharmaceutical Sciences*, 94(1):177–183, 2005.

[11] A G Markelz, A Roitberg, and E J Heilweil. Pulsed terahertz spectroscopy of DNA, bovine serum albumin and collagen between 0.1 and 2.0 THz. *Chemical Physics Letters*, 320(1-2):42–48, 2000.

[12] B M Fischer, M Walther, and P Uhd Jepsen. Far-infrared vibrational modes of DNA components studied by terahertz time-domain spectroscopy. *Physics in medicine and biology*, 47(21):3807–3814, 2002.

[13] M. Walther, P. Plochocka, B. Fischer, H. Helm, and P. Uhd Jepsen. Collective vibrational modes in biological molecules investigated by terahertz time-domain spectroscopy. In *Biopolymers - Biospectroscopy Section*, volume 67, pages 310–313, 2002.

[14] G. Méchain, Y.-B. André, S. Tzortzakis, M. Franco, B. Prade, a. Mysyrowicz, a. Couairon, E. Salmon, and R. Sauerbrey. Range of plasma filaments created in air by a multi-terawatt femtosecond laser. *Optics Communications*, 247(1-3):171–180, mar 2005.

[15] J Kasparian, M Rodriguez, G Mejean, J Yu, E Salmon, H Wille, R Bourayou, S Frey, Y.-B. Andre, A Mysyrowicz, R Sauerbrey, J.-P. Wolf, and L Woste. White-Light Filaments for Atmospheric Analysis. *Science*, 301(5629):61–64, 2003.

[16] J.B. Jackson, M. Mourou, J.F. Whitaker, I.N. Duling, S.L. Williamson, M. Menu, and G.a. Mourou. Terahertz imaging for non-destructive evaluation of mural paintings. *Optics Communications*, 281(4):527–532, feb 2008.

[17] K Kawase, Y Ogawa, Y Watanabe, and H Inoue. Non-destructive terahertz imaging of illicit drugs using spectral fingerprints. *Optics Express*, 11(20):2549–2554, 2003.

[18] John F Federici, Brian Schulkin, Feng Huang, Dale Gary, Robert Barat, Filipe Oliveira, and David Zimdars. THz imaging and sensing for security applications—explosives, weapons and drugs. *Semiconductor Science and Technology*, 20(7):S266–S280, 2005.

[19] Albert Redo-Sanchez, Gerard Salvatella, Regina Galceran, Eva Roldos, Jose-Antonio Garcia-Reguero, Massimo Castellari, and Javier Tejada. Assessment of terahertz spectroscopy to detect antibiotic residues in food and feed matrices. *Analyst*, 136(8):1733–1738, 2011.

[20] Hua Yuefang and Zhang Hongjian. Qualitative and Quantitative Detection of Pesticides With Terahertz Time-Domain Spectroscopy. *Microwave Theory and Techniques, IEEE Transactions on*, 58(7):2064–2070, 2010.

[21] Maria Massaouti, Christina Daskalaki, Andrei Gorodetsky, Anastasios D Koulouklidis, and Stelios Tzortzakis. Detection of Harmful Residues in Honey Using Terahertz Time-Domain Spectroscopy. *Applied Spectroscopy*, 67(11):1264–1269, 2013.

[22] L. Ozyuzer, a. E. Koshelev, C. Kurter, N. Gopalsami, Q. Li, M. Tachiki, K. Kadowaki, T. Yamamoto, H. Minami, H. Yamaguchi, T. Tachiki, K E. Gray, W.-K. Kwok, and U. Welp. Emission of Coherent THz Radiation from Superconductors. *Science*, 318(5854):1291–1293, 2007.

[23] T. Dekorsy, H. Auer, H. Bakker, H. Roskos, and H. Kurz. THz electromagnetic emission by coherent infrared-active phonons. *Physical Review B*, 53(7):4005–4014, 1996.

[24] A J Kreisler and A Gaugue. Recent progress in high-temperature superconductor bolometric detectors: from the mid-infrared to the far-infrared (THz) range. *Superconductor Science & Technology*, 13(8):1235–1245, 2000.

[25] M. F. Kimmitt. Restrahlen to T-rays - 100 Years of terahertz radiation. In *Journal of Biological Physics*, volume 29, pages 77–85, 2003.

[26] D. Leisawitz, W. Danchi, M. DiPirro, L.D. Feinberg, D. Gezari, M. Hagopian, J.C. Mather, S.H. Moseley, R.F. Silverberg, W.D. Langer, M. Shao, M.R. Swain, H.W. Yorke, and J. Staguhn. Far-IR/submillimeter space interferometry: scientific motivation and technology requirements. *2001 IEEE Aerospace Conference Proceedings (Cat. No.01TH8542)*, 4:4/1995–4/2004, 2001.

[27] Sharly Fleischer, Yan Zhou, Robert W. Field, and Keith A. Nelson. Molecular orientation and alignment by intense single-cycle THz pulses. *Physical Review Letters*, 107(16):1–5, 2011.

[28] Benjamin Born, Seung Joong Kim, Simon Ebbinghaus, Martin Gruebelebc, and Martina Havenith. The terahertz dance of water with the proteins: the effect of protein flexibility on the dynamical hydration shell of ubiquitin. *Faraday Discussions*, 141:161, 2008.

[29] J. Ahn, D. N. Hutchinson, C. Rangan, and P. H. Bucksbaum. Quantum phase retrieval of a Rydberg wave packet using a half-cycle pulse. *Physical Review Letters*, 86(7):1179–1182, 2001.

[30] Katalin Kovács, Emeric Balogh, János Hebling, Valer Toşa, and Katalin Varjú. Quasi-phase-matching high-harmonic radiation using chirped THz pulses. *Physical Review Letters*, 108(19), 2012.

[31] C Vicario, C Ruchert, F Ardana-Lamas, P M Derlet, B Tudu, J Luning, and C P Hauri. Off-resonant magnetization dynamics phase-locked to an intense phase-stable terahertz transient. *Nature Photonics*, 7(9):1–4, 2013.

[32] S. Baierl, M. Hohenleutner, T. Kampfrath, A. K. Zvezdin, A. V. Kimel, R. Huber, and R. V. Mikhaylovskiy. Nonlinear spin control by terahertz-driven anisotropy fields. *Nature Photonics*, (October), 2016.

[33] S. Baierl. Terahertz-Driven Nonlinear Spin Response of Antiferromagnetic Nickel Oxide. *Physical Review Letters*, 117(19):197201, 2016.

[34] Liang Jie Wong, Arya Fallahi, and Franz X Kärtner. Compact electron acceleration and bunch compression in THz waveguides. *Optics express*, 21(8):9792–806, 2013.

[35] A. J. Goers, G. A. Hine, L. Feder, B. Miao, F. Salehi, J. K. Wahlstrand, and H. M. Milchberg. Multi-MeV Electron Acceleration by Subterawatt Laser Pulses. *Physical Review Letters*, 115(19), 2015.

[36] F Salehi, A J Goers, G A Hine, L Feder, D Kuk, B Miao, D Woodbury, K Y Kim, and H M Milchberg. MeV electron acceleration at 1 kHz with <10mJ laser pulses. oct 2016.

[37] Emilio A. Nanni, Wenqian R. Huang, Kyung-Han Hong, Koustuban Ravi, Arya Fallahi, Gustavo Moriena, R. J. Dwayne Miller, and Franz X. Kärtner. Terahertz-driven linear electron acceleration. *Nature Communications*, 6:8486, 2015.

[38] Mostafa Shalaby and Christoph P Hauri. Demonstration of a low-frequency three-dimensional terahertz bullet with extreme brightness. *Nature Communications*, 6:1–8, 2015.

[39] D You, D R Dykaar, R R Jones, and P H Bucksbaum. Generation of high-power sub-single-cycle 500-fs electromagnetic pulses. *Optics Letters*, 18(4):290, 1993.

[40] Xi-Cheng Zhang and Jingzhou Xu. *Introduction to THz Wave Photonics*, volume 53. Springer US, Boston, MA, 2010.

[41] A. Dreyhaupt, S. Winnerl, T. Dekorsy, and M. Helm. High-intensity terahertz radiation from a microstructured large-area photoconductor. *Applied Physics Letters*, 86(12):1–3, 2005.

[42] M Beck, H Schäfer, G Klatt, J Demsar, S Winnerl, M Helm, and T. Dekorsy. Impulsive terahertz radiation with high electric fields from an amplifier-driven large-area photoconductive antenna. *Optics express*, 18(9):9251–9257, 2010.

[43] et all Rogério dos Santos Alves; Alex Soares de Souza. *Principles of Terahertz Science and Technology*. Number 1. Springer US, Boston, MA, 2009.

[44] F Blanchard, L Razzari, H C Bandulet, G Sharma, R Morandotti, J C Kieffer, T Ozaki, M Reid, H F Tiedje, H K Haugen, and F a Hegmann. Generation of 1.5 microJ single-cycle terahertz pulses by optical rectification from a large aperture ZnTe crystal. *Optics Express*, 15(20):13212–20, 2007.

[45] Clemens Ruchert, Carlo Vicario, and Christoph P. Hauri. Scaling submillimeter single-cycle transients toward megavolts per centimeter field strength via optical rectification in the organic crystal OH1. *Optics Letters*, 37(5):899, 2012.

[46] Clemens Ruchert, Carlo Vicario, and Christoph P Hauri. Spatiotemporal Focusing Dynamics of Intense Supercontinuum THz Pulses. *Physical Review Letters*, 110(12):123902, 2013.

[47] Christoph P. Hauri, Clemens Ruchert, Carlo Vicario, and Fernando Ardana. Strong-field single-cycle THz pulses generated in an organic crystal. *Applied Physics Letters*, 99(16):0–3, 2011.

[48] J Hebling, K L Yeh, M C Hoffmann, B Bartal, and K A Nelson. Generation of high-power terahertz pulses by tilted-pulse-front excitation and their application possibilities. *Journal of the Optical Society of America B-Optical Physics*, 25(7):B6–B19, 2008.

[49] Konstantin L Vodopyanov. Optical generation of narrow-band terahertz packets in periodically inverted electro-optic crystals: conversion efficiency and optimal laser pulse format. *Optics express*, 14(6):2263–2276, 2006.

[50] Yuri Avestisyan, Caihong Zhang, Iwao Kawayama, Hironaru Murakami, Toshihiro Somekawa, Haik Chosrowjan, Masayuki Fujita, and Masayoshi Tonouchi. Terahertz generation by optical rectification in lithium niobate crystal using a shadow mask. *Optics express*, 20(23):25752–7, 2012.

[51] Guibao Xu, Xiaodong Mu, Yujie J Ding, and Ioulia B Zotova. Efficient generation of backward terahertz pulses from multiperiod periodically poled lithium niobate. *Optics letters*, 34(7):995–7, 2009.

[52] J A Fülöp, L Pálfalvi, G Almási, and J Hebling. Design of high-energy terahertz sources based on optical rectification. *Optics express*, 18(12):12311–12327, 2010.

[53] Janos Hebling, Gabor Almasi, Ida Kozma, and Jurgen Kuhl. Velocity matching by pulse front tilting for large area THz-pulse generation. *Optics express*, 10(21):1161–1166, 2002.

[54] Don Dooley. Sensitivity of broadband pyroelectric terahertz detectors continues to improve. *Laser Focus World*, 46(5):49–53, 2010.

[55] C Kubler, R Huber, and A Leitenstorfer. Ultrabroadband terahertz pulses: generation and field-resolved detection. *Semiconductor Science and Technology*, (7):S128, 2005.

[56] Q. Wu and X.-C. Zhang. Free-space electro-optic sampling of terahertz beams. *Applied Physics Letters*, 67(24):3523, 1995.

[57] Ajay Nahata, David H Auston, Tony F Heinz, and Chengjiu Wu. Coherent detection of freely propagating terahertz radiation by electro-optic sampling. *Applied Physics Letters*, 68(2):150, 1996.

[58] S Casalbuoni, H Schlarb, B Schmidt, P Schmüser, B Steffen, and A Winter. Numerical studies on the electro-optic detection of femtosecond electron bunches. *Physical Review Special Topics - Accelerators and Beams*, 11:72802, 2008.

[59] D.J. Cook, J.X. Chen, E.A. Morlino, and R.M. Hochstrasser. Terahertz-field-induced second-harmonic generation measurements of liquid dynamics. *Chemical Physics Letters*, 309(3-4):221–228, aug 1999.

[60] Nicholas Karpowicz, Jianming Dai, Xiaofei Lu, Yunqing Chen, Masashi Yamaguchi, Hongwei Zhao, X.-C. Zhang, Liangliang Zhang, Cunlin Zhang, Matthew Price-Gallagher, Clark Fletcher, Orval Mamer, Alain Lesimple, and Keith Johnson. Coherent heterodyne time-domain spectrometry covering the entire "terahertz gap". *Applied Physics Letters*, 92(1):011131, 2008.

[61] J Dai, X Xie, and X C Zhang. Detection of broadband terahertz waves with a laser-induced plasma in gases. *Physical Review Letters*, 97(10), 2006.

[62] M. Bin, D. J. Benford, M. C. Gaidis, T H Buttgenbach, J Zmuidzinas, E Serabyn, and T G Phillips. A Large Throughput High Resolution Fourier Transform Spectrometer for Submillimeter Applications. *International Journal of Infrared and Millimeter Waves*, 20(3):1–18, 1999.

[63] Christoph P. Hauri, Clemens Ruchert, Carlo Vicario, and Fernando Ardana. Strong-field single-cycle THz pulses generated in an organic crystal. *Applied Physics Letters*, 99(16):2013–2016, 2011.

[64] Mostafa Shalaby, Carlo Vicario, and Christoph P. Hauri. High-performing nonlinear visualization of terahertz radiation on a silicon charge-coupled device. *Nature Communications*, 6:8439, 2015.

[65] Mostafa Shalaby and Christoph P Hauri. Air Nonlinear dynamics triggered by an ultraintense THz bullet. *arXiv*, 2, 2015.

[66] Dmitry Turchinovich, Jørn M Hvam, and Matthias C Hoffmann. Self-phase modulation of a single-cycle terahertz pulse by nonlinear free-carrier response in a semiconductor. *Physical Review B*, 85(20):201304, 2012.

[67] Torsten Löffler, Markus Kreß, Mark Thomson, Tobias Hahn, Noboru Hasegawa, and Hartmut G Roskos. Comparative performance of terahertz emitters in amplifier-laser-based systems. *Semiconductor Science and Technology*, 20(7):S134–S141, jul 2005.

[68] Matthias Hoffmann, János Hebling, Harold Hwang, Ka-Lo Yeh, and Keith Nelson. Impact ionization in InSb probed by terahertz pump—terahertz probe spectroscopy. *Physical Review B*, 79(16):161201, apr 2009.

[69] D You, D R Dykaar, R R Jones, and P H Bucksbaum. Generation of high-power sub-single-cycle 500-fs electromagnetic pulses. *Optics Letters*, 18(4):290, 1993.

[70] T Löffler, T Hahn, M Thomson, F Jacob, and H Roskos. Large-area electro-optic ZnTe terahertz emitters. *Opt. Express*, 13(14):5353–5362, 2005.

[71] D. J. Cook and R. M. Hochstrasser. Intense terahertz pulses by four-wave rectification in air. *Optics letters*, 25(16):1210–1212, aug 2000.

[72] H. Hamster, A. Sullivan, S. Gordon, W. White, and R. W. Falcone. Subpicosecond, electromagnetic pulses from intense laser-plasma interaction. *Physical Review Letters*, 71(17):2725–2728, 1993.

[73] T I Oh, Y S You, N Jhajj, E W Rosenthal, H M Milchberg, and K Y Kim. Scaling and saturation of high-power terahertz radiation generation in two-color laser filamentation Scaling and saturation of high-power terahertz radiation generation in two-color laser filamentation. *Appl. Phys. Lett.*, 102:201113, 2013.

Chapter 2

Laser plasma THz sources:a comprehensive study

2.1 Properties of ultrashort pulse nonlinear propagation

The propagation of electromagnetic pulses has been the subject of intense research in fundamental and applied physics. Thanks to the appearance of chirped pulse amplified laser systems in 1985 [1], the laser peak intensities have been tremendously enhanced. Since, various non-linear phenomena, which occur during the propagation of high intensity ultrashort laser pulses in air, have been observed. One of the most impressive, and unusual, phenomenon is the so-called filamentation. The first experimental observation of femtosecond laser filamentation was reported in 1995 [2]. The results indicated the presence of a self-trapped laser beam, induced by non-linearities, which persisted over a long distances in air. The formation of filaments can be described as a self-action process in which an ultrashort laser pulse, with sufficient power, undergoes strong spatial and temporal reshaping as it propagates in a transparent medium. This results in the propagation of the beam with a very narrow waist which remains almost constant over many Rayleigh lengths, leaving ionized channels in its wake. This phenomenon appears for input powers close to or above a critical value, P_{cr}. It is the result of a competition involving linear and highly nonlinear effects, such as the optical Kerr effect, defocusing due to plasma created by optical field ionization, nonlinear losses, dispersion and others [3].

2.1.1 Optical Kerr efect

In 1877, John Kerr first reported the dependence of the refractive index of a material to the strength of an applied static electric field [4]. In the field of nonlinear optics, where the static

electric field is replaced by a rapidly oscillating optical electric field from a laser, the same phenomenon is observed and is called the optical Kerr effect and it is the driving effect of femtosecond filamentation and the origin of rich nonlinear phenomena. In the presence of a strong laser field, the refractive index of air (as well as for any transparent medium) is not only dependent on the frequency of the laser field, but also on its spatio-temporal intensity distribution according to the following relation:

$$n = n_0 + n_2 I(r,t) \tag{2.1}$$

where $n_2(cm^2/W)$ is called the nonlinear refractive index of the medium and depends on the frequency of the incident wave and the material properties. Typically the nonlinear refractive index n_2 is of the order of $10^{-19} cm^2/W$ in gases and $10^{-16} cm^2/W$ in amorphous solids and liquids. Equation 2.1 reveals that the refractive index acting on any beam propagating in a nonlinear medium is dependent on the intensity profile of the beam itself. As a direct result a beam with a Gaussian intensity profile will induce a Gaussian refractive index modulation as it propagates. This refractive index modulation resembles a positive lens and will cause the beam to focus as it is shown in Fig. 2.2 (a). The focusing of the beam due to self-action effects (without any initial beam curvature), called self-focusing, was first investigated by P. L. Kelly in 1965 [5] and has been extensively studied thereafter [6]. Self-focusing of Gaussian beams is always happening in positive n_2 nonlinear media, even at very low intensities. However in order to be observable self-focusing must overcome linear diffraction. This is possible only if the power carried by the beam is above a critical value which depends on the beam shape. For Gaussian beams the critical power is given by:

$$P_{cr} = \frac{3.77\lambda_0^2}{8\pi n_0 n_2} \tag{2.2}$$

Note that the above equation is referring to the critical power value for collimated Gaussian beams only, and is independent of intensity. Typically the critical power for an 800 nm laser pulse is about 3.2 GW in air and 4 MW in water.

2.1.2 Optical field ionization

During the self-focusing process, the intensity $I(W/cm^2)$ dramatically increases to the point where it will be possible to ionize the medium. Multiphoton ionization (MPI) is the first process to occur and its rate scales as I^K, where K, the number of simultaneously absorbed photons, is approximately equal to 8 for air, at a laser wavelength 800 nm taking into account only oxygen. In liquids and condensed materials, K is in general smaller than in gases. For

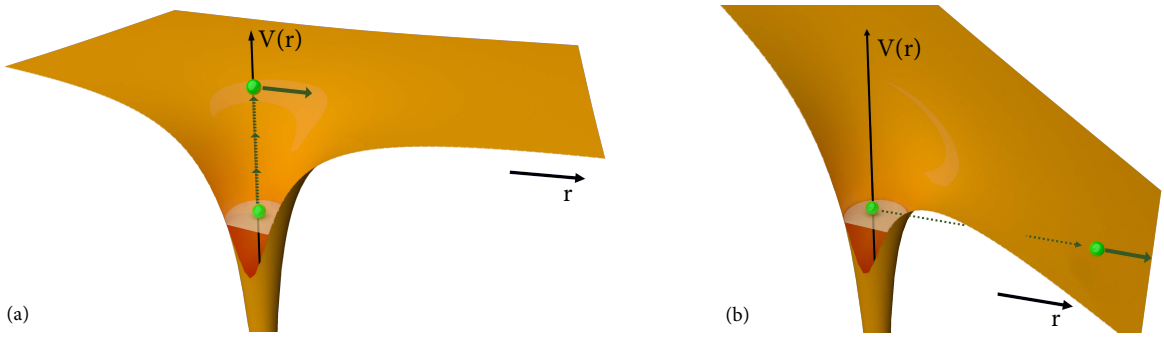

Fig. 2.1 Schematic diagram of: (a) multiphoton and (b) tunnel ionization.

the same 800 nm laser we need K = 5 photons in water, and 6 in fused silica glass in order to generate an electron. At higher intensities and shorter optical frequencies, tunnel ionization occurs where an electron escapes through the barrier formed by the electromagnetic field and the Coulomb potential. Conventionally, photoionization process can be characterized by the Keldysh parameter γ_K, described by [7]:

$$\gamma_K = \sqrt{\frac{U_i}{2U_p}} = \sqrt{\frac{t_i}{T}} \tag{2.3}$$

here U_i is the ionization potential energy of an atom or ion, $U_p = e^2E^2/4m_e\omega^2$ is the laser ponderomotive potential energy, t_i is the ionization time and T is the laser oscillation period given by $T = 2\pi/\omega$ [8, 9]. For $\gamma_K >> 1$, the ionization is dominated by the multiphoton process whereas the tunneling process is dominant for $\gamma_K < 1$. In terms of laser intensity, the multiphoton process is responsible for relatively low laser intensities $< 10^{12}W/cm^2$, whereas tunneling ionization is responsible for $10^{14}W/cm^2$. The direct effect of this plasma formation is a local reduction of the refractive index. This effect can be seen in Fig.2.2 (b) and acts as a negative defocusing lens, preventing the beam from collapsing. The index variation due to the plasma is expressed as:

$$n = n_0 - \frac{\rho(r,t)}{2\rho_c} \tag{2.4}$$

where ρ is electrons density of the generated plasma and ρ_c the critical plasma density at which the medium becomes opaque, given from:

$$\rho_c \equiv \frac{\varepsilon_0 m_e \omega_0^2}{e^2} \tag{2.5}$$

$m_e = 9.1093829140 \times 10^{-31} kg$, and $e = -1.602176565 \times 10^{-19} C$ are the electron mass and charge. For 800 nm we get $\rho_c = 1.7 \times 10^{21} cm^{-3}$.

2.1.3 Filamentation

Filamentation is the result of the dynamic equilibrium of numerous linear and nonlinear effects acting on intense ultrashort laser pulses when they propagate through transparent media. Initially linear phenomena such diffraction and dispersion are acting on the wavepacket, and given enough power the beam will start to self-focus. Self-focusing will lead to an increase of the intensity, which will in turn accelerate the self-focusing process further. Close to the point of collapse the intensity of the pulse is high enough to ionize the medium through MPI and tunneling ionization and will generate plasma arresting the collapse. Ionization will

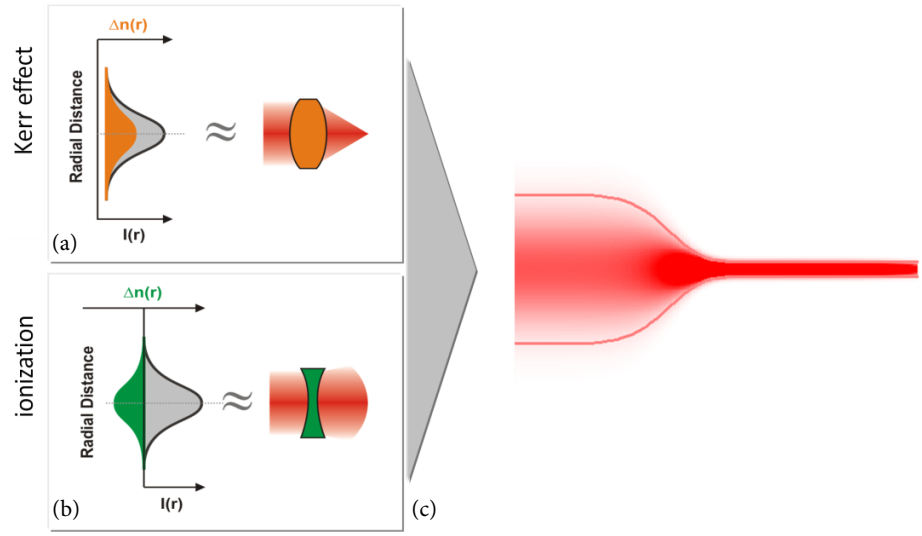

Fig. 2.2 Schematic representation of mechanisms that lead to filamentation.

locally drop the intensity, while plasma defocusing will defocus the trailing part of the pulse widening the beam. The above described nonlinear process will repeat itself if the wavepacket has enough power left to initiate a second self-focusing stage. In fact the process repeats itself multiple times, up to the point where the power carried by the wavepacket is not high enough to re-initiate a new self-focusing stage and linear effects will finally disperse the wavepacket. The schematic representation of the refocusing cycles taking place in filamention is shown in Fig. 2.2 (c). The dynamical equilibrium between these two phenomena results in the formation of a filament as schematically represented in Fig. 2.2.

Filamentation can thus be seen as a direct competition between these two phenomena. This inherently led to the concept of intensity clamping, which is the intensity that cannot be

exceeded within the filament:

$$I_{cl} \approx \left(\frac{2n_2\rho_c}{\sigma_K t_p \rho_{at}} \right)^{K-1} \tag{2.6}$$

where ρ_{at} is the density of neutral atoms and $\sigma_K$is the ionization cross section for K photons. Typically for a pulse duration of 100 fs and a wavelength of 800 nm, $I_{cl} \approx 1.8 \times 10^{13} W/cm^2$ However, this description of filamentation is rather succinct and it would be too simplistic and inaccurate to describe filamentation using such a qualitative approach. Phenomena such as self-phase modulation (SPM), self-steepening and losses related to multiphoton absorption and to plasma absorption are taking part with a lower impact on the process of filamentation. For this reason a full numerical model for pulse propagation has been developed through the years and offers a deeper insight into the filamentation process [3].

2.2 THz generation through two-color filamentation in air

Despite the relative high generation efficiency and their simple experimental implementation, all the above mechanisms are restricted by a relatively short radiation bandwidth. In THz emission through photoconductive antennas in semiconductors, the emitted spectrum does not exceed 4 THz due to the electron relaxation time of the semiconductor substrate. Optical rectification on the other hand, strongly depends on the non-linear crystal used. In particular coherence length and propagating dispersion of the THz pulse inside the crystal limit the emitted bandwidth. Using much thinner crystals and shorter laser pulse durations the emitted THz bandwidth can be greatly improved however strong phonon resonances result in a non uniform spectrum consisted of gaps.

Contrary to all the above laser plasma sources, can emit ultra-broadband intense THz pulses. Several different mechanisms can lead to THz waves generation in air. High-intensity laser pulses can easily ionize a gas resulting in a THz transient which can be formed through a coherent plasma oscillation driven by either the ponderomotive force or by transition radiation from accelerated electron bunches driven by wakefield acceleration [10]. The latter provided high-energy electrons that would emit transition radiation in the THz range when impinging on a sharp dielectric constant gradient. Electrons driven with ponderomotive force induce an oscillation primarily along the direction of the pulse propagation vector, and thus radiates in a conical pattern, while electrons driven by the wakefield provided THz radiation in the forward direction. Due to the highly nonlinear nature of the effects, they are inefficient at low intensities, and so work with more common regenerative amplifiers with kHz repetition rates required alternate methods. Such lasers are powerful enough to ionize the target gas, but using them efficiently requires a more direct method of accelerating the

electrons. Applying of a DC bias to the plasma accelerates the electrons as they are ionized, resulting in a rapidly increasing current and the radiation of a THz pulse. In this case, the direction of the photocurrent is determined by the direction of the bias field, and so it can be set to be orthogonal to the pulse propagation direction, leading to coherent build-up of the THz pulse amplitude along the plasma. Doing this led to an order of magnitude enhancement of the THz pulse amplitude over what was generated through ponderomotive acceleration alone, and was limited mainly by the strength of the applied bias, which was constricted by electrical breakdown of the gas as the field approached 30 kV/cm in the atmosphere.

An alternative method generates a strong THz pulse by combining the fundamental laser pulse with a pulse at its second harmonic frequency. During the two-color filamentation a laser beam and its second harmonic are focused together in gases, like ambient air, and produce laser-plasma filaments that emit THz radiation. Using two-color filamentation one can generate THz pulses with energies of few microjoules and with extremely broad spectra,ranging from almost zero up to approximately 60 THz [11], or even 200 THz [12], that entirely cover the terahertz gap. As an additional advantage, the two-color filamentation method allows one to generate THz radiation at remote distances [13–15], thereby solving the THz propagation issues such as high absorption in atmospheric water vapor and strong diffraction.

The first experiment on THz generation by the two-color filamentation scheme was reported by Cook and Hochstrasser in 2000 [16]. Their main motivation was to demonstrate the inverse of the previously reported method of Terahertz Field Induced Second Harmonic generation (TFISH) [17, 18] in which a THz field at frequency ω_{THz} and an optical field at frequency ω interact to generate the second harmonic field at frequency $2\omega \pm \omega_{\mathrm{THz}}$. As a result, the generation of THz radiation through two-color filamentation in [16] was explained as a four-wave-mixing (FWM) process where an optical field with frequency ω and its second harmonic with frequency $2\omega \pm \omega_{\mathrm{THz}}$ interact to generate a THz field at frequency ω_{THz}. However, already in the first experiments it became clear that the FWM model of THz generation is incomplete. First, the intensity of the generated THz radiation appeared to be surprisingly strong for a FWM process in ambient air, and second, the threshold of THz generation is strongly correlated with the ionization threshold, that is, the produced plasma plays a significant role in the process of THz generation [16, 19–21].

In response to the incompleteness of the FWM model, in 2007 Kim et al. [22] proposed the photocurrent model of THz generation by two-color filamentation. According to the photocurrent model the free electrons produced by ionization of air, and being accelerated by an asymmetric two-color laser field, produce a nonzero photocurrent. This photocurrent,

occuring on the timescale of the photoionization, can emit an electromagnetic pulse at THz frequencies.

Since then a number of attempts have been made in order to validate which of the above mechanisms dominates and which model describes the process of THz generation by two-color filamentation correctly [23–29]. Recent studies [26, 27, 29] show that both FWM and photocurrent mechanisms contribute to THz generation; the contribution of FWM is much weaker and generates higher THz frequencies than plasma. However these results were obtained for the case of parallel linearly polarized ω and 2ω fields. In case of more complicated polarization states of the two-color field it was shown that using only the FWM model it is possible to explain the observed polarization of the generated THz pulse [23, 24, 30], while the photocurrent model can give irrelevant predictions [23, 24].

When using both the FWM and the photocurrent model in order to predict the yield and polarization of THz radiation generated by arbitrarily polarized ω and 2ω fields, one can see that when the polarizations of both ω and 2ω fields are linear or circular, the FWM and photocurrent models give qualitatively similar predictions that are in agreement with available experimental data [add our ref]. However, in the case where one of the components of the two-color field is elliptically polarized, the predictions of the two models diverge. In particular, the study of THz yield dependence on the ellipticity of the main harmonic can be used to define the dominant mechanism of THz field polarization formation.

2.2.1 FWM and photocurrent models

In general, the microscopic FWM and the photocurrent models can be applied only to short plasma filament lengths. For longer plasma channels macroscopic effects, like air-plasma dispersion or absorption, become crucial. Therefore, the FWM and photocurrent models are better suited for modeling experiments with tightly focused two-color beams. Nevertheless, despite the fact that the FWM and the photocurrent models oversimplify the processes of two-color filamentation, they can provide a valuable analytic insight on the main trends, not to mention the fact that they can be applied much faster than more precise but time consuming simulations.

In the framework of the FWM model, the generation of THz field by two-color filamentation can be described by a nonlinear process of the third order. In general, the components of the corresponding nonlinear polarization vector $\mathbf{P}$ can be written as

$$P_i = \varepsilon_0 \sum_{jkl} \chi^{(3)}_{ijkl} E_j E_k E_l, \tag{2.7}$$

where i, j, k, and l denote one of the Cartesian coordinates x, y, z, while $\chi^{(3)}_{ijkl}$ are the elements of the third-order susceptibility tensor, and E_j are the components of the electric field vector **E**. In an isotropic medium, like air, the susceptibility tensor possesses the following symmetry properties [31]:

$$\chi^{(3)}_{xxxx} = \chi^{(3)}_{yyyy} = \chi^{(3)}_{zzzz}, \tag{2.8a}$$

$$\chi^{(3)}_{xxyy} = \chi^{(3)}_{xxzz} = \chi^{(3)}_{yyxx} = \chi^{(3)}_{yyzz} = \chi^{(3)}_{zzxx} = \chi^{(3)}_{zzyy}, \tag{2.8b}$$

$$\chi^{(3)}_{xyxy} = \chi^{(3)}_{xzxz} = \chi^{(3)}_{yzyz} = \chi^{(3)}_{yxyx} = \chi^{(3)}_{zxzx} = \chi^{(3)}_{zyzy}, \tag{2.8c}$$

$$\chi^{(3)}_{xyyx} = \chi^{(3)}_{xzzx} = \chi^{(3)}_{yxxy} = \chi^{(3)}_{yzzy} = \chi^{(3)}_{zxxz} = \chi^{(3)}_{zyyz}. \tag{2.8d}$$

The four types of nonzero elements appearing in Eq. (2.8) are not independent and are related by the equation [31]

$$\chi^{(3)}_{xxxx} = \chi^{(3)}_{xxyy} + \chi^{(3)}_{xyxy} + \chi^{(3)}_{xyyx}. \tag{2.9}$$

Equations (2.8) and (2.9) allow us to express the nonlinear susceptibility in the following compact form [31]:

$$\chi^{(3)}_{ijkl} = \chi^{(3)}_{xxyy}\delta_{ij}\delta_{kl} + \chi^{(3)}_{xyxy}\delta_{ik}\delta_{jl} + \chi^{(3)}_{xyyx}\delta_{il}\delta_{jk}, \tag{2.10}$$

where δ_{ij} are the Kronecker symbols. By substituting Eq. (2.10) into Eq. (2.7) we find

$$P_i = \varepsilon_0 \left(\chi^{(3)}_{xxyy} + \chi^{(3)}_{xyxy} + \chi^{(3)}_{xyyx}\right) \sum_j E_j^2 E_i. \tag{2.11}$$

Then, using Eq. (2.9) and denoting $\chi^{(3)}_{xxxx}$ simply as $\chi^{(3)}$ and taking into account that we consider only transversal field components, E_x and E_y, we finally obtain

$$P_x = \varepsilon_0 \chi^{(3)} \left(E_x^2 + E_y^2\right) E_x, \tag{2.12a}$$

$$P_y = \varepsilon_0 \chi^{(3)} \left(E_x^2 + E_y^2\right) E_y, \tag{2.12b}$$

where the components E_x and E_y can be found from Eqs. (2.16)-(2.18). In the far zone the radiation produced by the nonlinear polarization $\mathbf{P}^{(3)}$ is proportional to its second temporal derivative, $\ddot{\mathbf{P}}^{(3)}$, while the THz field corresponds to the low frequency part of $\ddot{\mathbf{P}}^{(3)}$.

In turn, according to the photocurrent model the THz radiation is produced by a nonzero current of free electrons accelerated by the asymmetric two-color field [22]. If we assume zero velocity for newly born electrons and neglect ponderomotive forces, then the equation

for the plasma current density $\mathbf{J}$ can be written as [32]

$$\frac{\partial \mathbf{J}}{\partial t} + \nu_c \mathbf{J} = \frac{q_e^2}{m_e} \rho_e \mathbf{E}, \tag{2.13}$$

where $\mathbf{E}$ is the two-color field from Eq. (2.18), ν_c is the collision frequency, q_e and m_e are the charge and mass of electrons, and ρ_e is the concentration of free electrons that can be found by solving the following kinetic equation:

$$\frac{\partial \rho_e}{\partial t} = R(E)(\rho_0 - \rho_e), \tag{2.14}$$

where $R(E)$ is the ionization rate with $E = (E_x^2 + E_y^2)^{1/2}$ and ρ_0 is the concentration of neutral molecules. In this thesis, in order to calculate the ionization rate $R(E)$ we use the Ammosov-Delone-Krainov (ADK) tunneling ionization formula [9, 33]:

$$R(E) = \frac{\alpha_{\mathrm{ADK}}}{(E/E_a)^{2n-1}} \exp\left(-\frac{\beta_{\mathrm{ADK}}}{E/E_a}\right), \tag{2.15}$$

where $\alpha_{\mathrm{ADK}} = (q_e U_i/\hbar)|C_n|^2 (4\sqrt{2} r_a^{3/2})^{2n-1}$, $\beta_{\mathrm{ADK}} = (4\sqrt{2}/3) r_a^{3/2}$, $n = \sqrt{U_H/U_i}$, $r_a = U_i/U_a$, $|C_n|^2 = 2^{2n}[n\Gamma(n)\Gamma(n+1)]^{-1}$, $\Gamma(x)$ is the Gamma function, $E_a = m_e^2 q_e^5/[(4\pi\varepsilon_0)^3\hbar^4] \approx 5.14 \times 10^{11}$ V/m is the atomic field, $U_a = m_e q_e^3/[(4\pi\varepsilon_0)^2\hbar^2] \approx 27.2$ eV is the atomic potential, $U_H \approx 13.6$ eV is the ionization potential of hydrogen, and U_i is the ionization potential of the medium atoms or molecules. For our calculations we use the ionization potential of nitrogen $U_i = 15.6$ eV, the concentration of neutral molecules is $\rho_0 = 2.4 \times 10^{25}$ m^{-3}, and the collision frequency $\nu_c = 5 \times 10^{12}$ s^{-1}. For simplicity we neglect the ionization impact of oxygen – the second main component (after nitrogen) of the atmospheric air, because it affects the result only quantitatively while the photocurrent model is essentially qualitative. In the far zone, the radiation produced by the current $\mathbf{J}$ is proportional to its first temporal derivative $\dot{\mathbf{J}}$. To find the components of the generated THz field vector $\mathbf{E}^{\mathrm{THz}} = E_x^{\mathrm{THz}}\hat{\mathbf{x}} + E_y^{\mathrm{THz}}\hat{\mathbf{y}}$ one can compute the Fourier transform of $\ddot{\mathbf{P}}^{(3)}$ and $\dot{\mathbf{J}}$ and take their low frequency part ($\leq$100 THz). The THz yield is measured with we use the THz field amplitude $A^{\mathrm{THz}} = [(A_x^{\mathrm{THz}})^2 + (A_y^{\mathrm{THz}})^2]^{1/2}$ with the amplitudes of x and y THz field components defined as $A_x^{\mathrm{THz}} = \max(E_x^{\mathrm{THz}}) - \min(E_x^{\mathrm{THz}})$ and $A_y^{\mathrm{THz}} = \max(E_y^{\mathrm{THz}}) - \min(E_y^{\mathrm{THz}})$.

The case when the main and second harmonic are linearly polarized is well studied including the impact from each of the above mechanisms. However, for the cases when the two-color fields have complex polarization states the role of the four-wave mixing and plasma mechanisms in the formation of THz polarization is still under-explored. On the other hand, one of the many characteristics of this source is its donut-shaped beam profile in the

far field. Understanding the underlying mechanisms of THz generation through two-color filamentation, as well as the conical character of this source is exciting and crucial.

The rest of the chapter will be separated in two parts. In the first part, we will use both the four-wave mixing and photocurrent models in order to consider the THz generation by two-color fields with arbitrary polarizations and we will show that under specific polarizations of the two-color field components it is possible to determine which of the mechanisms is responsible for THz polarization formation.

In the second one, we will propose a comprehensive physical model, accompanied with experimental verification, explaining the conical character of THz emission from this source. Responsible for this behavior is phase matching of the radiation produced inside the filament, combined with a partial back reflection of the generated terahertz field from the filament itself due to the frequency-dependent critical plasma density. Unlike previously proposed models, our model shows good agreement with our experiments as well as a wide range of experimental findings from the literature.

2.3 The model of arbitrarily polarized two-color field

There are two experimental schemes of two-color filamentation. In the inline scheme the second harmonic crystal (usually a BBO), is placed on the way of the pump laser beam, after the focusing lens (Fig. 2.3(a)). In the combined scheme an independently generated second harmonic is mixed with the main harmonic using a dichroic mirror, and then the obtained two-color field is focused by a lens (Fig. 2.3(b)). Whilst the combined scheme allows a direct control (and hence, detailed study) of the $\omega - 2\omega$ time delay, relative polarization and intensity, the optical setup must be interferometrically stabilized in order to maintain a stable $\omega - 2\omega$ phase shift.

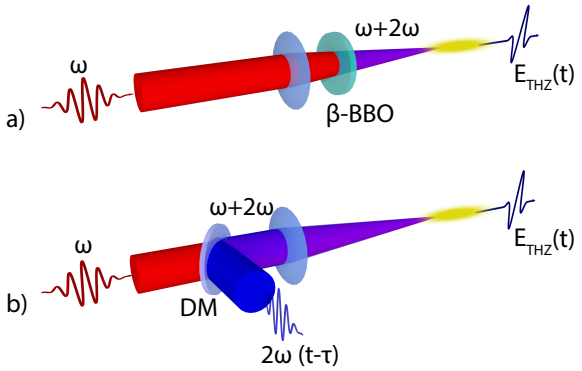

Fig. 2.3 Two experimental schemes of two-color filamentation: (a) inline and (b) combined.

Therefore, in practice the inline scheme is used much more often. In turn, in the inline scheme the individual control of $\omega - 2\omega$ polarizations is quite complicated, because the BBO crystal in this scheme is typically detuned from its optimal angle (when the ω polarization is parallel to the ordinary axis of the BBO) in order to produce an ω-field component parallel to the 2ω field polarized along the BBO extraordinary axis. As a result, the ω field becomes elliptically polarized after passing through the BBO crystal. Alternatively, the BBO crystal can be rotated for type-I phase matching, which results in crossed polarization of the ω and the 2ω fields. Then a tunable dual-band wave plate can be used to control the mutual orientation of the ω and 2ω fields, or additional quarter wave plates operating at ω and 2ω frequencies for further controlling the polarizations of the two fields [34]. In the later case though, a compensation plate is inserted in the setup in order to compensate for the pulse separation due to the multiple optical elements.

To describe an arbitrarily polarized two-color field, the following equations can be used for the main, $\mathbf{E}^{\omega}(t) = E_x^{\omega}(t)\hat{\mathbf{x}} + E_y^{\omega}(t)\hat{\mathbf{y}}$, and second harmonic, $\mathbf{E}^{2\omega}(t) = E_x^{2\omega}(t)\hat{\mathbf{x}} + E_y^{2\omega}(t)\hat{\mathbf{y}}$, fields:

$$\mathbf{E}^{\omega}(t) = A^{\omega} e^{-\frac{t^2}{2t_0^2}} \left[\cos(\omega t)\hat{\mathbf{x}} + \varepsilon_{\omega}\sin(\omega t)\hat{\mathbf{y}}\right], \tag{2.16a}$$

$$\mathbf{E}^{2\omega}(t) = A^{2\omega} e^{-\frac{t^2}{t_0^2}} \left[\cos(2\omega t + \phi)\hat{\mathbf{x}} + \varepsilon_{2\omega}\sin(2\omega t + \phi)\hat{\mathbf{y}}\right], \tag{2.16b}$$

where $\hat{\mathbf{x}}$ and $\hat{\mathbf{y}}$ are the unit vectors along x and y axes, A^{ω} and $A^{2\omega}$ are the amplitudes, with ϕ being a relative phase. By tuning the ellipticity ε_{ω} and $\varepsilon_{2\omega}$ one can individually define an arbitrary polarization state of ω and 2ω fields: $\varepsilon_i = 0$ and 1 determine linear and circular polarizations ($i = \omega$ or 2ω), while the intermediate values correspond to an elliptical polarization; the sign of ε_i allows to switch between left- and right-handed polarizations.

In order to describe nonparallel $\omega - 2\omega$ polarizations we introduce the 2ω field $\mathbf{E}^{2\omega'} = E_x^{2\omega'}\hat{\mathbf{x}} + E_y^{2\omega'}\hat{\mathbf{y}}$ rotated by some angle θ:

$$E_x^{2\omega'} = E_x^{2\omega}\cos\theta - E_y^{2\omega}\sin\theta, \tag{2.17a}$$

$$E_y^{2\omega'} = E_x^{2\omega}\sin\theta + E_y^{2\omega}\cos\theta. \tag{2.17b}$$

Finally, the total two-color electric field $\mathbf{E} = E_x\hat{\mathbf{x}} + E_y\hat{\mathbf{y}}$ can be written as

$$\mathbf{E} = \mathbf{E}^{\omega} + \mathbf{E}^{2\omega}. \tag{2.18}$$

For our calculations we use the following parameters of ω and 2ω fields: corresponding wavelengths 800 nm and 400 nm, with intensities $I^{\omega} = \varepsilon_0 c_0 A^2/2 = 10^{14}$ W/cm^2 and $I^{2\omega} = 0.2I^{\omega}$, and pulse duration $t_0 = 50/(2\sqrt{\ln 2})$ fs, or 50 fs FWHM.

2.3.1 Nonparallel linearly polarized ω and 2ω fields

Among different polarization states the case of nonparallel linearly polarized ω and 2ω fields is the second more studied after the parallel one [35–37, 34, 38, 30]. The conducted experiments show that in the regimes where the propagation effects can be neglected, independently on the angle between the ω and 2ω polarizations, the polarization of the generated THz field remains linear. Additionally, the THz polarization essentially follows the polarization of the 2ω field (see Fig. 3 in [30]), however the THz yield is about one order of magnitude higher when ω and 2ω are parallel polarized than when they are orthogonally polarized. In order to

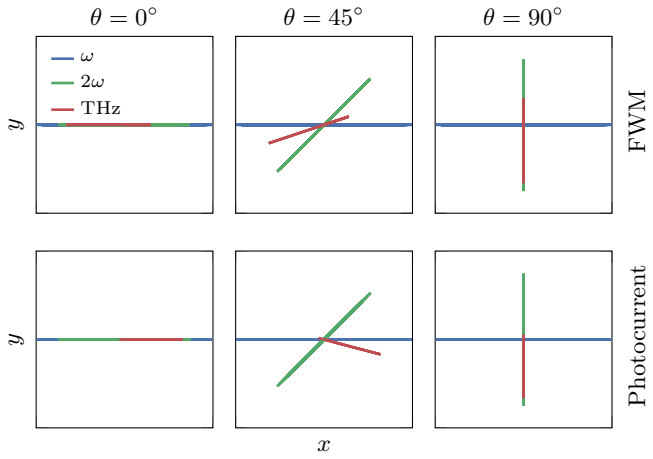

Fig. 2.4 xy-plane projection of ω, 2ω, and THz normalized fields for several values of 2ω rotation angle θ. THz field is calculated by (top row) the FWM and (bottom row) photocurrent models.

study the above polarization configuration we set $\varepsilon_{\omega} = \varepsilon_{2\omega} = 0$ in Eq. (2.16), and vary the angle θ in Eq. (2.17). As the relative phase ϕ we take 0 and $\pi/2$ in case of the FWM and photocurrent models, respectively. These phases have been predicted to be the optimal ones (in terms of the THz yield) for each of the model [16, 22]

Figure 2.4 shows the mutual orientation of ω, 2ω, and THz fields, projected on the xy plane. One can see that both models predict that the THz polarization follows the polarization of the 2ω field. In particular, when the polarizations of ω and 2ω are orthogonal, the THz is polarized along the 2ω. However, according to the photocurrent model the THz and 2ω polarizations rotate in the opposite directions.

Figure 2.5 shows the THz yield as a function of the 2ω rotation angle θ for both FWM and photocurrent models. We see that the predictions of the models are similar: the THz

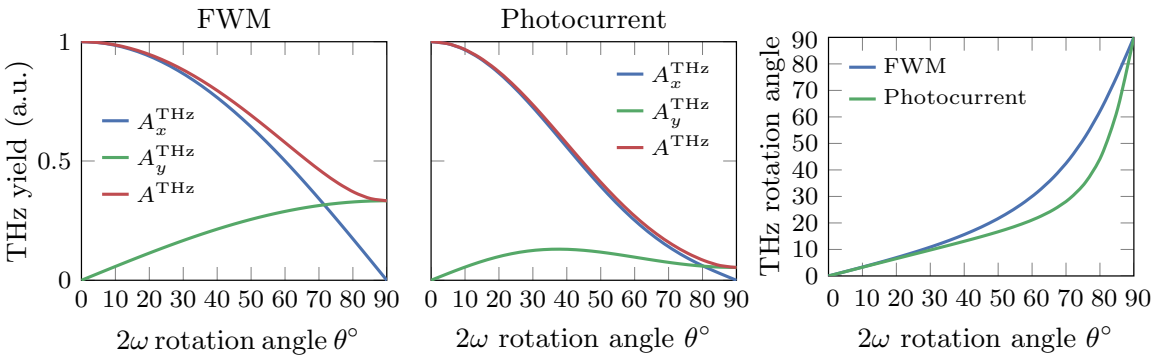

Fig. 2.5 THz yield as a function of 2ω *rotation angle* θ *according to (left) FWM and (center) photocurrent models. (Right) THz rotation angle versus* 2ω *rotation angle* θ *for both models.*

yield decreases with increase of θ, reaching its minimum at $\theta = 90^\circ$ (orthogonal ω and 2ω). Also, Fig. 2.5 shows that the FWM model predicts three times higher THz yield for orthogonal ω and 2ω. Additionally, Fig. 2.5 shows the dependence of the THz polarization angle on θ. One can see that at small θ the dependence of THz rotation angle on θ is linear. Though, closer to $\theta = 90^\circ$ the THz polarization very rapidly approaches the polarization of 2ω, that is, in case of orthogonal ω and 2ω fields, the THz polarization parallel to 2ω can be considered as an unstable equilibrium.

To sum up, in the case of nonparallel linearly polarized ω and 2ω fields the major predictions of both FWM and photocurrent model are in agreement with the published experimental data. The existing discrepancies are minor and do not allow a rigorous experimental verification of the impact from each one of the THz generation mechanisms.

2.3.2 Circular polarization of ω and 2ω fields

In [34] Dai et al. studied the THz yield and polarization for different polarization states of ω and 2ω fields. In particular they showed that when the ω and 2ω fields are both circularly polarized, the THz polarization remains linear and rotates with relative phase ϕ, while the THz intensity remains constant.

In order to study this polarization state we set $\varepsilon_\omega = \varepsilon_{2\omega} = 1$ in Eq. (2.16) and vary the relative phase ϕ between the ω and 2ω fields.

Figure 2.6 show the orientation of ω, 2ω, and THz fields for several values of the relative phase ϕ. One can see that in agreement with the experimental data by Dai et al. [34] both the FWM and the photocurrent models predict the rotation of THz polarization with ϕ. We note that the THz field calculated by the photocurrent model is slightly elliptic.

Figure 2.7 shows that, in full agreement with the experiment, both models predict an invariant THz yield under changes of the relative phase ϕ. Also Fig. 2.7 shows that the

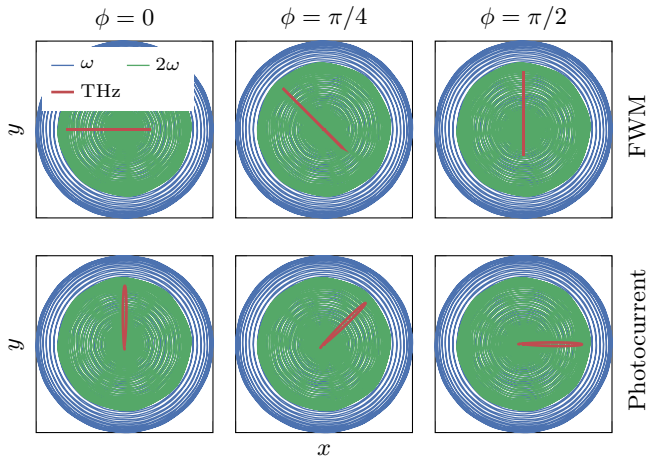

Fig. 2.6 xy-plane projection of ω, 2ω, and THz normalized fields for several values of relative phase ϕ. THz field is calculated by (top row) the FWM and (bottom row) photocurrent models.

rotation angle of the THz polarization depends linearly on ϕ. Additionally to the facts stated in [34] we found that when the circular polarization of ω and 2ω fields have different rotation directions ($\varepsilon_\omega = 1$ and $\varepsilon_{2\omega} = -1$ or vise versa), the THz emission becomes suppressed for all values of ϕ.

The results presented in this section show that in the case of circularly polarized ω and 2ω fields, the predictions of both FWM and photocurrent models agree with the experimental data of [34]. Taking into account that in their paper Dai et al. [34] used a sophisticated quantum mechanical model in order to support the experimental data, we can conclude that despite the simplicity of the FWM and photocurrent models their predictions are very close to the more rigorous models.

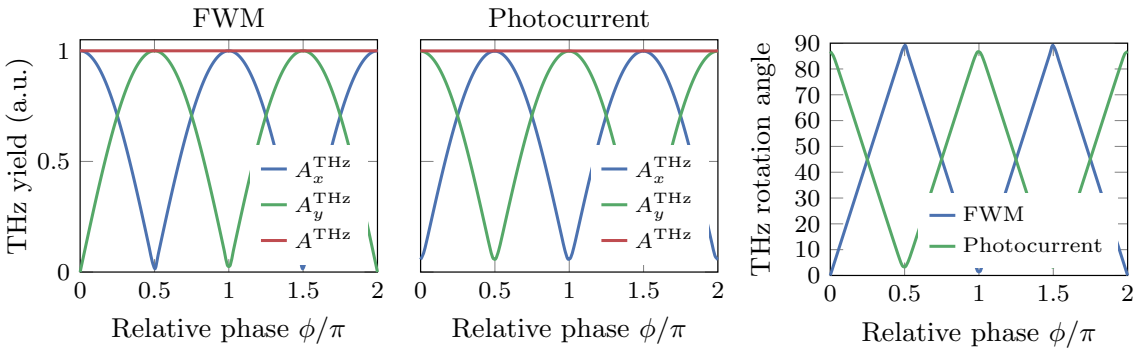

Fig. 2.7 THz yield as a function of relative phase ϕ according to (left) FWM and (center) photocurrent models. (Right) THz rotation angle versus ϕ for both models.

2.3.3 Dependence on ellipticity of ω field polarization

More intriguing polarization states were considered by Théberge et al. in [24] where the authors studied the generation of far-infrared radiation (FIR) in the range of 5–12 μm (25–60 THz) during the two-color filamentation in air. In particular the authors of [24] studied the dependence of FIR yield on the ellipticity of the ω field, while the orientation of a linearly polarized 2ω field was fixed. They found that FIR yield growths with ω field ellipticity and reaches its maximum when the ω field is circularly polarized. Using propagation simulations based on the FWM model, Théberge et al. showed that the FWM model better fits the experimental data than the photocurrent model. However, we want to note that this conclusion should be extrapolated to the the whole THz spectrum with caution, because the authors of [24] studied only the high frequency part of the THz spectrum that is known to be generated mainly through the FWM mechanism [26, 27, 29]. In addition we note that the experiment by Théberge et al. [24] was conducted using a long focus lens (f=1.5 m) that produces long plasma channels and, therefore, the propagation effects in this experiment can have significant impact on the final THz polarization [39, 23].

To study the polarization state from [24], we set $\varepsilon_{2\omega} = 0$ in Eqs. (2.16) and vary the ellipticity ε_ω of the ω field. Additionally, we choose the rotation angle θ to be zero.

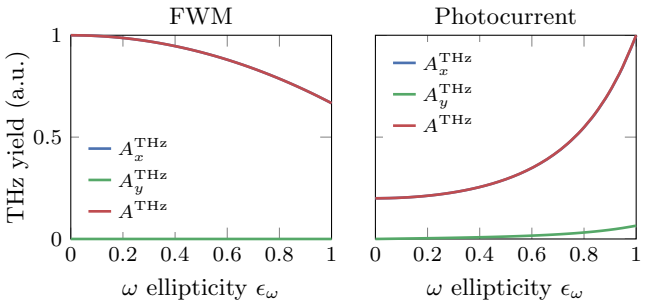

Fig. 2.8 THz yield as a function of ω field ellipticity ε_ω according to (left) the FWM and (right) the photocurrent model.

Figure 2.8 shows the dependence of the THz yield on the ellipticity ε_ω of the main harmonic calculated by the FWM and the photocurrent models (the relative phase ϕ in these calculations was set to 0 for the FWM model and $\pi/2$ for the photocurrent model). Surprisingly, the predictions of the FWM and the photocurrent models in this case are opposite: according to the FWM model the THz yield decreases with ε_ω, while the photocurrent model predicts an increase.

In order to provide more details we also studied the effect of the relative phase ϕ. Figure 2.9 shows the dependence of the THz yield on both the relative phase ϕ and ω field ellipticity ε_ω. One can see that according to the FWM model the effect of the relative phase

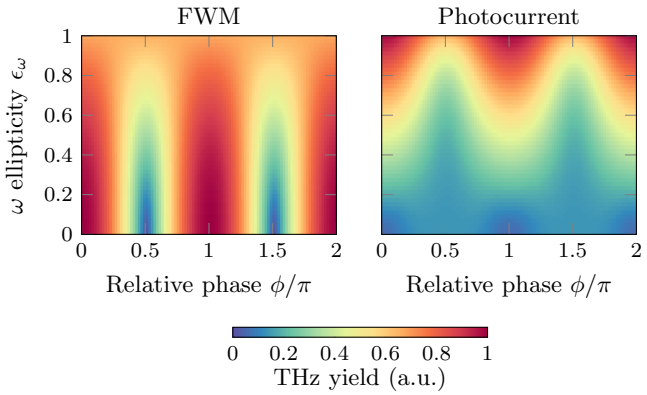

Fig. 2.9 THz yield as a function of the relative phase ϕ and ω field ellipticity ε_ω according to (left) the FWM and (right) the photocurrent model.

ϕ washes out when the ω polarization approaches to circular. In particular, for a circularly polarized ω field the THz yield becomes independent on ϕ. In turn, the photocurrent model predicts that while the ω polarization is linear, the optimal phase ϕ follows the expression $\phi = (n+1/2)\pi$ ($n = 0,1,2,...$). However, when ω becomes circularly polarized this expression is changed to $\phi = n\pi$.

Thus, the case of linearly polarized 2ω field and elliptically polarized ω field shows strong inconsistency between the predictions of the FWM and the photocurrent models. This in turn is useful since experimental studies of the THz yield dependence on the ellipticity of the ω field can reveal which of the two mechanisms is dominating in the formation of the THz polarization during the two-color filamentation.

2.4 Physical mechanisms of THz conical emission

As described in the previous chapter, phase matching (PM) is essential for efficient THz generation. In the two-color plasma generation the total terahertz yield appears to depend on phase matching between the fundamental (ω) and the second(2ω) harmonic of the focused laser beam that produces the filament and hence THz radiation. Since the dephasing length for ω and 2ω in the plasma string for typical average filament plasma densities is about $10-20$ mm, it had been considered that no further change in the THz generation from filament elongation can be expected [40]. However, You et.al. [41] demonstrated continuous increase of theTHz yield while changing the filament length up to 60 mm, which is far above the dephasing length. They explain this effect by the THz off-axis PM, i.e. radiation is generated onto a cone surface around the optical axis. Although the THz generation in two-color laser filament model proposed by You et.al. [41] shows a conical far field distribution due to

THz off-axis PM, it presents a number of inconsistencies and limitations when compared to various experimental findings. This can be understood by a number of parameters that have not been taken into account as well as the fact that the plasma densities considered in their model were far too low ($\sim 10^{16}$ cm^{-3}) compared to the ones in the experiments with measured densities up to $\sim 10^{18}$ cm^{-3} [42]. Other parameters that limited the model were the absence of phase change due to propagation of THz radiation inside the filaments, as well as the fact that all the waves below the plasma frequency cannot propagate through it. Finally, all the calculations in Ref.[41] were performed for monochromatic THz waves, not ultrabroadband as in reality.

Next a comprehensive two-dimensional model of two-colour filament THz generation is proposed, that addresses the shortfalls of the previous model discussed above, like the phase change that terahertz radiation gets due to propagation inside the plasma, as well as plasma opacity for radiation with frequencies below its own one. This gives the opportunity to consider higher plasma density values that are more realistic and close to the experiments. We include the broadband spectral character of the generated terahertz radiation, which in the case of such broadband (0.5-15 THz, i.e. 5 octaves) radiation is crucial. Also, we introduce spatial non-uniformity of the plasma density both along and across the filament. Following this careful description of the physical processes involved, we show that results obtained with our model compared to Ref.[41] are qualitatively very different. Detailed simulations with full and simplified models for a wide range of initial parameters, if compared with experimentally obtained data of the spatial emission patterns show much better agreement with our comprehensive approach. Finally, we further validate our model by nicely reproducing other experimental findings from the literature.

2.4.1 Theoretical description

Since the geometry of the process is axially symmetric, we use a two-dimensional model to simplify the equations and speed up the calculations and introduce a flat cartesian coordinate system with z axis along the filament and x axis across it. THz radiation generated inside the filament is proportional to the nonlinear polarisation produced in air by focusing the fundamental and the second harmonic of femtosecond optical pulses:

$$P(x,z,\Omega) \propto A(x,z,\Omega)\sin(\theta(z))\,exp\left(ik_{THz}z\right) \tag{2.19}$$

where $A(x,z,\Omega)$ is the amplitude of the generated terahertz field at a certain point of the filament for all frequencies of interest. The central frequency of the generated spectrum is proportional to the square root of plasma density, as proposed in [43–46], and varies from

point to point inside the filament, as well as the overall amplitude of the spectrum, which is proportional to the plasma density N_e. The $\sin(\theta(z))$ term describes the terahertz field amplitude modulation due to the relative phase walk-off between the fundamental and the second harmonic during their propagation inside the filament. For the case of non-uniform filaments, this phase difference can be calculated as

$$\theta(z) = \theta_0 + \int_{z_{max}}^{z} (n_{2\omega}(z') - n_{\omega}(z'))k_{\omega}dz' \tag{2.20}$$

z_{max} is the coordinate of the point with maximum plasma density inside the filament, $n_{\omega}(z') = n_{air,\omega} + n_{plasma,\omega}(z')$ are the refractive indices for ω and 2ω respectively, $n_{air,\omega,2\omega}$ are taken from [47] and

$$n_{plasma,\omega}(z') \approx \sqrt{1 - \frac{\omega_p^2(z')}{\omega^2}} \tag{2.21}$$

To calculate the plasma frequency $\omega_p(z')$ we use the well-known relation [48] $\omega_p = \sqrt{4\pi e^2 N_e(z')/m_e}$, that gives ~ 1 THz for $N_e = 10^{16}$ cm^{-3}, and ~ 3 THz for $N_e = 10^{17}$ cm^{-3}.

The last term in Eq. 2.20 reflects the phase difference of the THz radiation produced at various filament points.

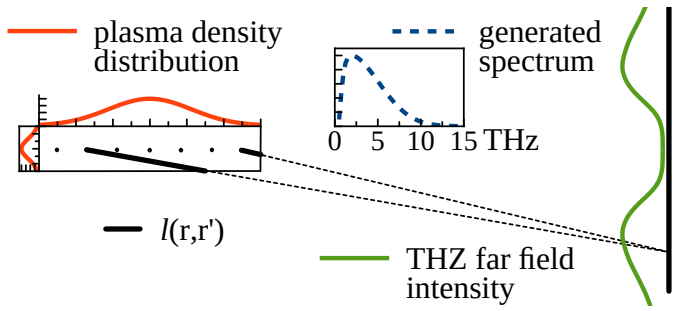

Fig. 2.10 Schematic representation of two-color filament THz generation model.

To calculate the THz far field distribution for a frequency Ω we must integrate over the whole filament with known plasma density distribution [49]:

$$E(r,\Theta,\Omega) \propto k_{THz} \int_V \frac{P(r',\Omega)\exp\left(ik_{THz}|r-r'|\right)h(r',r,\Omega)}{|r-r'|} d^2r' \tag{2.22}$$

where $r = (\xi,\eta)$ is the point at the registration plane, $r' = (x',z')$ is the point inside the filament, and $h(r',r,\Omega)$ represents the phase change that generated THz radiation acquires inside the filament or its blocking if the frequency is less than the plasma frequency at

any point of the ray trace between the source point and the registration plane. $h(r',r,\Omega)$ is calculated separately as a multiplier

$$h\left(r',r,\Omega\right)=\begin{cases}0 & \Omega<\omega_p\\ \exp\left[i\int\limits_{l(r,r')}k_{THz}\left(n_{THz}\left(\xi,\Omega\right)-1\right)d\xi\right] & \Omega\geq\omega_p\end{cases} \tag{2.23}$$

Where $l(r,r')$ is the part of the ray path between r and r' that lies inside the filament (Fig. 2.10) and n_{THz} is the plasma refractive index at the point ξ on $l(r,r')$ inside the filament for frequency Ω:

$$n_{THz}\left(\xi,\Omega\right)=\frac{1}{\sqrt{1-\frac{\omega_p^2(\xi)}{\Omega^2}}}. \tag{2.24}$$

The unity in Eq. 2.23 is disregarded not to accumulate the phase change due to wave propagation through the same region in space twice, since it has already been considered in Eq. 2.22.

The obtained broadband far field intensity distribution can be then expressed as a sum of monochromatic intensities [50]:

$$I\left(r,\Theta\right)=\sum_{\Omega}\left|E\left(r,\Theta,\Omega\right)\right|^2\cdot\alpha\left(\Omega\right) \tag{2.25}$$

where $\alpha(\Omega)$ is the sensitivity function of the detector used in the experiments.

Natural phase matching due to simple interference occurs at various cone angles for all spectral components of the broadband generated spectrum. This results in a broadening of the resulting donut thickness compared to a single wavelength interference pattern. One of the most essential results obtained with this model is the off-axis character of the produced THz for all studied filament lengths and plasma densities starting from a certain minimum peak plasma density n_{min} which is typically less than $3\times10^{14}\text{cm}^{-3}$ and depends on the filament length as shown in Fig. 2.11(a). Since plasma densities below $3\times10^{14}\text{cm}^{-3}$ are much lower than experimentally obtained values [51], we observed conical emission of THz radiation in all studied cases. Extinction of the on-axis emission is explained by the destructive interference of radiation for all wavelengths that appears if phase change of the produced THz wave inside the filament is taken into account (Fig. 2.11(b)). The dephasing length of a filament with 7×10^{16} cm^{-3} plasma density is 18 mm, which is almost twice longer than the filament length taken in the model (10 mm). Thus, if in-filament phase change was not considered in the calculations, the produced THz profile would have been on-axis; this is what is shown with dashed red line in Fig. 2.11(b). If phase change is introduced, a

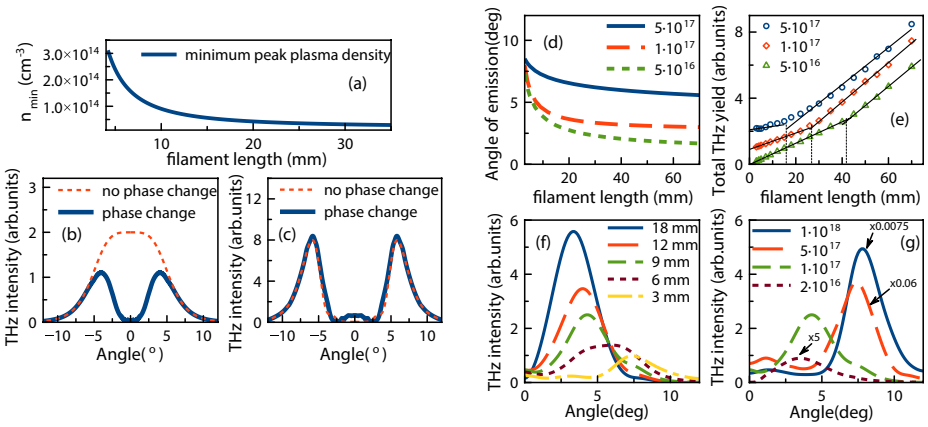

Fig. 2.11 Minimum peak plasma density for comical emission(a), simulation results for far field THz profiles of 10 mm (b) and 20 mm (c) long filaments with maximum plasma density of 7×10^{16} *cm*$^{-3}$ *and* 7×10^{17} *cm*$^{-3}$ *respectively calculated with and without phase change inside the filament, (d) conical emission angle for filaments with different maximum plasma density, (e) total terahertz yield for filaments with different maximum plasma density (scaled and shifted for readability), (f) far field THz profiles of filaments with maximum plasma density of* 1×10^{17} *cm*$^{-3}$ *and different lengths, (g) far field THz profiles of 9 mm long filaments with various maximum plasma densities, scaled to fit the plot, multipliers shown with arrows.*

conical spatial profile appears (solid blue line in Fig. 2.11(b)). In Fig. 2.11(c) we show that even if the conical THz far field pattern is formed without calculation of the in-filament phase change, because the dephasing length for 7×10^{17} cm^{-3} plasma density is 2.5 mm, 8 times less than filament length of 20 mm, phase change addition does not bring any drastic changes on the spatial pattern of the produced THz radiation. These two mechanisms of forming the conical THz emission from the filament also affect the total THz yield slope. For shorter filaments, where the cone is formed mostly by in-filament dephasing, the total THz yield slope is smaller than the one for longer filaments having the same plasma density. For higher plasma densities, the switch between the two mechanisms occurs at shorter filament lengths as can be clearly seen in Fig. 2.11(e). Also, similarly to [41], the angle of maximum THz intensity direction is bigger for higher plasma densities (Fig. 2.11(g)), but at the same time shorter filaments, even with the same plasma densities produce wider cones of generated THz radiation (Fig. 2.11(f)). If we plot the conical angle versus filament length, we can see a clear and obvious dependency from both plasma density and filament length (Fig 2.11(d)). In all graphs, the mentioned plasma density value corresponds to the filament's maximum plasma density while considering, in general, a Gaussian plasma distribution along and across the propagation axis [42].

2.4.2 Experimental verification

In order to validate our theoretical predictions, we have performed experiments using the setup shown in Fig. 2.12. A Ti:sapphire chirped-pulse amplification laser system delivering 35 fs, 800 nm IR pulses with energies up to 30 mJ at 50 Hz repetition rate has been used. The pulse energy of the beam was controlled by the amplifier of the laser to the desired value. The fundamental (ω) beam was focused by an $f = 200$ mm lens followed by a 50 μm thick beta-barium borate (BBO) Type-I crystal, cut at 29.9° which generates its second harmonic (2ω). Both ω and 2ω were focused in ambient air creating a plasma filament around the focal point that generates THz radiation. A 3 mm thick HDPE filter followed by a 1.5 mm Si wafer were used to filter out any optical and residual IR radiation. In order to obtain the spatial profile of the THz beam an iris of 2 mm in diameter was placed 110 mm away from the end of the filament and was scanned in the $x-y$ plane using a 2D motorized stage allowing for a 50×50 mm scanning range. The radiation transmitted through the iris was collected and guided by two parabolic mirrors onto a broadband pyroelectric detector as shown in Fig. 2.12.

To tailor the plasma strings and control their uniformity we appropriately adjusted the input laser pulse energy as well as the beam wavefront, introducing astigmatism and wavefront distortions by tilting the focusing lens. In this way, different plasma string profiles (both symmetric and asymmetric) with different lengths and maximum electron densities were created. In each case, both THz patterns and plasma spatial distributions were recorded. The spatial distribution of the generated plasma was recorded using a linear CCD camera and imaging its fluorescence emission, providing an estimation for the plasma electron density based on previous measurements and works with our system [42, 51]. In all the experiments the recorded profile of the produced THz radiation had a conical spatial intensity distribution (inset in Fig. 2.12).

Our experiments can be grouped in two cases. In the first one we studied the evolution of the THz beam profile changes when decreasing the filaments maximum electron density and symmetrically shortening its length, see corresponding filament profiles in Fig. 2.13(a). This was achieved by just reducing the input laser power. In the second case the maximum electron density remained constant while the filament's length was getting shorter but in an asymmetric way this time, as shown in Fig. 2.13(b). This result was achieved by reducing the input power and in parallel appropriately tilting the focusing lens.

Our experimental results together with corresponding simulations from our model are shown in Fig. 2.13. In Fig. 2.13 (c) and (d) we plot the corresponding conical angle vs. filament length dependency for the cases of Fig. 2.13 (a) and (b) respectively. For the simulation results shown in Fig. 2.13(c) both the filament length and peak plasma density

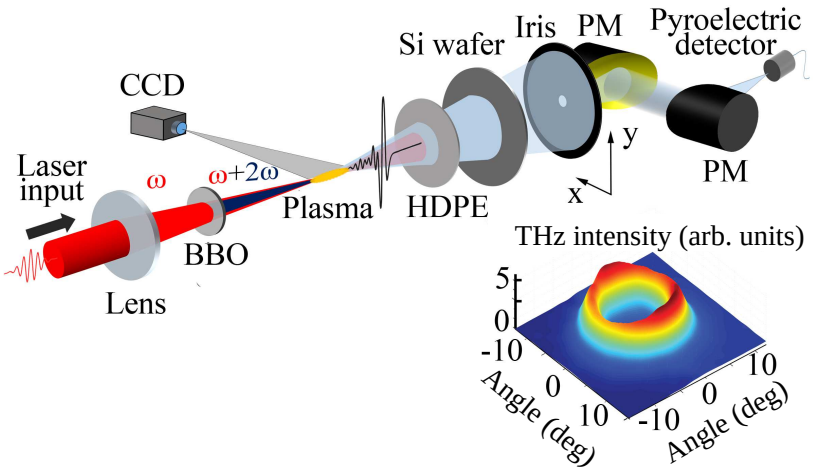

Fig. 2.12 Experimental setup for two-color plasma terahertz generation and far field THz beam profiling, inset: measured conical profile of the THz emission from two-color plasma filament. PM: Parabolic Mirror, HDPE: High Density Polyethelene Filter, BBO: β Barium Borate Type I crystal. Inset shows measured THz profile.

were varied as shown in the inset of Fig. 2.13 (c). In contrast, for the simulations in Fig. 2.13(d) the peak electron density was kept fixed, at 3×10^{17} cm^{-3}, while reducing the filament asymmetric Gaussian distribution length. Experimental and simulated far field THz patterns for selected points from Fig 2.13 (c) and (d) are shown in Fig. 2.13 (e) and (f) respectively. From these one can see that not only the angle of maximum emission, but also the shapes and absolute values of these curves match, demonstrating the strength of our model.

2.4.3 Comparison with experimental data from literature

To further check our model we also explored other experimental works from the literature. First, we used results of far field THz mapping obtained by You et al. [41]. For the simulations we used the filament lengths they report. As for the plasma densities, based on our past works and experience [42, 51] and taking into account the lenses and pulse energies they use we estimate that the maximum plasma density should not be less than 10^{17} cm^{-3}. For our simulations, we used a plasma density of 10^{17} cm^{-3} for the 10 mm filament and 2.5×10^{17} cm^{-3} for the 40 mm filament respectively. As can be seen in figures 2.14 (a),(b), our simulations are in better agreement than their own theoretical predictions.

In other recent works by Blank et. al. [52] and Klarskov et. al. [53] conical emission from two-color filaments was demonstrated, and in [52] the same filament tailoring by tuning the laser pulse energy was performed as we described above with very similar results. In

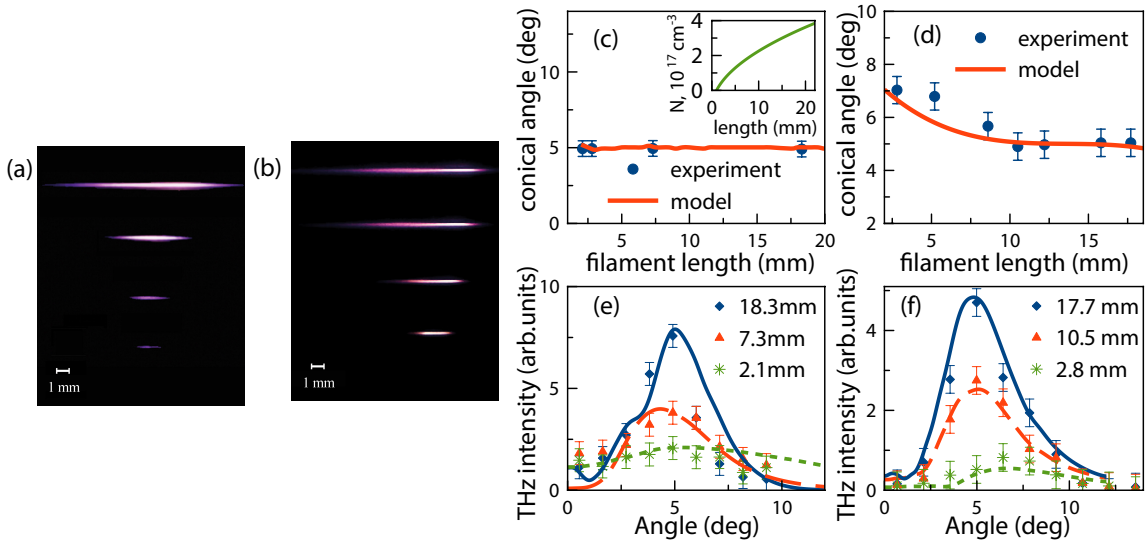

Fig. 2.13 Teraherz generation in symmetric (a), (c), (e) and asymmetric (b),(d), (f) plasma density distribution filaments: (a), (b) — photo of filaments, (c),(d) — conical angle of generated THz , blue points represent experimental results, lines show simulation results, (e),(f) — far field THz intensity profiles produced by filaments shown in (a) and (b) respectively. Dots represent experimental results and lines show simulation results. The inset in (c) shows the maximum plasma density dependency vs. length used in the model for this specific figure.

their experiments the THz generation cone angle remained constant for all pulse energies, something that surprised the authors of that paper but is naturally explained by our model as presented in Fig. 2.13(a),(c),(e). It is worth noticing once more that in order not to block on-axis radiation by photocarriers induced in silicon filters, we use a HDPE filter put in front of the silicon wafer. To reproduce experimental results from [52] we took the filament length of 9.5 mm with maximum plasma density of 5.5×10^{17} cm^{-3} for 100 mm lens (Fig. 2.14(c)) and the filament length of 14 mm with maximum plasma density of 1.8×10^{17} cm^{-3} for 200 mm lens (Fig. 2.14(d)). For the THz emission profile from [53] reproduction, we took the filament length of 22 mm, which is close to the length they report, and plasma density of 3×10^{17} cm^{-3}, estimated from the pulse energy they use. A comparison of the experimental data from [53] with our model results is shown in Fig. 2.14(e).

Our model describes not only the spatial profile of the generated THz field, but also its spectrum. In another recent work Borodin et. al. [54] studied the conical emission from two-color filaments and showed that higher THz frequencies are found at smaller cone angles. We have performed simulations with our code for their experiments and as can be seen in Fig. 2.14(f), we find nice agreement between their experiments and our model for the spectral distribution. In the model, we used a peak electron density of 1.5×10^{17} cm^{-3}, which is close to the average one they report, and a filament length of 7 mm, which is in agreement

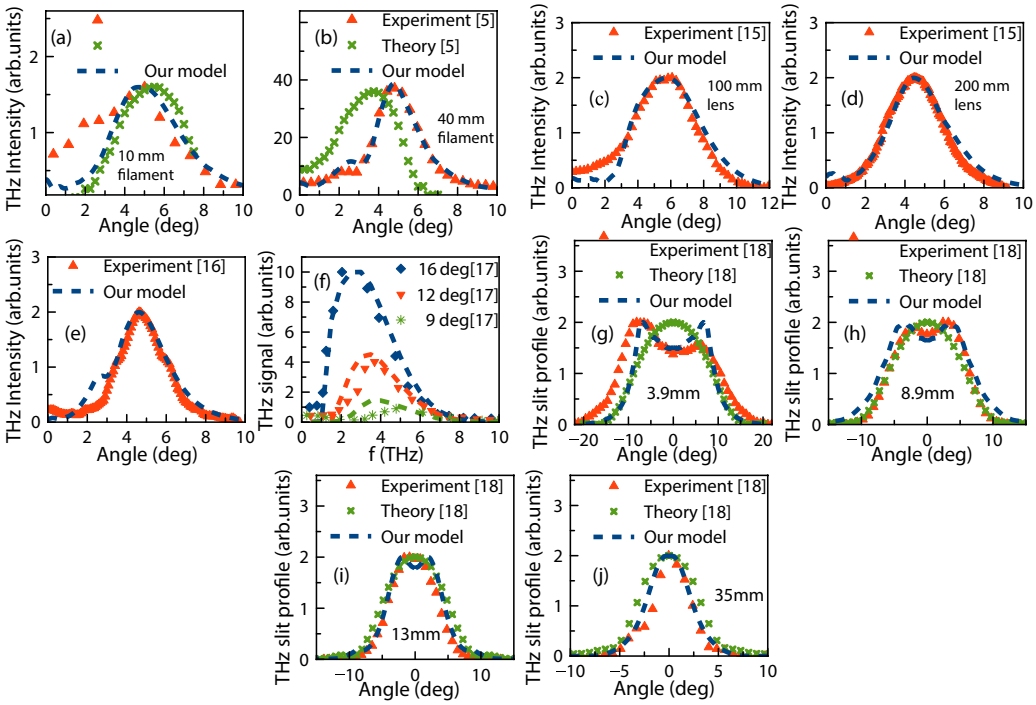

Fig. 2.14 (a), (b) Far field THz patterns through germanium filter, experimental (triangles) and theoretical (crosses) points taken from [41] and compared with our model (dashed line), for two cases of (a) 10mm filament produced by 1.3 mJ pulse, (b) 40 mm filament produced by 5 mJ pulse; (c), (d) far field THz patterns: experimental points (triangles) taken from [52] and compared with our model (dashed line), for two cases of (c) filament produced through 100 mm lens , (d) filament produced through 200 mm lens, pulse energy in both cases 0.71 mJ; (e) far field THz pattern from [53] repeated and explained with our model (dashed line); (f) Simulated THz spectra for various collection angles, experimental data taken from [54], followed by dashed lines calculated with our model; (g), (h), (i), (j) — THz patterns from [55] (triangles), with their theory (crosses) and reproduced with our model (dashed line).

with our measurements under similar experimental conditions, Fig. 2.13 (c). Finally, we reproduced some older experimental data from Ref.[55]. For this we rearranged our model output to show the result of scanning the THz profile with a vertical slit. We used the filament lengths given in [55], yet for the plasma densities we again use our estimations. Thus we used THz profiles for a 3.9×0.2 mm filament with 8×10^{16} cm^{-3} maximum plasma density – Fig. 2.14(g), a 8.9×0.36 mm filament with 3×10^{16} cm^{-3} maximum plasma density – Fig. 2.14(h), a 13×0.2 mm filament with 2×10^{16} cm^{-3} maximum plasma density – Fig. 2.14(i), and a 35×0.08 mm filament with 6×10^{15} cm^{-3} maximum plasma density – Fig. 2.14(j). As can be clearly seen, also in these cases our model describes the experimental findings nicely and better than previously mentioned models. Another approach to explanation of the conical emission suggested in ref. [56], also predicts off-axis only THz generation.

2.5 Conclusion

In this chapter we presented a comprehensive study of plasma based THz sources. We used the FWM and the photocurrent models in order to study the generation of THz radiation by arbitrarily polarized two-color fields. We have shown that in the cases of linearly or circularly polarized ω and 2ω fields the predictions of the two models are qualitatively similar and reproduce the results of experiments as well as those of more rigorous theories. However, we have found that in the configuration where the ω field is elliptically polarized and the 2ω field is linearly polarized the predictions of the FWM and the photocurrent models show opposite behavior. This latter result enables the experimental verification on the dominating mechanism in such cases.

Finally, we proposed a physical model for the off-axis phase-matched THz generation in two-color filamentation. In particular, this model allows working with realistic plasma densities, includes the broadband nature of THz pulses from filaments and shows very good agreement not only with our experimental results, but also with many other experimental results in the literature. For all combinations of filament lengths and realistic maximum plasma densities the far field THz distributions have a donut-like shape, which is a new theoretical result confirmed by experiments. The angle of the conical emission drops with decreasing plasma electron density or increasing filament length. The total THz yield increases almost linearly with filament length, thus, the THz output can be effectively increased by extending the filament length with a constant plasma density. Also, the fact that lower THz frequencies find themselves at bigger cone angles allows one to use this effect for spatially tuned spectral filtering of the plasma filament generated THz radiation.

References

[1] D. Strickland and G. Mourou, Optics Communications **56**, 219 (1985), ISSN 00304018, arXiv:1011.1669v3.

[2] a. Braun, G. Korn, X. Liu, D. Du, J. Squier, and G. Mourou, Optics letters **20**, 73 (1995), ISSN 0146-9592.

[3] A. Couairon and A. Mysyrowicz, Physics Reports-Review Section of Physics Letters **441**, 47 (2007), URL {\T1\textless}GotoISI{\T1\textgreater}://000246088800001.

[4] P. Weinberger, Philosophical Magazine Letters **88**, 897 (2008), ISSN 0950-0839.

[5] P. L. Kelley, Physical Review Letters **15**, 1005 (1965), ISSN 0031-9007, arXiv: 1011.1669v3, URL http://link.aps.org/doi/10.1103/PhysRevLett.15.1005.

[6] G. Fibich, *Self-focusing: Past and Present*, vol. 114 (2009), ISBN 978-0-387-32147-9, URL http://link.springer.com/10.1007/978-0-387-34727-1.

[7] K. Y. Kim, I. Alexeev, and H. M. Milchberg, in *Physics of Plasmas* (2005), vol. 12, pp. 1–7, ISSN 1070664X.

[8] V. S. Popov, Physics-Uspekhi **47**, 855 (2004), ISSN 1063-7869, URL http://0-iopscience.iop.org.libraries.colorado.edu/1063-7869/47/9/R01$\ delimiter"026E30F$nhttp://0-iopscience.iop.org.libraries.colorado.edu/1063-7869/47/9/R01/pdf/1063-7869{_}47{_}9{_}R01.pdf.

[9] M. V. Ammosov, N. B. Delone, and V. P. Krainov, Sov. Phys. JETP **64**, 1191 (1986), ISSN 0044-4510.

[10] X.-C. Zhang and J. Xu, *Introduction to THz Wave Photonics*, vol. 53 (Springer US, Boston, MA, 2010), ISBN 978-1-4419-0977-0, arXiv:1011.1669v3, URL http://ebooks.cambridge.org/ref/id/CBO9781107415324A009http://link.springer.com/10.1007/978-1-4419-0978-7.

[11] T. I. Oh, Y. S. You, N. Jhajj, E. W. Rosenthal, H. M. Milchberg, and K. Y. Kim, Appl. Phys. Lett. **102**, 201113 (2013).

[12] E. Matsubara, M. Nagai, and M. Ashida, Applied Physics Letters **101**, 011105 (2012), ISSN 00036951, URL http://dx.doi.org/10.1063/1.4732524http://scitation.aip.org/content/aip/journal/apl/101/1/10.1063/1.4732524.

[13] T.-J. Wang, C. Marceau, Y. Chen, S. Yuan, F. Theberge, M. Chateauneuf, J. Dubois, and S. L. Chin, Applied Physics Letters **96**, 211113 (2010), URL http://dx.doi.org/10.1063/1.3441004.

[14] W.-M. Wang, S. Kawata, Z.-M. Sheng, Y.-T. Li, L.-M. Chen, L.-J. Qian, and J. Zhang, Optics letters **36**, 2608 (2011), ISSN 1539-4794, URL http://www.ncbi.nlm.nih.gov/pubmed/21765483.

[15] J.-F. F. Daigle, F. Théberge, M. Henriksson, T.-J. J. Wang, S. Yuan, M. Châteauneuf, J. Dubois, M. Piché, and S. L. Chin, Optics Express **20**, 6825 (2012), ISSN 1094-4087, URL http://www.opticsexpress.org/abstract.cfm?URI=oe-20-6-6825.

[16] D. J. Cook and R. M. Hochstrasser, Optics letters **25**, 1210 (2000), ISSN 0146-9592, URL http://dx.doi.org/10.1364/OL.25.001210http://www.opticsinfobase.org/abstract.cfm?URI=ol-25-16-1210http://ol.osa.org/abstract.cfm?URI=ol-25-16-1210.

[17] A. Nahata and T. F. Heinz, Optics Letters **23**, 67 (1998), ISSN 0146-9592, URL http://www.opticsinfobase.org/abstract.cfm?URI=ol-23-1-67.

[18] D. Cook, J. Chen, E. Morlino, and R. Hochstrasser, Chemical Physics Letters **309**, 221 (1999), ISSN 00092614, URL http://www.ncbi.nlm.nih.gov/pubmed/25361120http://linkinghub.elsevier.com/retrieve/pii/S0009261499006685.

[19] D. J. Cook, J.-X. Chen, and R. M. Hochstrasser, in *Ultrafast Phenomena XII* (Springer-Verlag, 2001), pp. 197–199.

[20] M. Kress, T. Löffler, S. Eden, M. Thomson, and H. G. Roskos, Optics Letters **29**, 1120 (2004).

[21] T. Bartel, P. Gaal, K. Reimann, M. Woerner, and T. Elsaesser, Optics Letters **30**, 2805 (2005), ISSN 0146-9592, URL http://ol.osa.org/abstract.cfm?URI=ol-30-20-2805http://dx.doi.org/10.1364/OL.30.002805http://www.opticsinfobase.org/abstract.cfm?URI=OL-30-20-2805.

[22] K.-Y. Kim, J. H. Glownia, A. J. Taylor, and G. Rodriguez, Optics express **15**, 4577 (2007).

[23] D. Dietze, J. Darmo, N. J. Heyman, A. Urich, and K. Unterrainer, CLEO/Europe - EQEC 2009 - European Conference on Lasers and Electro-Optics and the European Quantum Electronics Conference **26**, 2016 (2009), ISSN 0740-3224.

[24] F. Théberge, M. Châteauneuf, G. Roy, P. Mathieu, and J. Dubois, Physical Review A **81**, 033821 (2010), ISSN 1050-2947, URL http://link.aps.org/doi/10.1103/PhysRevA.81.033821.

[25] M. Li, W. Li, Y. Shi, P. Lu, H. Pan, and H. Zeng, Applied Physics Letters **101**, 161103 (2012), URL http://dx.doi.org/10.1063/1.4759268.

[26] L. Bergé, S. Skupin, C. Köhler, I. Babushkin, and J. Herrmann, Physical Review Letters **110**, 73901 (2013), URL http://link.aps.org/doi/10.1103/PhysRevLett.110.073901.

[27] A. V. Borodin, N. A. Panov, O. G. Kosareva, V. A. Andreeva, M. N. Esaulkov, V. A. Makarov, A. P. Shkurinov, S. L. Chin, and X. C. Zhang, Optics Letters **38**, 1906 (2013).

[28] Y. Nomura, Y.-T. Wang, A. Yabushita, C.-W. Luo, and T. Fuji, Optics Letters **1**, 1 (2015).

[29] V. Andreeva, O. Kosareva, N. Panov, D. Shipilo, P. Solyankin, M. Esaulkov, P. González de Alaiza Martínez, A. Shkurinov, V. Makarov, L. Bergé, et al., Physical Review Letters **116**, 063902 (2016), ISSN 0031-9007, URL http://link.aps.org/doi/10.1103/PhysRevLett.116.063902.

[30] M. Esaulkov, O. Kosareva, V. Makarov, N. Panov, and A. Shkurinov, Frontiers of Optoelectronics pp. 1–8 (2014), ISSN 2095-2759, URL http://link.springer.com/10.1007/s12200-014-0443-1.

[31] R. W. Boyd, *Nonlinear optics* (Academic Press, 2003), 3rd ed.

[32] I. Babushkin, W. Kuehn, C. Köhler, S. Skupin, L. Bergé, K. Reimann, M. Woerner, J. Herrmann, and T. Elsaesser, Physical Review Letters **105**, 053903 (2010), ISSN 0031-9007, URL http://dx.doi.org/10.1103/PhysRevLett.105.053903http://link.aps.org/doi/10.1103/PhysRevLett.105.053903.

[33] M. D. Thomson, M. Kress, T. Loffler, and H. G. Roskos, Laser & Photonics Reviews **1**, 349 (2007), URL {\T1\textless}GotoISI{\T1\textgreater}://000253904000004.

[34] J. Dai, N. Karpowicz, and X.-C. Zhang, Physical Review Letters **103**, 023001 (2009).

[35] X. Xie, J. M. Dai, and X.-C. C. Zhang, Physical Review Letters **96**, 075005 (2006), ISSN 0031-9007, URL http://dx.doi.org/10.1103/PhysRevLett.96.075005http://link.aps.org/doi/10.1103/PhysRevLett.96.075005{\T1\textless}GotoISI{\T1\textgreater}://000235554100041.

[36] K. Y. Kim, A. J. Taylor, J. H. Glownia, and G. Rodriguez, Nature Photonics **2**, 605 (2008), ISSN 1749-4885, URL http://dx.doi.org/10.1038/nphoton.2008.153http://www.nature.com/doifinder/10.1038/nphoton.2008.153{\T1\textless}GotoISI{\T1\textgreater}://000259649700010.

[37] Y. Chen, C. Marceau, S. Génier, F. Théberge, M. Châteauneuf, J. Dubois, and S. L. Chin, Optics Communications **282**, 4283 (2009), ISSN 00304018, URL http://linkinghub.elsevier.com/retrieve/pii/S0030401809007226.

[38] O. G. Kosareva, N. A. Panov, R. V. Volkov, V. A. Andreeva, A. V. Borodin, M. N. Esaulkov, Y. Chen, C. Marceau, V. A. Makarov, A. P. Shkurinov, et al., Journal of Infrared, Millimeter, and Terahertz Waves **32**, 1157 (2011).

[39] Y. S. You, T. I. Oh, and K.-Y. Kim, Opt. Lett. **38**, 1034 (2013), URL http://ol.osa.org/abstract.cfm?URI=ol-38-7-1034.

[40] Y.˜Liu, A.˜Houard, M.˜Durand, B.˜Prade, and A.˜Mysyrowicz, Opt. Express **17**, 11480 (2009).

[41] Y.˜S.˜You, T.˜I.˜Oh, and K.˜Y.˜Kim, Phys. Rev. Lett. **109**, 183902 (2012), URL http://link.aps.org/doi/10.1103/PhysRevLett.109.183902.

[42] J.-M.˜Manceau, A.˜Averchi, F. Bonaretti, D.˜Faccio, P.˜Di˜Trapani, A.˜Couairon, and S.˜Tzortzakis, Opt. Lett. **34**, 2165 (2009), URL http://www.opticsinfobase.org/ol/abstract.cfm?URI=ol-34-14-2165.

[43] K.˜Y.˜Kim, A.˜J.˜Taylor, J.˜H.˜Glownia, and G.˜Rodriguez, Nat. Photonics **2**, 605 (2008).

[44] C.˜D'Amico, A.˜Houard, S.˜Akturk, Y.˜Liu, J.˜Le˜Bloas, M.˜Franco, B.˜Prade, A.˜Couairon, V.˜T.˜Tikhonchuk, and A.˜Mysyrowicz, New J. Phys. **10**, 13015 (2008), URL http://iopscience.iop.org/1367-2630/10/1/013015.

[45] P.˜Sprangle, J.˜R.˜Penano, B.˜Hafizi, and C.˜A.˜Kapetanakos, Phys. Rev. E **69**, 66415 (2004), URL http://pre.aps.org/abstract/PRE/v69/i6/e066415.

[46] M.˜Chen, A.˜Pukhov, X.˜Y.˜Peng, and O.˜Willi, Phys. Rev. E **78**, 46406 (2008), URL http://pre.aps.org/abstract/PRE/v78/i4/e046406.

[47] B. Edlén, Metrologia **2**, 71 (1966), URL http://stacks.iop.org/0026-1394/2/i=2/a=002.

[48] N.˜A.˜Panov, O.˜G.˜Kosareva, V.˜A.˜Andreeva, A.˜B.˜Savel?ev, D.˜S.˜Uryupina, R.˜V.˜Volkov, V.˜A.˜Makarov, and A.˜P.˜Shkurinov, JETP Lett+ **93**, 638 (2011), URL http://link.springer.com/article/10.1134/S0021364011110099.

[49] ˜. Goodman, *Introduction to Fourier Optics* (McGraw-Hill Book Co. N.Y., 1968).

[50] A.˜Gorodetsky and V.G.˜Bespalov, SPIE Proc. Ser. **7601**, 760107 (2010), URL http://proceedings.spiedigitallibrary.org/proceeding.aspx?articleid=746106.

[51] D.˜Abdollahpour, S.˜Suntsov, D.˜G.˜Papazoglou, and S.˜Tzortzakis, Opt. Express **19**, 16866 (2011), URL http://www.opticsinfobase.org/oe/abstract.cfm?URI=oe-19-18-16866.

[52] V.˜Blank, M.˜D.˜Thomson, and H.˜G.˜Roskos, New J. Phys. **15**, 75023 (2013), URL http://iopscience.iop.org/1367-2630/15/7/075023.

[53] P.˜Klarskov, A.˜C.˜Strikwerda, K.˜Iwaszczuk, and P.˜U.˜Jepsen, New J. Phys. **15**, 75012 (2013), URL http://iopscience.iop.org/1367-2630/15/7/075012.

[54] A.V.˜Borodin, M.N.˜Esaulkov, I.I.˜Kuritsyn, I.A.˜Kotelnikov, and A.P.˜Shkurinov, J. Opt. Soc. Am. B **29**, 1911 (2012), URL http://josab.osa.org/abstract.cfm?URI=josab-29-8-1911.

[55] Y. Zhang, S. Wang, and X. Wang, **2**, 2 (????).

[56] L. A. Johnson, J. P. Palastro, T. M. Antonsen, and K. Y. Kim, Phys. Rev. A **88**, 63804 (2013), URL http://link.aps.org/doi/10.1103/PhysRevA.88.063804.

Chapter 3

Spectral bandwidth scaling laws and THz wave packets reconstruction

In this chapter we derive theoretically the scaling laws of the THz spectral bandwidth produced from two-color laser filaments as a function of the input laser pulse duration and find the spectrum loss-less limits for eo detection. Using this information we perform experiments by stretching the input laser pulse to the loss-less regime and then extrapolate the THz bandwidth and pulse duration at shorter input laser durations. Additionally, in order to correct also for the detector response function we apply an iterative reconstruction algorithm that implements a numerical simulation of the eo detection. Using this approach we are able to fully restore the original THz wave packet using only eo detection.

3.1 The effect of a limited bandwidth

At first let us demonstrate how the limited bandwidth of a detector affects our perception of a THz pulse. In our experiments we generate THz pulses using the two-color filamentation scheme. Our Ti:sapphire chirped-pulse amplification laser system generates 40 fs pulses, at 800 nm central wavelength and maximum energy 2.3 mJ. We focus the input laser pulse by a lens with 200 mm focal length, followed by a 50 μm thick β-barium borate (BBO) Type-I crystal cut at 29.9° angle, which generates the second harmonic. After the BBO crystal, at the focus of the lens, the two-color pulses create a plasma filament that emits THz radiation. In order to avoid the absorption in water vapor we place our setup into a purge gas chamber filled with dry air. Using a pair of parabolic mirrors we gather the emitted THz radiation in the far field and send it to a THz detector. To detect the generated THz pulses we apply either

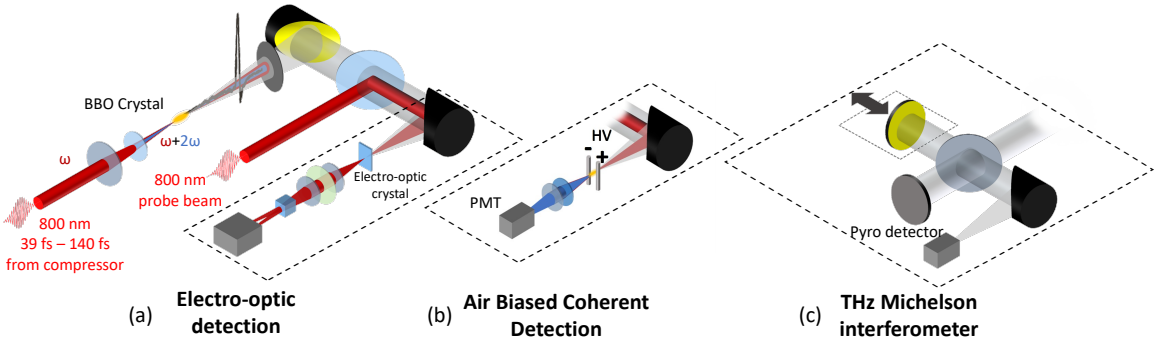

Fig. 3.1 Experimental setup for generating and detecting THz pulses through two-color filamentation in air. Tree different detection techniques were used: a) Electro-optic detection using a 500um thick ZnTe or a 100um thick GaP crystal, b) air biased coherent detection (ABCD) and c) Michelson interferometer.

eo detection or ABCD measurements. For eo detection we use 0.5 mm zinc telluride (ZnTe) and 100 μm gallium phosphide (GaP) crystals.

In addition to eo and ABCD measurements we also conducted measurements of the generated THz pulses using Michelson interferometry (field autocorrelation) as a reference method. We should stress that although Michelson interferometry is not a method of coherent detection (it cannot measure explicitly the phase of a THz pulse), it allows one though to detect the whole THz spectrum without limitations.

Figure 3.2 shows the THz fields and their amplitude spectra obtained by the different detection techniques. We see that the shortest spectrum is detected by the ZnTe crystal. It is followed by spectra measured by the GaP crystal and then by the ABCD measurement. The widest spectrum is registered by Michelson interferometry. The detection bandwidth of eo crystals is mainly restricted by their transverse optical phonon resonances. In ZnTe crystals the first phonon resonance is located at 5.3 THz and in GaP at 11 THz [1]. In turn, the detection bandwidth of the ABCD method can be estimated as the inverse duration of the probe pulse (the main limiting parameter). In our experiments, the duration of the probe pulse is about 70 fs (the probe pulse is longer than the input pulse due to the dispersion in the guiding optics) which corresponds to a detection bandwidth of about 14 THz.

In Fig. 3.2 we also see that the THz field measured by the different detection techniques have different durations and shapes. Defining the THz pulse duration τ_s as the full-width-half-maximum (FWHM) of the envelope of the modulus square of the detected THz field (measured signal), for the signals in Fig. 3.2 we have: 420 fs for the ZnTe crystal, 157 fs for the GaP crystal, and 77 fs for the ABCD method. Finally, from the Michelson interferometry signal and spectrum and assuming a transform limited pulse we obtain $\tau_s = 57$ fs, which can be safely considered as the shortest possible THz pulse duration in our experiments.

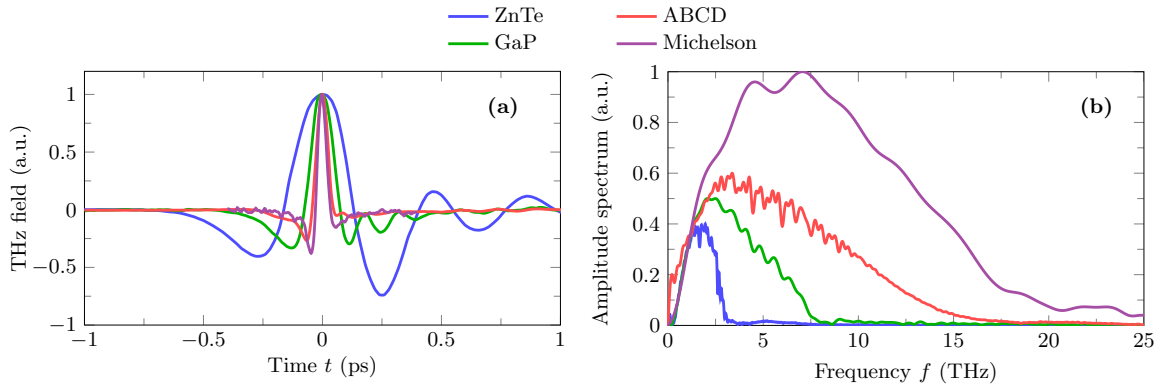

Fig. 3.2 Normalized THz fields (a) and their amplitude spectra (b) for a THz pulse measured by different techniques, namely, by ZnTe and GaP eo crystals, as well as by the ABCD method and Michelson interferometry (the spectra are independently normalized appropriately for clarity reasons).

Thus, even using the best of our eo crystals the measured THz pulse duration is two to three times larger than its real value. In addition, the signal from the eo detectors leads us to wrong conclusions about the shape of the original THz pulses. Figure 3.2 shows that both ZnTe and GaP crystals predict additional field oscillations that are absent on the signal measured by the more precise ABCD method. Thus, the eo detection, although it presents very high sensitivity, strongly affects our perception of the THz electric field deforming its original shape and misleading about its duration.

3.2 Scaling laws for the THz spectral bandwidth

In this section we find the laws according to which the spectral bandwidth and duration of the generated THz pulse depend on the duration of the input laser pulse. In order to find these laws we use the well accepted photocurrent model [2]. Since experimentally it is convenient to increase the laser pulse duration by changing the distance between the gratings of the laser compressor, the resulting pulse becomes chirped. Therefore, to write the field of the main harmonic we use the following expression:

$$E_{\omega 0}(t) = A_{\omega_0} \frac{\sqrt{1+iC}}{\sqrt{1+C^2}} \exp\left[-(1+iC)2\ln 2 \frac{t^2}{\tau_i^2}\right] e^{-i\omega_0 t}, \tag{3.1}$$

where C is the chirp parameter, with $\tau_i = t_i\sqrt{1+C^2}$ and t_i being the FWHM durations of the stretched and transform-limited input laser pulse. The field of the second harmonic is

calculated as

$$E_{2\omega_0}(t) = \frac{\sqrt{I_{2\omega_0}/I_{\omega_0}}}{|E_{\omega_0}(t=0)|} E^2_{\omega_0}(t) e^{-i\pi/2}, \tag{3.2}$$

where the prefactor is chosen so in order to fix the ratio of the intensities $I_{\omega_0} = n_0 \varepsilon_0 c_0 A^2_{\omega_0}/2$ and $I_{2\omega_0}$ of the main and second harmonic, respectively. The initial conditions in our calculations are $E(t) = E_{\omega 0}(t) + E_{2\omega 0}(t)$, $\lambda_0 = 800\,\text{nm}$, and the intensity of the main and second harmonics are $I_{\omega_0} = 5 \times 10^{13}\,\text{W/cm}^2$ and $I_{2\omega_0} = 0.2 I_{\omega_0}$ respectively.

The photocurrent derivative $\partial J/\partial t$ is calculated assuming that the medium consists of N_2 molecules with the concentration $2.68 \times 10^{19}\,\text{cm}^{-3}$. For the generated THz pulse we consider a waveform that corresponds to the spectrum of $\partial J/\partial t$ at frequencies below 100 THz.

Since the initial two-color pulse is chirped, we need to take into account that its phase is strongly modulated. Therefore, in order to avoid errors in calculations of the amount of free electrons, we use a phase sensitive nonadiabatic ionization rate proposed by Yudin and Ivanov [3].

Figure 3.3 shows the dependence of the FWHM bandwidth of the power spectrum (a) and duration (inversed bandwidth) (b) of the generated THz pulse as a function of the FWHM duration τ_i of the input laser pulse. The three curves correspond to three different initial (non chirped) laser pulse durations, $t_i = 30$, 40 and 50 fs respectively, in order to show that the analysis is independent of the initial laser pulse duration. One can see that the duration of the THz pulse has an astonishing simple linear dependence on the duration of the input laser pulse. Similar indications have been reported in [4]. In Fig. 3.3 we also have indicated the spectral bandwidth limits of the various techniques so one can easily identify what needs to be the laser pulse duration in order to be within the limits of each detector. For instance for eo detection with a GaP crystal one should have laser pulse durations above $\sim$90 fs and for the ZnTe above $\sim$180 fs.

Thus, form the previous discussion it becomes clear which way we should proceed in order to find the duration of the THz pulse in our experiment. We need to stretch our input laser pulse above the duration that corresponds to the spectrum loss-less detection regime, measure the THz pulse duration there and then use the scaling laws we have just derived to find the corresponding THz pulse duration for shorter input laser pulses.

We need to stress though that even if the bandwidth of the eo detector is broad enough and one operates in the spectrum loss-less regime, the THz pulse will still be distorted, into other, because of the chromatic dispersion and spectral sensitivity of the eo crystal. These effects though can be easily modeled and accounted for as we show in the next section.

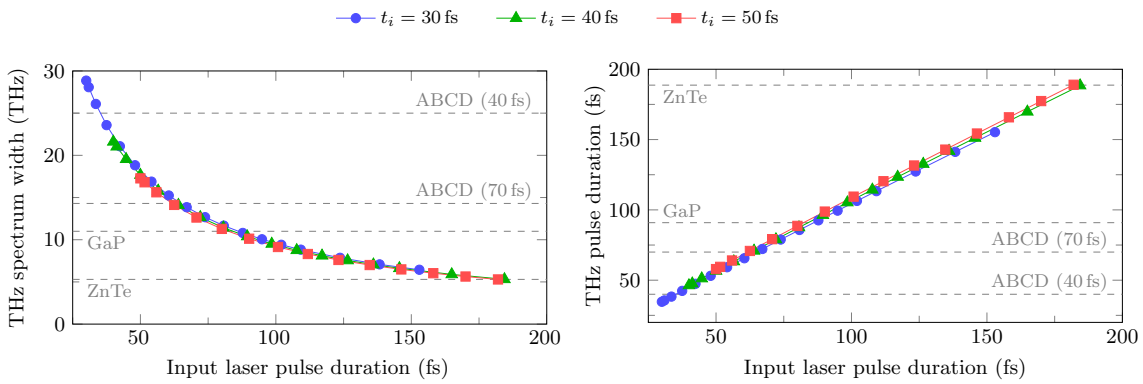

Fig. 3.3 The dependence of the spectral bandwidth (a) and duration (inversed bandwidth) (b) of the generated THz pulse on the FWHM duration τ_i of the input laser pulse. Dashed lines indicate the limits of the various detection techniques. The ABCD method's limits are shown for two probe beam pulse durations, 70 and 40 fs.

3.3 The reconstruction method

In this section we introduce a reconstruction method whose aim is to restore the broadband THz wave packets that were distorted by the propagation through an eo detector (in the spectrum loss-less case).

The eo sampling technique is based on measuring the birefringence induced by the THz field inside the detection crystal as a function of time. The technique has been extensively studied in the past, e.g. [5, 1], and below we describe the methodology one needs to use to correctly model it.

A laser probe beam experiences polarization changes during its propagation through the detection crystal. After the crystal the probe beam is splitted into two components with mutually perpendicular polarizations and sent to a pair of balanced photodiodes. Let us denote the voltage in each of the photodiodes as A_1 and A_2. A normalized difference of A_1 and A_2 is given by [5]

$$\frac{A_1 - A_2}{A_1 + A_2} = \sin\Gamma, \tag{3.3}$$

where Γ is a relative phase shift between the two orthogonally polarized components of the probe beam. We can write Γ as [1]

$$\Gamma(t) = \frac{2\pi n_0^3 d}{\lambda_0}\mathrm{Re}[F(t)], \tag{3.4}$$

where λ_0 is the wavelength of the probe beam, n_0 is the refractive index of the detection crystal at λ_0, and d is the crystal thickness. For a GaP crystal at $\lambda_0 = 800\,\text{nm}$ we have $n_0 = 3.18$ [1]. The factor $\text{Re}[F(t)]$ in Eq. (3.4) denotes the real part of the function $F(t)$, which we define as

$$F(t) = \frac{1}{2\pi} \int_{-\infty}^{\infty} H(\omega)\, \widetilde{E}(\omega) e^{-i\omega t} d\omega. \tag{3.5}$$

Here $\widetilde{E}(\omega)$ is the spectrum of the incoming THz pulse with electric field $E(t)$, that is,

$$\widetilde{E}(\omega) = \int_{-\infty}^{\infty} E(t) e^{i\omega t} dt \tag{3.6}$$

and $H(\omega)$ is the eo response function, given by [1]

$$H(\omega) = r_{41}(\omega)\, G(\omega)\, T(\omega), \tag{3.7}$$

where $r_{41}(\omega)$, $G(\omega)$, and $T(\omega)$ are the frequency dependent eo coefficient, the geometric response function, and the transmission coefficient of the detection crystal, respectively.

The transmission coefficient $T(\omega)$ reads as

$$T = \frac{t_1 t_2 e^{ikd}}{1 + r_1 r_2 e^{2ikd}}. \tag{3.8}$$

If we assume that the detection crystal is surrounded by dry air with a unity refractive index, then $t_1 = 2/(1+n)$, $t_2 = 2n/(n+1)$, and $r_1 = (1-n)/(1+n)$, $r_2 = (n-1)/(n+1)$, where n is the refractive index of the detection crystal at THz frequencies with $k = n\omega/c_0$ being the wave number of the THz pulse.

For the frequency dependent refractive index n we use the following model [1]:

$$n^2(\omega) = \varepsilon_{el} + \frac{S_0 \omega_0^2}{\omega_0^2 - \omega^2 - i\Lambda_0 \omega}. \tag{3.9}$$

In the case of GaP crystals $\varepsilon_{el} = 8.7$, $S_0 = 1.8$, $\omega_0/(2\pi) = 10.98\,\text{THz}$, and $\Lambda_0/(2\pi) = 0.02\,\text{THz}$ [1].

The geometric response function $G(\omega)$ takes into account the mismatch between the phase velocity of the THz pulse and group velocity v_g of the probe laser pulse inside the

detection crystal [1]:

$$G(\omega) = \frac{1}{d}\int_0^d dz \int_{-\infty}^{\infty} \delta(z/v_g - t) e^{i(kz-\omega t)} dt$$
$$= \frac{1}{d}\frac{e^{i(k-\omega/v_g)d} - 1}{i(k-\omega/v_g)}. \tag{3.10}$$

For a probe pulse at $\lambda_0 = 800\,\text{nm}$ propagating inside a GaP crystal $v_g = 0.28c_0$ [1].

The eo coefficient r_{41} determines the sensitivity of the detection crystal at different frequencies. We use the following model for r_{41} [1]:

$$r_{41}(\omega) = d_E\left(1 + \frac{C\omega_0^2}{\omega_0^2 - \omega^2 - i\Lambda_0\omega}\right) \tag{3.11}$$

with the same parameters ω_0 and Λ_0 as in the model for $n(\omega)$. For GaP crystals $d_E = 1.13 \times 10^{-12}\,\text{m/V}$ and $C = -0.47$. These values of d_E and C differ slightly from the ones proposed in [1]. We modified the original values in order to shift the frequency where the real part of r_{41} becomes zero. This correction gives a better fit for our experimental data.

Equations (3.3)–(3.11) allow us to simulate the process of eo sampling for any given THz pulse. For an electric field $E(t)$ of the initial THz pulse, the algorithm performs the following steps: (i) calculates the spectrum $\widetilde{E}(\omega)$ of $E(t)$ in accordance with Eq. (3.6); (ii) using Eqs. (3.8)–(3.11), calculates the eo coefficient $r_{41}(\omega)$, the geometric response function $G(\omega)$, and the transmission coefficient $T(\omega)$; (iii) calculates the eo response function $H(\omega)$ from Eq. (3.7) and then the function $F(t)$ from Eq. (3.5); (iv) using Eq. (3.4), calculates the phase shift $\Gamma(t)$. Finally, the sine of Γ, according to Eq. (3.3), gives us the eo signal that can be directly compared with the experimental data.

In order to choose a model for our THz pulse that enters the eo detection system we turn to the results of the ABCD method (see Fig. 3.2). The signals show that the original THz pulse would be a single cycle pulse, whose electric field $E(t)$ can be modeled by the following function:

$$E(t) = E_0 \frac{t}{t_0} \exp\left(-\frac{t^2}{t_0^2}\right), \tag{3.12}$$

where E_0 is the peak amplitude. The FWHM of the envelope of the modulus square of $E(t)$ in (3.12) is $\tau_0 = 1.81t_0$.

To fit the experimental results we use a nonlinear curve fitting process which runs iteratively, until convergence, the above algorithm with Eq. (3.12) as the initial condition

and only fitting parameters the duration τ_0 of the initial THz pulse and the thickness d of the eo crystal. We consider d as a fitting parameter in order to compensate errors rising from inaccurate determination of the crystal's thickness together with possible misalignment of the crystal relative to the optical axis. As initial estimates for τ_0 and d we use the duration of the recorded THz signal and the thickness of the eo crystal provided by its manufacturer. At this stage of the reconstruction we do not take into account the absolute value of the amplitude E_0 and consider only normalized values.

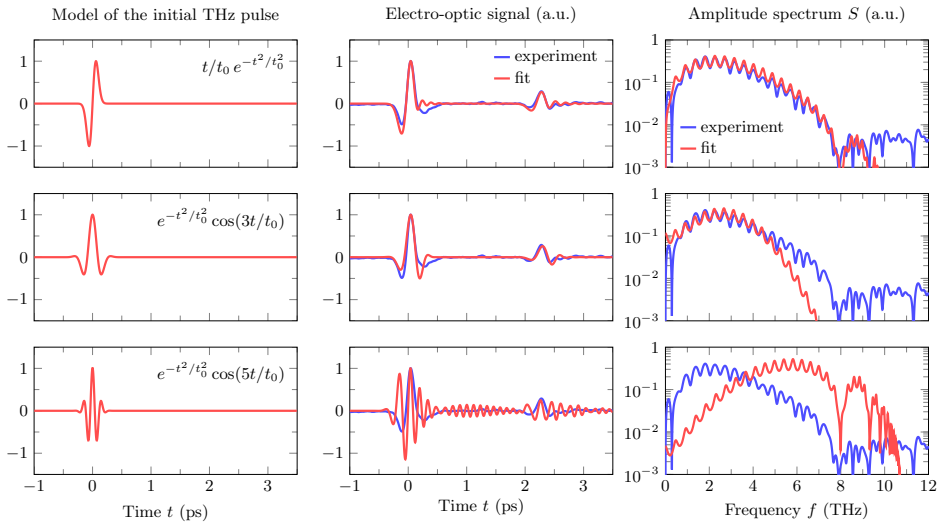

Fig. 3.4 The THz signal measured by 100 µm Gap crystal (middle column) and its amplitude spectrum (right column) together with their best fits obtained by the reconstruction method for different models of the initial THz pulse (left column). The echoes seen in the measured fields (middle column) come from the finite thickness of the eo crystal and are actually useful in the fitting process since the resulting Fabry-Perot interference fringes in the spectra (right column) fix the thickness of the crystal.

In order to test our reconstruction method, we apply it to the signal measured by a 100 μm GaP crystal and for an input laser pulse of 108 fs, which is in the spectrum loss-less regime as shown in Fig. 3.3.

In Fig. 3.4 we plot the experimentally measured THz signal (middle column) and its amplitude spectrum (right column) together with their best fits obtained by our reconstruction method for three different models of the initial pulse (left column). One can clearly see that the model from Eq. (3.12) (top raw) gives the closest agreement with the experimental findings. The duration τ_0 of the original THz pulse, restored by our reconstruction method, is equal to 147 fs, while the duration of the experimental signal is 185 fs. Thus, if we provide spectrum loss-less measurements our reconstruction algorithm is able to nicely recover the shape and duration of the original THz pulse that was distorted by the propagation inside an eo crystal.

3.4 Retrieval of the original THz pulse duration

In this section we combine the analysis of sections 3.2 and 3.3 in order to retrieve the duration of the THz pulse generated in our system by transform-limited laser pulses with duration 40 fs. For this purpose we conducted a series of experiments where we stretched our input laser pulses above durations that allow one to reach the detector spectrum loss-less regime.

For each experiment in the series we measured the duration τ_i of the input laser pulse and detect the corresponding generated THz pulses with a 100 μm GaP crystal. Then for the recorded eo signals that belongs to the loss-less regime of detection we applied our reconstruction method and retrieved the duration τ_0 of the original THz pulse.

Figure 3.5 shows the duration τ_s of the THz signal measured by the GaP crystal (blue dots) and the corresponding value τ_0 retrieved by our reconstruction method for laser pulse durations τ_i above 100 fs (green triangles). As a reference data, in this figure we also plot the duration τ_s measured by the ABCD method (golden square) and the Michelson interferometer (purple pentagon) for the shortest initial laser pulse.

In Fig. 3.5 we see that for the input laser pulses whose duration τ_i exceeds 100 fs, the values of τ_0 retrieved by our reconstruction method depend linearly on τ_i as expected from our theoretical results in section 3.2. Thus, we can confidently extrapolate linearly the THz pulse durations for the shorter laser pulse durations, represented by the red triangles in Fig. 3.5. The obtained dependence of the THz pulse duration on the input laser pulse duration is then given by

$$\tau_0 = a\tau_i + b, \tag{3.13}$$

with $a = 1.16$ and $b = 21.49$ (for τ_0 and τ_i in femtoseconds). Using Eq. (3.13) we find that for our shortest initial laser pulse ($\tau_i = 40$ fs) the generated THz pulse has duration $\tau_0 = 68$ fs. This value is in-between the duration of 57 fs estimated by the Michelson interferometry and the ABCD measurement of 77 fs, as could be expected.

One may consider that Eq. (3.13) is specific to our experimental conditions only. In order to verify this point we performed additional simulations, as the ones described in section 3.2, for different laser peak intensities, in the range $I_{\omega_0} = 10^{13} - 10^{14}$ W/cm^2, as well as for different $I_{2\omega_0}/I_{\omega_0}$ ratios. We found that Eq. (3.13) is always valid with practically the same value of a while b has a variance of ± 5 fs. This would suggest that if one uses Eq. (3.13) with our experimentally extracted values of a and b to calculate the THz pulse duration resulting from 2-color filaments in gases under different experimental conditions the obtained result would still be close to the real one within an error of 10-20%, something

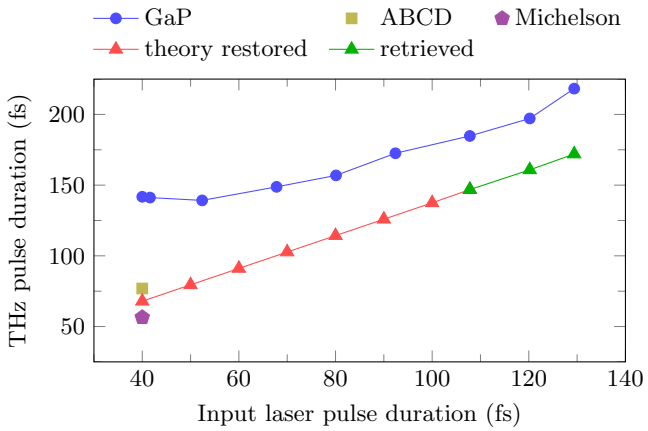

Fig. 3.5 THz pulse duration τ_s measured with a GaP eo crystal (blue dots) and the corresponding restored duration τ_0 (red and green triangles), as a function of the input laser pulse duration τ_i.

that we have validated with published results of ABCD measurements (that are closer to the real THz pulse durations) found in the literature [6–8].

3.5 Absolute amplitude of the THz pulse

In the previous section we have shown how to retrieve the shape and duration of the original THz pulse distorted by an eo detector. If, additionally, one can find a way to retrieve the absolute amplitude E_0, then all the information about the original THz wave packet will be known. There are two standard methods to calculate the absolute amplitude E_0 of a THz electric field if one uses eo detection. In order to apply the first method we need to measure the total energy of a THz pulse. Additionally, for the same pulse, we need to measure its spatial distribution and eo signal, then normalize them and integrate. The desired amplitude E_0 can be found if we divide the total THz energy by the two calculated integrals [9].

The second method is based on a simplified version of the theory of eo detection (see section 3.3) where we neglect the dispersion inside the eo crystal. As a result of this simplification, we find that the peak of an eo signal corresponds to a relative phase shift Γ given by [1]

$$\Gamma = \frac{2\pi n_0^3 d}{\lambda_0} r_{41} E_0, \tag{3.14}$$

where r_{41} is calculated at some specific frequency. The resulting value of E_0 is then calculated by Eq. (3.3), using the readings from the balanced photodiodes of the eo detection setup.

Both these methods have substantial disadvantages. In the first method we assume that the temporal distribution of the THz field is well represented by an eo signal which, as we

have already seen, is not true. Moreover, this method demands additional measurements of the spatial profile of the THz pulse. In turn, the second method does not take into account the dispersion inside the eo crystal.

As an alternative to the existing methods, we can calculate the absolute amplitude of the THz electric field using our reconstruction method. The calculation stages are the following. First, using a normalized eo signal we restore the duration τ_0 of the original THz pulse, thereby obtaining its shape, that is, its normalized electric field. Then, we simulate the eo signal for a THz pulse with the restored τ_0 and unity amplitude, say 1 kV/cm. As a result, for a given THz pulse with a given τ_0, we find the relation between the absolute amplitude E_0 (in physical units) and the peak value of the relative phase shift Γ. The final scaling can be done using Eq. (3.3) and the readings from the balanced photodiodes. Thus our result will be the closest one to the actual value of the absolute amplitude, since it does not depend on additional measurements of the pulse profile and takes into account the distortions introduced by the eo detector including the dispersion of the eo crystal.

Following the above procedure, we find that our THz pulse with duration $\tau_0 = 68$ fs has peak amplitude E_0 equal to 250 kV/cm. For comparison, the amplitude calculated using Eq. (3.14) is equal to 70 kV/cm, which is three times lower than the value obtained by our reconstruction method.

3.6 Conclusion

In this chapter, we have shown that one can fully retrieve the ultrashort broadband THz wave packets produced by two-color laser filaments even when using dispersive and bandwidth lossy detection channels, like the very popular electro-optic detection. This was made possible by identifying the THz spectrum bandwidth scaling laws as a function of the input laser pulse duration and by correcting for the electro-optic detection distortions using an iterative nonlinear curve fitting algorithm. Our results beyond the evident impact on THz science and technology can open the way in suggesting similar solutions to other problems where only partial information of wave packets and wave functions can be measured.

References

[1] S Casalbuoni, H Schlarb, B Schmidt, P Schmüser, B Steffen, and A Winter. Numerical studies on the electro-optic detection of femtosecond electron bunches. *Physical Review Special Topics - Accelerators and Beams*, 11:72802, 2008.

[2] Ki-Yong Kim, James H Glownia, Antoinette J Taylor, and George Rodriguez. Terahertz emission from ultrafast ionizing air in symmetry-broken laser fields. *Optics Express*, 15:4577–4584, 2007.

[3] Gennady L Yudin and Misha Yu Ivanov. Nonadiabatic tunnel ionization: Looking inside a laser cycle. *Phys. Rev. A*, 64:13409, 2001.

[4] A V Borodin, N A Panov, O G Kosareva, V A Andreeva, M N Esaulkov, V A Makarov, A P Shkurinov, S L Chin, and X C Zhang. Transformation of terahertz spectra emitted from dual-frequency femtosecond pulse interaction in gases. *Optics Letters*, 38(11):1906–1908, 2013.

[5] M Brunken, H Genz, C Hessler, H Loos, A Richter, P Göttlicher, M Hüning, H Schlarb, S Simrock, P Schmüser, D Suetterlin, M Tonutti, and D Türke. Electro-Optic Sampling at the TESLA Test Accelerator: Experimental Setup and First Results. Technical report, TESLA Technology Collaboration, 2003.

[6] Jianming Dai, Jingle Liu, and Xi-Cheng Zhang. Terahertz Wave Air Photonics: Terahertz Wave Generation and Detection With Laser-Induced Gas Plasma. *IEEE Journal of Selected Topics in Quantum Electronics*, 17:183–190, 2011.

[7] Xiaofei Lu and X.-C. Zhang. Balanced terahertz wave air-biased-coherent-detection. *Appl. Phys. Lett.*, 98:151111, 2011.

[8] I Chen Ho and Xi Cheng Zhang. Application of broadband terahertz spectroscopy in semiconductor nonlinear dynamics. *Frontiers of Optoelectronics*, 7(2):220–242, 2014.

[9] F Blanchard, G Sharma, X Ropagnol, L Razzari, R Morandotti, and T Ozaki. Improved terahertz two-color plasma sources pumped by high intensity laser beam. *Optics Express*, 17:6044–6052, 2009.

Chapter 4

Abruptly autofocusing beams:harmonics and THz generation

4.1 Abruptly auto focusing beams

The focusing characteristics of optical beams have always been an issue of great practical importance [1]. Often, optical waves are used as a means of energy delivery on a remote target. In general, a wave tends to focus or defocus whenever its initial phase and/or amplitude have been suitably manipulated. In many applications, a Gaussian or top-hat beam is focused on a remote target by the use of a focusing element that reshapes the beam's wave-front. The main drawback of this approach is the gradual increase in the peak intensity as the focus is approached. For many applications it is crucial that a beam abruptly focuses its energy right before a target while maintaining a low intensity profile until that very moment.

Ideally, this can be accomplished by inducing an asymmetry in the longitudinal intensity profile so that the energy is abruptly delivered to the focus exactly the way that is described above. Recently, a new family of abruptly autofocusing waves was theoretically proposed [2]. These waves exhibit interesting focusing characteristics since, close to the focal point, they undergo an abrupt increase in their intensity. Because of the nature of these waves, the caustic of the intensity maxima converges in a nonlinear fashion toward the focus. Because of the nature of these waves, the caustic of the intensity maxima converges in a nonlinear fashion toward the focus.

One member of this family is the ring-Airy beams with a radially symmetric Airy intensity distribution. In this case, the intensity maxima follow a parabolic trajectory [2, 3]. After the first experimental verification of this behavior [4] it is known that the intensity contrast achieved is much higher than that of a typical Gaussian beam. A wide range of applications

are thus possible, such as medical laser treatment, microparticle trapping, and temporal cloaking that were discussed in numerous reports [5–7]. The amplitude of a ring airy beam can be described as:

$$u_\omega(r,0) = u_0 Ai(\rho) e^{\alpha\rho} \tag{4.1}$$

where u_0 is the amplitude, $Ai()$ is the Airy function, $\rho \equiv (r_0 - r)/w$ and r_0, w, a are respectively the primary ring radius, width and apodization parameters. The direct generation of the radially symmetric Airy distribution is not a trivial task, since combined phase and amplitude modulation are required. Alternatively, such a distribution can be generated thought the Fourier transform (FT) of a properly modulated input wave. This approach was successfully applied in generating one-dimensional (1D) and two-dimensional (2D) Airy beams [3, 8, 9]. In this latter case, the FT is a Gaussian beam modulated by a cubic phase so only phase modulation is required. On the other hand, the FT of the radially symmetric Airy distribution, which cannot be described by a simple analytical form, is a Bessel-like distribution with a central peak surrounded by decaying amplitude rings [2]. Although this distribution changes signs as a function of the radius, it can be generated [4] by encoding both amplitude and

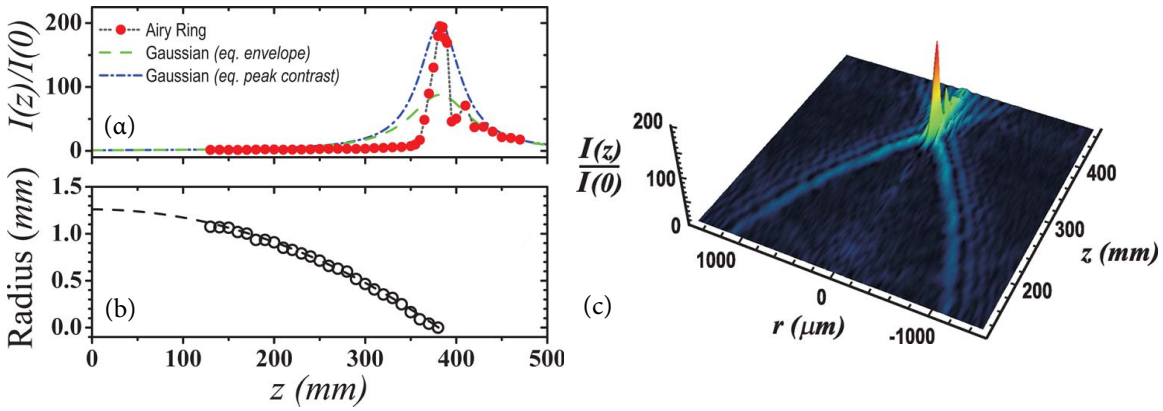

Fig. 4.1 (a) Intensity contrast as a function of the propagation distance: solid circles, experimental values; dashed curve and dashed–dotted curve, intensity contrast of equivalent Gaussian beams. (b) Radius of the ring Airy as a function of the propagation distance. (c) Radially averaged intensity as a function of the propagation distance. Taken by [4].

phase information onto a phase-only filter using a technique proposed by Davis et al. [10]. This versatile technique is based on the idea that the phase modulation of a diffracting phase element leads to a spatial modulation of its diffraction efficiency so that energy is selectively transferred between the diffraction orders, more specifically, the zero and first orders, allowing the modulation of their amplitude. Phase modulation of an optical wave can be easily achieved by a spatial light modulator (SLM) or by the use specially designed amplitude/phase masks.

Papazoglou et.al [4] showed that the intensity peak follows a curved trajectory as the wave propagates toward the focus while the intensity contrast is abruptly increased at the focus, as expected [2]. It is interesting to note here that the autofocusing is an inherent property of the wave. Fig.4.1 (c) shows the intensity contrast, defined as the ratio of the peak intensity along the propagation to the peak intensity at the Fourier. Fig.4.1 (a) shows the intensity contrast as a function of the propagation distance of the generated Airy ring in comparison to an equivalent (theoretically calculated) Gaussian beam that is focused using a lens of equal focal distance of the autofocusing Airy ring while the radius of the primary Airy ring as a function of the propagation distance is shown in Fig.4.1 (b).

4.2 Harmonics generation of abruptly autofocusing beams

Several works were published studying accelerating 1D Airy beams within nonlinear media. Experiments with Airy beams in quadratic media including the generation and manipulation of Airy beams through engineered periodic poling [11, 12] and three-wave-mixing of Airy beams were reported [13–15]. Second harmonic generation of 1D and 2D Airy beams was also reported in quadratic nonlinear media [16] where they showed that fundamental and second harmonic exhibit joint self-similar acceleration within the nonlinear medium, but with intensity peaks that are asynchronous with respect to one another. Nevertheless, interactions of ring-Airy beams with non-linear crystals as well as possible applications have not been investigated yet. Next, we examine high harmonics generation in a non-linear crystal using abruptly auto focusing beams and we propose general analytic formulas for second and higher harmonics generation. Specifically for second harmonic, generation and propagation of a ring-Airy beam is studied experimentally under free propagating and extra focusing conditions.

4.2.1 Theoretical description

Starting from equation 4.1 and without loss of generality the amplitude of the generated 2nd harmonic in a thin BBO crystal is given by:

$$u_{2\omega}(r,0) = \chi^{(2)} u_{\omega}(r,0)^2 = \chi^{(2)} u_0^2 Ai(\rho)^2 e^{2\alpha\rho} \tag{4.2}$$

where $\chi^{(2)}$ is the nonlinear susceptibility. By using a well-known approximation of the Airy function, $Ai(-x) \cong \sin(\frac{2}{3}x^{3/2} + \frac{\pi}{4})x^{-1/4}/\sqrt{\pi}$, we can expand (D. G. Papazoglou, personal

communication) the term $Ai()^2$ in equation 4.2:

$$Ai(\rho)^2 \cong 2(\rho)^2 + E(\rho)Ai(\hat{S}\cdot\rho) \equiv Ai_2^{\alpha}(\rho) \tag{4.3}$$

where $E(\rho) \equiv \frac{1}{2\sqrt{\pi}}\frac{1}{f(\rho)^{1/4}}$, $\hat{S}$ is a linear scaling operator $\hat{S}\cdot\rho \equiv 2^{2/3}\rho + \frac{\pi}{8\cdot 2^{1/3}}$ and $f()$ is an apodization function:

$$f(x) = \begin{cases} x & \text{x} < -\frac{6}{5} \\ \frac{6}{5} - e^{-4} + e^{4x} & \text{x} \geq -\frac{6}{5} \end{cases}$$

Using the approximation of eq. 4.3 we can write for the second harmonic:

$$u_{2\omega}(r,0) \cong \frac{1}{2\pi}\chi^{(2)}u_0^2 e^{2\alpha\frac{r_0-r}{w}}\frac{1}{f(\frac{r_0-r}{w})^{1/2}} + \frac{e^{-\pi\alpha/8}}{2/\sqrt{\pi}}\chi^{(2)}u_0^2\frac{1}{f(\rho)^{1/4}}Ai(\frac{r_0'-r}{w'})e^{\sqrt[3]{2}\alpha\frac{r_0'-r}{w'}} \tag{4.5}$$

where $r_0' = r_0 + \frac{\pi}{16}$ and $w' = 2^{-2/3}$. Thus the amplitude of the generated second harmonic can be analyzed into 2 terms, a smooth pedestal that does not exhibit any autofocusing behavior and a ring-Airy term that is strongly apodized. This term contains a ring-Airy (with different scaling factors, i.e radius and width compared to the 1st harmonic) that is apodized stronger (25% larger exponential apodization factor and further radial ($\sim$ radius$^{-1/4}$) apodization factor).

Without the presence of a focusing lens the ω ring-Airy and the $a\omega$ ring-Airy component will auto focus at positions that can be predicted [3, 4, 17] by the 1D analytical formulas, so for the autofocusing position of ω we get:

$$f_{Ai}^{\omega} = 4\pi\frac{w^2}{\lambda}\sqrt{r_0/w+1} \cong 4\pi\frac{w^{3/2}}{\lambda}\sqrt{r_0}, \quad r_0 \gg w \tag{4.6}$$

On the other hand, to estimate the autofocus position of the 2ω we replace w and r_0 in the above equation with w' and r_0' to get:

$$f_{Ai}^{2\omega} = 4\pi\frac{w'^{3/2}}{\lambda/2}\sqrt{r_0'} = 4\pi\frac{w^{3/2}}{\lambda}\sqrt{r_0} = f_{Ai}^{\omega}. \tag{4.7}$$

Interestingly, the ring-airy component of the 2ω will autofocus at exactly the same position with the generating ω ring-Airy.

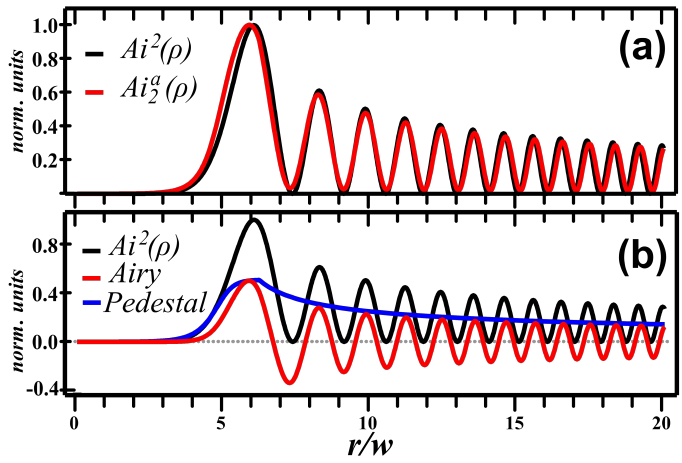

Fig. 4.2 Approximation of the $Ai()^2$ function. (a) comparison of $Ai(\rho)^2$ to the approximation $Ai_2^{\alpha}(\rho)$ (b) decomposition of the approximation to the airy $E(\rho)Ai(\hat{S}\cdot\rho)$ and the pedestal terms $2E(\rho)^2$ respectively

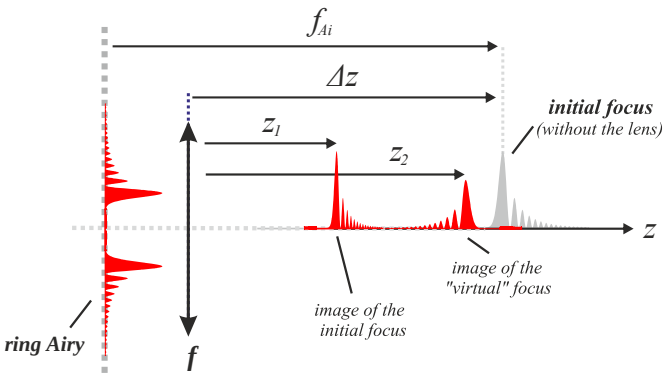

Fig. 4.3 Focusing of a ring Airy beam by a thin lens. As in the case of all Janus waves two focal regions are observed [18]

On the other hand, to increase the efficiency of the process, the generating ω ring-Airy is focused using a lens. Since ring –Airy beams are Janus waves [18] they exhibit a double focus while the position of the primary foci can be well predicted by simple imaging formulas. As shown in Fig. 2 if we assume that a thin lens is located at a distance Δz from the focus of the ring-Airy beam we get two foci at positions [18] z_1, z_2 relative to the lens:

$$z_1 = (\frac{\Delta\tilde{z}}{\Delta\tilde{z}+\tilde{f}})f, \quad z_2 = (\frac{\Delta\tilde{z}-2}{\Delta\tilde{z}-2+\tilde{f}})f \tag{4.8}$$

where, $\Delta\tilde{z} \equiv \Delta z/f_{Ai} < 1, \tilde{f} \equiv f/f_{Ai}$ are respectively the distance Δz and the focal distance of the lens normalized over the ring-Airy focal distance. Appling this to the case of the ω

ring-Airy we get two foci at positions $z_1^{\omega}, z_2^{\omega}$:

$$z_1^{\omega} = (\frac{\Delta\tilde{z}^{\omega}}{\Delta\tilde{z}^{\omega} + \tilde{f}^{\omega}})f, \quad z_2^{\omega} = (\frac{\Delta\tilde{z}^{\omega} - 2}{\Delta\tilde{z}^{\omega} - 2 + \tilde{f}^{\omega}})f, \quad \tilde{f}_{\omega} \equiv f/f_{Ai}^{\omega}, \quad \Delta\tilde{z}^{\omega} \equiv \Delta z/f_{Ai}^{\omega} \tag{4.9}$$

In the case of the second harmonic the situation is more complex. The 2ω ring-Airy term will lead to two foci at positions $z_1^{2\omega}, z_2^{2\omega}$ while the smooth pedestal term will focus at position $z_3^{2\omega}$:

$$\begin{gathered} z_1^{2\omega} = (\frac{\Delta\tilde{z}^{2\omega}}{\Delta\tilde{z}^{2\omega} + \tilde{f}_{2\omega}})f \cong z_1^{\omega}, \quad z_2^{2\omega} = (\frac{\Delta\tilde{z}^{2\omega} - 2}{\Delta\tilde{z}^{2\omega} - 2 + \tilde{f}_{2\omega}})f \cong z_2^{\omega}, \quad z_3^{2\omega} \cong f, \\ \tilde{f}_{2\omega} \equiv f/f_{Ai}^{2\omega} \cong \tilde{f}_{\omega}, \quad \Delta\tilde{z}^{2\omega} \equiv \Delta z/f_{Ai}^{2\omega} \cong \Delta\tilde{z}^{2\omega} \end{gathered} \tag{4.10}$$

In the above predictions we have ignored any chromatic aberration of the lens. This analysis can be generalized (D. G. Papazoglou, personal communication) for generation ring Airy harmonics of any even or odd order. For the case of even orders $Ai(\rho)^{2m}, (m = 1, 2, \dots)$ eq. 4.3 is generalized to:

$$Ai(\rho)^{2m} \cong Ai_2^{\alpha}(\rho)^m = \sum_{n=0}^{m} \frac{2^n \cdot m!}{n!(m-n)!} E(\rho)^{m+n} Ai(\hat{S} \cdot \rho)^{m-n} \tag{4.11}$$

For the case of odd orders $Ai(\rho)^{2m+1}, (m = 1, 2, \dots)$ eq.4.3 is generalized to:

$$Ai(\rho)^{2m+1} \cong Ai_2^{\alpha}(\rho)^m \cdot Ai(\rho) = \sum_{n=0}^{m} \frac{2^n \cdot m!}{n!(m-n)!} E(\rho)^{m+n} Ai(\hat{S} \cdot \rho)^{m-n} \cdot Ai(\rho) \tag{4.12}$$

As an example if we apply these results to the 3rd and 4th harmonic we get:

$$Ai(\rho)^3 \cong 2E(\rho)^2 Ai(\rho) + E(\rho) Ai(\rho) Ai(\hat{S} \cdot \rho), \tag{4.13}$$

$$Ai(\rho)^4 \cong [4E(s)^4 + 2E(s)^2 E(\hat{S} \cdot s)^2] + 4E(\rho)^3 Ai(\hat{S} \cdot \rho) + E(\rho)^2 E(\hat{S} \cdot \rho) Ai(\hat{S} \cdot \rho), \tag{4.14}$$

where $\hat{S} \cdot \rho \equiv 2^{2m/3}\rho + \frac{\pi}{8 \cdot 2^{1/3}} \frac{1 - 2^{2m/3}}{1 - 2^{2/3}}$. Clearly in both cases we can distinguish ring Airy terms that will exhibit abrupt autofocusing as they propagate. In the case of the 4th harmonic the situation is similar to the 2nd harmonic since it can be decomposed to a smooth pedestal and two ring Airy's

4.2.2 Experimental verification

The experimental setup used for the generation of the SH is shown in Fig. 4.4. A Ti:Sapphire laser system was used to deliver Gaussian shaped 800 nm, 35 fs pulses at 50 Hz repetition

rate. The ring-Airy beam was generated using a Fourier transform approach [2]in which the phase of the Gaussian laser beam is phase modulated using a spatial light modulator (SLM, Hamamatsu LCOS-X10468-2) and then is Fourier transformed by a lens. The ring-Airy beam was generated on the Fourier transform plane (FP) of the lens after the zero-order diffraction

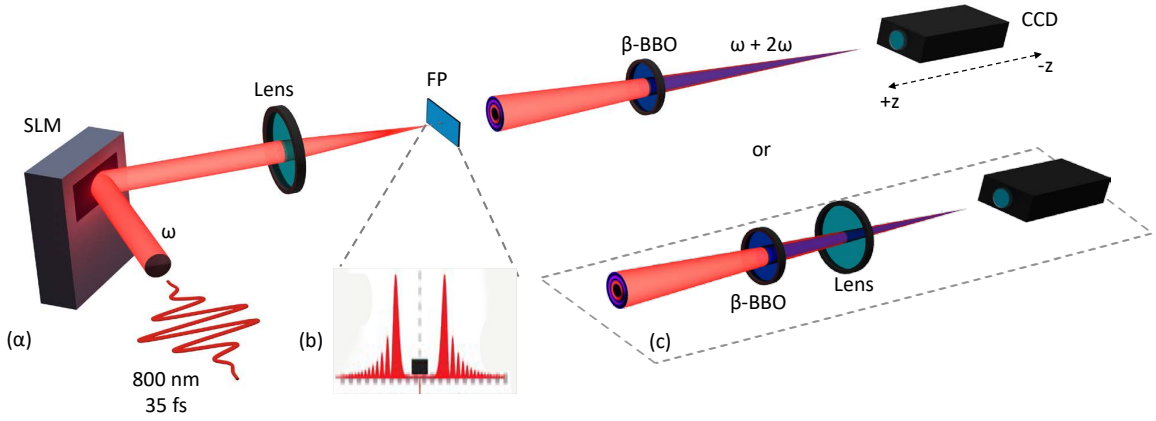

Fig. 4.4 Schematic representation of the experimental setup. The ring Airy beam is generated at the Furrier plane (FP) of a convex lens after it is passed through a spatial light modulator (SLM). A beta-BBO generates the second harmonic and together they either auto focus (a) or extra focused (c) on a scanned CCD. Zero-order diffraction is blocked at the FP (b).

is blocked while its parameters (radius, width) have been tuned in order for the abrupt auto focus to occur at f_{Ai} = 400 mm from the generation plane. The auto focusing beam was then passed through a beta-barium borate (BBO) crystal of 200 um thickness, in order for the second harmonic to be generated while the crystal was properly tuned in order to have the maximum conversion efficiency. The fundamental and its second harmonic were then allowed either to freely auto focus or they were extra focused with the use of a plano-convex focusing lens (f = 100 mm). The distance of the BBO crystal and the focusing lens from the FP was 60 mm and 146 mm respectively. A bandpass interference filter was used in order to allow either the fundamental or its second harmonic to be studied. The transverse intensity distribution of the beam was then imaged by a linear 14-bit CCD camera which was moved along the z propagation.

Firstly, the auto focusing characteristics of the fundamental and its second harmonic were studied without the presence of a focusing lens. Combining 2D transverse (x, y) images that were captured at various positions along the propagation z-axis, the $I(x,y,z)$ intensity profile of the beam was retrieved. An x-z cross section of such a profile is shown in Fig. 4.5 for the above case. Fig.4.5 (a), reveals the auto focusing behavior of the fundamental ring-Airy beam which focuses at z = 400 mm as expected. The characteristic peak followed by evanescent oscillations are prominent. Interestingly enough, as seen in Fig. 4.5 (b), the

second harmonic beam exhibits the same parabolic trajectory to the same focus resulting in an elongated distribution along z, while the characteristic rings at the defocusing region enhances its ring-Airy id. In addition to this, the slowly diffracting pedestal part of the beam is also prominent around the auto focusing part. In fact, this part carries most of the energy since only a part of the fundamental beam keeps its autofocusing character. The same parabolic behavior of the two harmonics results in their spatial overlap at the focus region as expected from the analysis above. This behavior, exposes interesting possibilities in wave mixing experiments such as higher-harmonics generation or even THz generation as will be described later. In Fig. 4.5 (c),(d) are shown the corresponding numerical simulations that verify completely our experimental observations.

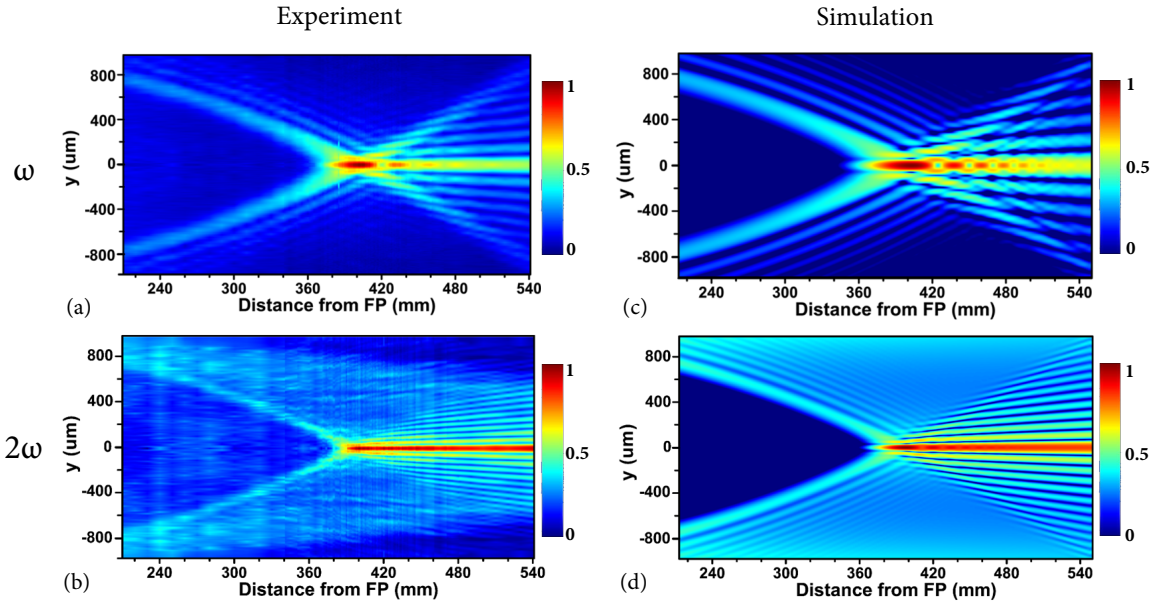

Fig. 4.5 Free propagating fundamental and second harmonic ring Airy beams (a),(b) together with their numerical simulations (c),(d).

The extra focusing lens after the BBO crystal, results in a more peculiar behavior already described in detail in [18]. Briefly, Papazoglou et.al include ring-Airy waves in the family of Janus waves. Thus they can be described as conjugated waves whose propagation can be decomposed to the propagation of twin waves (a “real” and a “virtual” one), which are conjugate to each other under inversion of the propagation distance. Without a focusing lens, the “virtual” wave is diffracting out without any interference with the “real” one. On the other hand, in the presence of a focusing lens both waves are brought to focus resulting in two symmetrical focal distributions. Under certain conditions, these two distributions can be separated in space while the exact position of each, can be precisely calculated and predicted. In Fig.4.6 (a) is shown how the fundamental beam is focused under the specific

focusing conditions. The two foci are clearly present giving rise to a representative intensity pattern observed in [18]. The position of the first and second focus is $z_1^{\omega} = 67.1mm$ and $z_2^{\omega} = 116.6mm$ respectively. In Fig.4.6 (c) the predicted intensity pattern is shown, where one can see that the predicted values for the position of the two foci are in an a very good agreement. In the case of the second harmonic ring-Airy beam, the expected behavior is

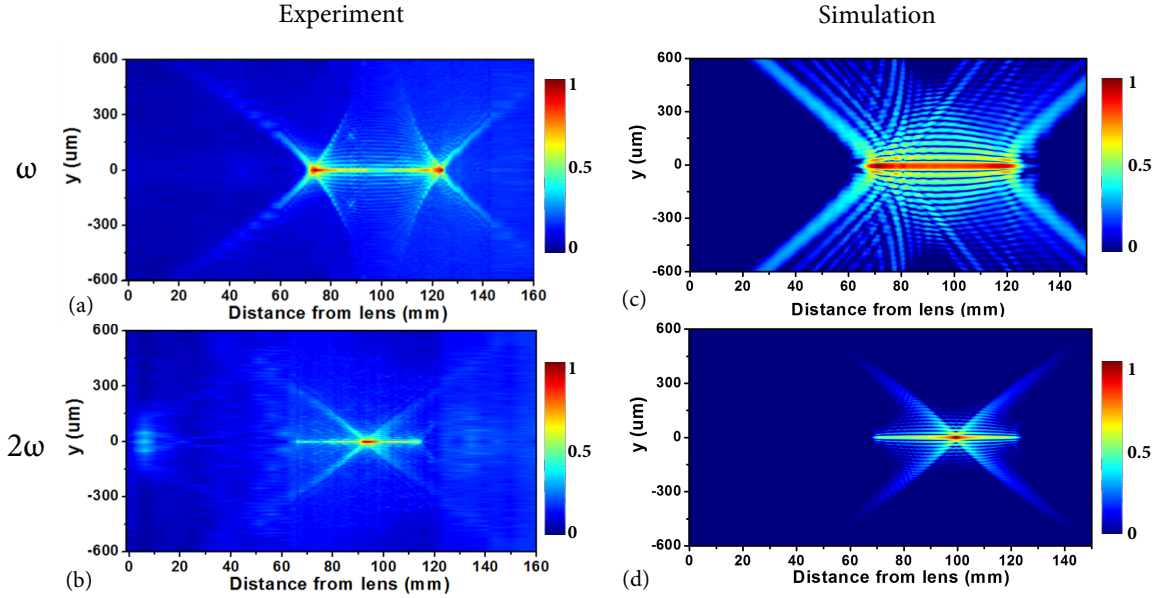

Fig. 4.6 Focused by a thin-lens of fundamental and second harmonic ring Airy beams (a),(b) together with their numerical simulations (c),(d).

almost identical with the fundamental one but the previously observed slowly diverging part of the beam, now is also focused by the lens resulting in an intensity pattern with three foci as can be seen in Fig.4.6 (b). The central focus at $z_3^{2\omega} = 86.6mm$ is more prominent and comes from this diverging part which linearly focuses to the geometrical focus of the lens. The other two foci are found around the central one and although they are fainter their positions $z_1^{2\omega} = 60.13mm$ and $z_2^{2\omega} = 108.2mm$ are clearly in agreement with the predicted values.

Again, what is interesting is the spatial overlap of the two beams. Although the foci of ω and 2ω are not at the exact same position, due to their elongated nature their frequency mixing becomes possible. Next, we will use this special behavior, in order to take advantage of the above observations and study efficient THz emission through two color filamentation using abruptly auto focusing ring-Airy beams, where, as already mentioned in previous chapters, spatial overlapping of the fundamental and its second harmonic is crucial.

4.3 Enhanced THz wave emission from air-plasma tailored by AAF laser beams

As was described above, there is wide range of possible applications when using AAF beams. The nonlinear propagation of novel beams other than Gaussian is always an area of interest for filamentation researchers [8, 19, 20]. The use of these beams not only helps design the spatial profile of the plasma, but also enables various broadband radiations from the plasma, such as supercontinuum radiation [21] terahertz (THz) radiation [22], giving hope to multiple remote-spectroscopy applications [23]. For the AAF beams, the nonlinear propagations were already observed in fused silica [17], but experimental results in air have yet to be demonstrated.

Moreover, we highlighted that a two color scheme using ring-Airy beams results in spatial overlap of the two frequencies in a long plasma channel. Below, we will take advantage of this property and we will investigate the characteristics of THz radiation from two-color AAF-beam-induced air-plasma. Using different plasma parameters to improve generation efficiency is a new area of interest for numerous research groups [24, 25]. Among those efforts, some have tried tailoring the plasma in different ways, such as creating plasma with gradient distribution [26], concatenating two plasmas into one [27], and putting two filaments side by side [28]. They have found that, with those methods, they can achieve either enhancement or control of the THz radiation from the tailored two-color air-plasmas.

AAF beams' high level of tenability [5], wavepacket stability in the nonlinear regime [17], and robustness when propagating in turbulent media [29] make plasmas induced by these novel wavepackets a promising broadband THz source for THz remote sensing and spectroscopy [23, 30], a critical topic for homeland security and environmental monitoring. The AAF beams used in this work were pre-engineered to have the same autofocusing curve as the familiar parabolic trajectory of ring-Airy beams [5].

4.3.1 Experimental setup

The measurements exploited a pump–probe THz time-resolved detection system, shown in Fig.4.7(a). The AAF beams were generated by sending 35 fs, 50 Hz, 800 nm Ti:sapphire laser pulses to a spatial light modulator (SLM, Hamamatsu LCOS-X10468-2), with a phase mask exerted. Following an approach similar to that of Chremmos et al. [5], the phase mask consisted of a radially chirped phase distribution $\phi(r) = C,\ (r - r_0)^{\frac{3}{2}},\ \forall r \geq r_0$ and $\phi(r) = 0,\ \forall r < r_0$, where r is the radius, r_o is a reference radius, and C is a constant. By

blocking the central part of the phase-modulated Gaussian beam with an opaque disk, after some free propagation, a ring-Airy distribution was formed [5]. This method is energetically advantageous com-pared to a Fourier transform approach [4], since the loss of a large amount of energy in the zero-order was avoided. The Gaussian beams were generated by sending the same laser pulses to the SLM with a plain phase mask. When using the Gaussian beam, the opaque disk was removed from the beam path, as shown in the zoom-in parts of Fig. 1(a).

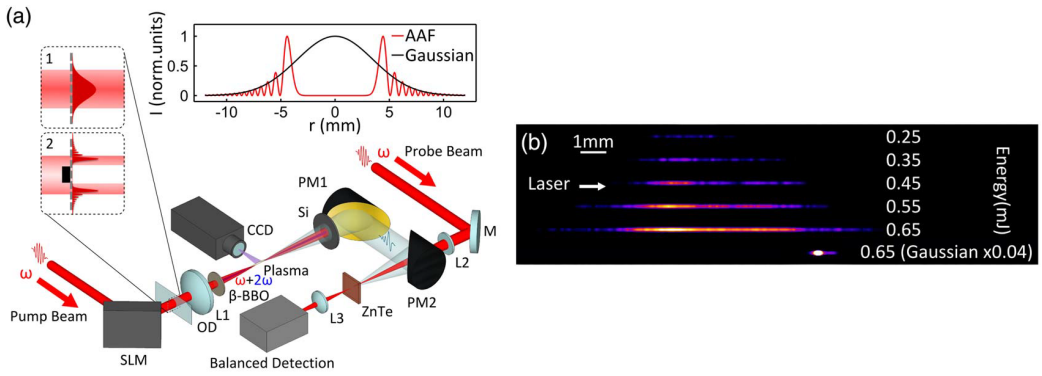

Fig. 4.7 (a) Experimental setup: SLM, spatial light modulator; OD, opaque disk, onto a transparent glass slide; L, lens; PM, parabolic mirror; M, mirror. Inset, top right: schematic comparison between the radial in-tensity distribution of the AAF and the Gaussian beam. Inset, top left: zoom-in on the beam area before and after the glass slide. Case 1 uses the Gaussian beam; the glass slide is shifted so the OD is removed from the beam path. Case 2 uses the AAF beam; the OD is moved back into the center of the beam to block the unwanted part. (b) Fluorescence false color images of AAF beam plasmas (top 5) with pulse energy from 0.25 to 0.65 mJ, and Gaussian beam plasma (bottom) with pulse energy 0.65 mJ. The Gaussian plasma image intensity has been reduced 25 times to reach similar visibility of the AAF beam plasmas.

The experimental setup was designed to compare the THz radiation from air-plasmas induced by AAF beams and Gaussian beams. To increase the intensity enough to generate plasma in air and to precisely position the plasma, in both cases the pump beam was focused by a 100 mm focal length lens, as shown in Fig. 1(a). The focused AAF pump beam preserves the AAF properties, such as the abrupt focusing, except that now the focus is more intense and is shifted toward the laser source. A 50-μm-thick β-barium borate (BBO) was put between the lens and the plasma to create the second-harmonic (SH) generation of the pump pulse. The SH of the AAF beam retains its abrupt autofocusing characteristic, sharing the same acceleration as the fundamental harmonic (FH) [31] and as mentioned before the abrupt autofocusing foci of the fundamental AAF and its SH overlap in space. The pulse energy of the pump beam before the β-BBO ranged from 0.1 to 0.65 mJ. The maximum energy that could be applied was limited by the onset of white-light generation in the lens that would cause damage.

Free-space electro-optic sampling with a 3-mm-thick <110> cut ZnTe was used to detect THz waveforms [32]. A pair of off-axis-parabolic-mirrors was used to collect, collimate, and re-focus the forward THz radiation from the plasma. Fluorescence images of the generated plasmas were recorded using a linear CCD camera and imaging optics.

4.3.2 Results

The fluorescence distribution emission $F(r,z)$ for various in-put optical energies is shown in Fig.4.7(b). In the figure, from top to bottom, the plasma images are respectively formed by focusing AAF beams with 0.25, 0.35, 0.45, 0.55, and 0.65 mJ pulse energy. It is clearly observed that the peak intensity of the plasma string shifts as the input energy increases.

Also observable is the emergence of low-intensity secondary peaks following the primary focus, as a characteristic feature of ring-Airy beams. At high en-ergy, the secondary peaks are merged with the main peak to a single plasma string. These nonlinear propagation phenomena in air agree very well with the nonlinear propagation of ring-Airy beams in the bulk of fused silica reported in 2013 by Panagiotopoulos et al. [17]. When we compare the plasmas induced by AAF and Gaussian beams [bottom trace in Fig.4.7(b)], we notice that the AAF beam induced plasma is significantly longer in contrast to the Gaussian plasma. Not only the length difference is apparent, but the difference in fluorescence emission intensity is also obvious. For example, with 0.65 mJ pump pulse energy, the maximum recorded fluorescence intensity of the Gaussian plasma is 210 times brighter than that of plasma generated by the AAF beam.

Fig.4.8(a) and (b) show the THz waveform and its spectrum generated by an AAF-beam-induced plasma. The signal was optimized through tuning the relative phase and intensity proportion between the FH (800 nm) and the SH (400 nm) by adjusting the position and angle of the β-BBO crystal. The spectral bandwidth of the detected THz signal is essentially limited by the phonon absorption of the ZnTe crystal.

Because the AAF air-plasma THz source under study shares the same asymmetrical laser field and interaction material with the familiar Gaussian air-plasma THz source, a THz emission process similar to that of a Gaussian source is expected. To confirm this expectation, we measured the THz peak amplitude as a function of the relative phase between the two colors by scanning the β-BBO between the focus and the lens. The scanning range of the crystal was limited by the focal length of the lens and the damage threshold of the BBO. The results are shown in Fig.4.8(c). The THz yield modulation is due to the variation of the relative phase between the two colors. The insets give examples of how the relative phase controls the THz radiation waveform polarity. Also shown in Fig.4.8(c) is that these data can be fitted using the four-wave-mixing (FWM) model [33] while taking into account how the

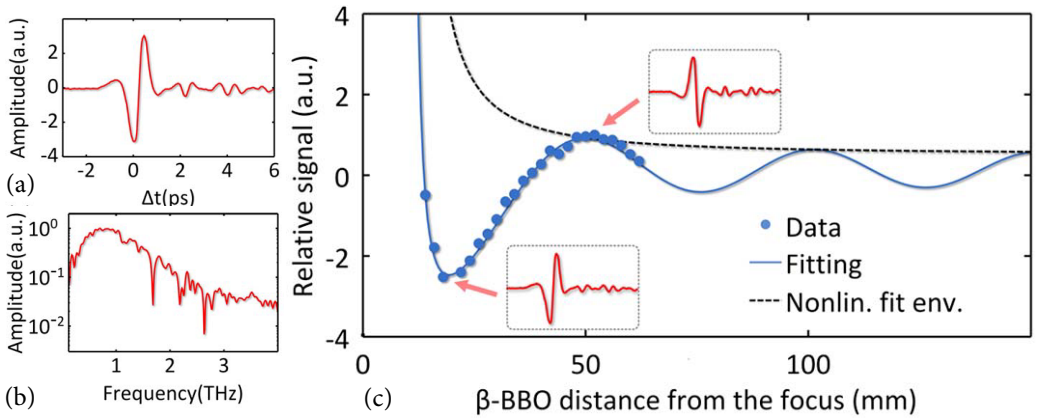

Fig. 4.8 (a) Typical THz waveform generated from the AAF-beam-induced plasma pumped with a pulse energy of 0.65 mJ. (b) The corresponding spectrum. (c) THz emission peak amplitude versus the β-BBO distance from the focus: blue dots, experimental data; blue solid curve, FWM model fitting result; black dashed curve, nonlinear fitting envelope taking into account the SH generation efficiency change as the β-BBO is moving toward the focus. The insets show two sample THz waveforms having opposite polarities.

SH generation efficiency would change as the β-BBO crystal moves closer to the plasma due to the beam intensity change on the crystal. The resulting fitting parameters give a THz yield modulation oscillation period that is consistent with the known dispersion in air [34].

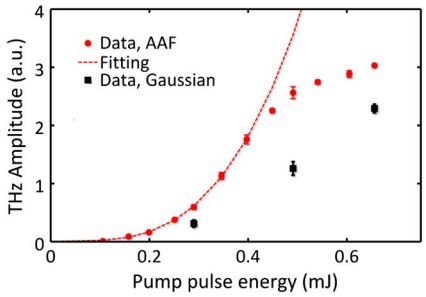

Fig. 4.9 Emitted THz wave peak amplitude as a function of total pump pulse energy (800 and 400 nm). Red dots, experimental data from the AAF beam; red dashed line, fitting of the AAF data with the FWM model; black squares, data from Gaussian beam under the same initial conditions as a comparison. The error bars show the measurement standard deviation of each point.

Fig.4.9 shows the emitted THz amplitude as a function of the input pulse energy. The red dots are the experimental data from the AAF beam plasma, which can be fitted with the FWM model: $E_{THz} \propto \alpha\chi^{(3)}I(I-bI^2)$ [33] where E_{THz} is the emitted THz field amplitude, α and b are constants, I is the total beam intensity before the BBO crystal, and $\chi^{(3)}$ is the third-order susceptibility of air. The fitting result shows that the experimental data starts to deviate from the fitting curve at around 0.45 mJ and the deviation becomes prominent at 0.55

mJ. This implies that, for higher pulse energies, one should consider the photocurrent model and the intensity clamping in the filaments [35, 36]. There could also be contribution from the nonlinear interaction between the beam and the lens that can cost some of the energy. When the input pulse energy is high, some energy hot spots observed on the primary ring of the AAF beam tend to cause white-light generation from the lens. To better characterize the AAF beam plasma as a THz source, we compare its THz emission with the one from a Gaussian-beam-induced plasma under the same experimental conditions.

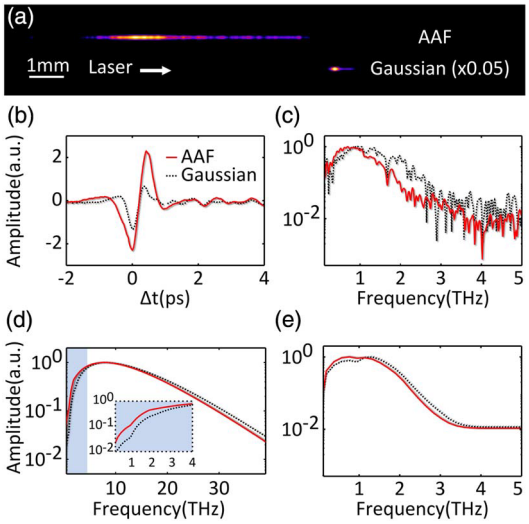

Fig. 4.10 (a) Fluorescence image comparison between an AAF beam plasma and a Gaussian plasma (intensity reduced by 20 times), both generated with pump pulse energy of 0.5 mJ. (b) Measured THz waveforms and (c) their corresponding normalized spectra generated by the two plasmas in (a). Normalized simulations of THz radiation spectra (d) without and (e) with the 3-mm-thick ZnTe detection bandwidth limitation; the inset in (d) is the enlarged version of the blue area (0–4 THz). Red solid curves, emission from AAF plasma; black dashed curves, emission from Gaussian plasma.

Fig.4.10(a) shows the images of the plasmas being discussed below. With a 0.5 mJ input pulse energy, the AAF beam plasma THz waveform measured is shown in Fig.4.10(b), whereas the one from the Gaussian beam has noticeably lower amplitude. If we calculate the pulse energy by integrating the square of THz field, the THz pulse energy from the AAF plasma is about 5.3 times larger than that from the Gaussian plasma. The obvious THz yield difference can be explained by the significant plasma length difference [37], as we have qualitatively verified with our interference model [38]. Neither plasma has reached the typical air filamentation dephasing length. If we consider the possibility that a shorter plasma may emit THz with a larger angle [38], which means the THz radiation from the Gaussian beam plasma could eventually be focused tighter than that from the AAF plasma, the real THz yield difference between the two might be substantially bigger than what we measured.

Fig.4.10(c) shows the normalized spectra of the waveforms. The AAF plasma THz emission has a central frequency slightly lower than the Gaussian one, which denotes that the AAF plasma has a lower plasma density [34]. A set of power-dependence measurement data of Gaussian beams is also shown in Fig.4.9.

During the experiment, the lens location was optimized for each measurement to avoid the signal discrepancy caused by focus location changes. Moreover, a 2-in. (50.8 mm) diameter parabolic mirror with 3-in. (76.2 mm) focal length was put after the plasma to collect the THz radiation, providing an 18.4° collecting angle, sufficient to cover the emission cone ($\sim 10^o$) from a two-color air-plasma generated by the 100 mm focal length lens [39].

To validate our hypothesis on the reasons behind the enhanced THz radiation pulse energy of AAF-beam-induced plasma and its redshifted central frequency, we performed simulations using our interference model described in Chapter 2, which is able to depict the THz radiation intensity and spectrum of a known plasma [38]. Using the plasma distributions according to the fluorescence images and the numerical estimations of the maximum electron densities for the Gaussian beam ($\sim 10^{17} cm^{-3}$) and the AAF beam ($3 \times 10^{16} cm^{-3}$), taking into account the detection bandwidth limitation of a 3-mm-thick ZnTe crystal, the resulting simulated THz radiation pulse energy of an AAF-beam-induced plasma is found to be about 4 times larger than that from the Gaussian plasma source. The normalized calculations of THz radiation spectra from these two THz sources are shown in Fig.4.10(e), giving the same type of central frequency difference as experimental measurements display. Both simulation results agree qualitatively well with the measured data. In addition, to predict the THz sources' behavior when using a broadband detection method, such as THz-air-biased-coherent-detection [40] or interferometric detection [34], we also performed a full spectral simulation without the bandwidth limit ZnTe, which indicates that the in-tensity enhancement and the redshift of the AAF-beam-induced THz radiation would persist regardless of the detection method. Fig.4.10(d), which shows the normalized full spectrum results with an inset focusing on the low-frequency region, helps to reveal that the AAF-beam-induced THz radiation spectrum would still have a redshift as compared to the Gaussian one. This spectral shift to the low frequency could possibly benefit the THz radiation enhancement of AAF-beam-induced plasma that we measured in the low-frequency region. Even so, considering that 0.1–3 THz is the most commonly used and more advantageous frequency range for THz time-domain spectroscopy [41], the enhancement we achieved through using AAF beam is still exciting.

4.4 Conclusion

In this chapter we utilized the use of AAF beams and particularly of ring-Airy beams to generate enhanced THz radiation from their laser-induced air-plasma through two color scheme. In order to achieve this, a study of fundamental and second harmonic generation and propagation properties were first studied. We showed that, FH and SH beams auto focus at the exact same position in the absence of an extra focusing lens while in its presence they focus in more peculiar way exhibiting a double focus, but again in the same positions. FH and SH are spatially overlapping in an elongated region opening new possibilities on generation of higher harmonics and of course THz generation when the power is enough to generate plasma in air. For the higher harmonics we investigate theoreticaly the case of 3rd and 4th harmonics were we can see that they will exhibit abrupt autofocusing.

Conserning THz generation, we performed experiments in air using AAF beams in comparison to normal Gaussian beams. We observed that, under the same experimental conditions with 0.5 mJ input pulse energy, the AAF-plasma-generated THz pulse energy is about 5.3 times larger than that from the Gaussian beam, possibly due to the significant plasma length difference. There is a noticeable change in the THz radiation spectrum between the AAF beam and the Gaussian beam that could be attributed to the plasma density difference between the corresponding plasmas. This unique wavepacket-based THz emitter demonstrates the possibility of AAF beam application in THz frequency remote sensing that will enable a high level of control on the excitation beam. It sets a reference for future work involving using different novel wavepackets to tailor the plasma as a THz source. Systematic exploration of the optimum AAF beam parameters for THz generation will possibly entail a further enhancement of THz radiation. Other families of beams may also exhibit interesting physics in regard to THz generation, such as 2D Airy beams [19] or Airy–Airy–Airy light bullets [9]. As more types of novel beam have been reported, using tools like SLMs or phase masks to sculpt the excitation beams could be a new direction for controlling THz radiation from laser-induced plasma.

References

[1] Bahaa E A Saleh and Malvin Carl Teich. Fundamentals of Photonics , 2nd Edition, 2007.

[2] Nikolaos K. Efremidis and Demetrios N. Christodoulides. Abruptly autofocusing waves. *Optics Letters*, 35(23):4045–4047, 2010.

[3] G A Siviloglou, J Broky, A Dogariu, and D N Christodoulides. Observation of Accelerating Airy Beams. *Physical Review Letters*, 99(21):213901, 2007.

[4] Dimitrios G Papazoglou, Nikolaos K Efremidis, Demetrios N Christodoulides, and Stelios Tzortzakis. Observation of abruptly autofocusing waves. *Optics letters*, 36(10):1842–4, may 2011.

[5] Ioannis Chremmos, Nikolaos K Efremidis, and Demetrios N Christodoulides. Pre-engineered abruptly autofocusing beams. *Optics letters*, 36(10):1890–1892, 2011.

[6] Peng Zhang, Jai Prakash, Ze Zhang, Matthew S Mills, Nikolaos K Efremidis, Demetrios N Christodoulides, and Zhigang Chen. Trapping and guiding microparticles with morphing autofocusing Airy beams. *Optics letters*, 36(15):2883–2885, 2011.

[7] Ioannis Chremmos. Temporal cloaking with accelerating wave packets. *Optics letters*, 39(15):4611–4, 2014.

[8] Pavel Polynkin, Miroslav Kolesik, Adam Roberts, Daniele Faccio, Paolo Di Trapani, and Jerome Moloney. Generation of extended plasma channels in air using femtosecond Bessel beams. *Optics express*, 16(20):15733–15740, 2008.

[9] Daryoush Abdollahpour, Sergiy Suntsov, Dimitrios G. Papazoglou, and Stelios Tzortzakis. Spatiotemporal Airy Light Bullets in the Linear and Nonlinear Regimes. *Physical Review Letters*, 105(25):253901, dec 2010.

[10] Jeffrey a. Davis, Don M. Cottrell, Juan Campos, María J. Yzuel, and Ignacio Moreno. Encoding Amplitude Information onto Phase-Only Filters. *Applied Optics*, 38(23):5004–5013, 1999.

[11] T. Ellenbogen, N. Voloch, a. Ganany-Padowicz, and a. Arie. Nonlinear generation and manipulation of Airy beams. *2009 Conference on Lasers and Electro-Optics and 2009 Conference on Quantum electronics and Laser Science Conference*, 3(June):395–398, 2009.

[12] Ido Dolev, Tal Ellenbogen, Noa Voloch-Bloch, and Ady Arie. Control of free space propagation of Airy beams generated by quadratic nonlinear photonic crystals. *Applied Physics Letters*, 95:2–4, 2009.

[13] Ido Dolev and Ady Arie. Three wave mixing of airy beams in a quadratic nonlinear photonic crystals. *Applied Physics Letters*, 97:1–3, 2010.

[14] Shu Jia, Joyce Lee, Jason W. Fleischer, Georgios A. Siviloglou, and Demetrios N. Christodoulides. Diffusion-trapped airy beams in photorefractive media. *Physical Review Letters*, 104(25):1–4, 2010.

[15] Yi Hu, Simon Huang, Peng Zhang, Cibo Lou, Jingjun Xu, and Zhigang Chen. Persistence and breakdown of Airy beams driven by an initial nonlinearity. *Optics Letters*, 35(23):3952–3954, 2010.

[16] Ido Dolev, Ido Kaminer, Asia Shapira, Mordechai Segev, and Ady Arie. Experimental observation of self-accelerating beams in quadratic nonlinear media. *Physical Review Letters*, 108(March):1–5, 2012.

[17] P Panagiotopoulos, D G Papazoglou, A Couairon, and S Tzortzakis. Sharply autofocused ring-Airy beams transforming into non-linear intense light bullets. *Nat Commun*, 4, 2013.

[18] Dimitris G. Papazoglou, Vladimir Yu. Fedorov, and Stelios Tzortzakis. Janus waves. *Optics Letters*, 41(20):4656, oct 2016.

[19] Pavel Polynkin, Miroslav Kolesik, Jerome V Moloney, Georgios a Siviloglou, and Demetrios N Christodoulides. Curved plasma channel generation using ultraintense Airy beams. *Science (New York, N.Y.)*, 324(5924):229–232, 2009.

[20] Maik Scheller, Matthew S. Mills, Mohammad-Ali Miri, Weibo Cheng, Jerome V. Moloney, Miroslav Kolesik, Pavel Polynkin, and Demetrios N. Christodoulides. Externally refuelled optical filaments. *Nature Photonics*, 8(4):297–301, 2014.

[21] Pavel Polynkin, Miroslav Kolesik, and Jerome Moloney. Filamentation of Femtosecond Laser Airy Beams in Water. *Physical Review Letters*, 103(12):123902, sep 2009.

[22] S. Moradi, A. Ganjovi, F. Shojaei, and M. Saeed. Parametric study of broadband terahertz radiation generation based on interaction of two-color ultra-short laser pulses. *Physics of Plasmas*, 22(4), 2015.

[23] Jingle Liu, Jianming Dai, See Leang Chin, and X.-C. Zhang. Broadband terahertz wave remote sensing using coherent manipulation of fluorescence from asymmetrically ionized gases. *Nature Photonics*, 4(9):627–631, sep 2010.

[24] Xu Xie, Jianming M Dai, and X.-C. C Zhang. Coherent control of THz wave generation in ambient air. *Physical Review Letters*, 96(7):075005, feb 2006.

[25] Eiichi Matsubara, Masaya Nagai, and Masaaki Ashida. Ultrabroadband coherent electric field from far infrared to 200 THz using air plasma induced by 10 fs pulses. *Applied Physics Letters*, 101(1):011105, 2012.

[26] J M Manceau, A Averchi, F Bonaretti, D Faccio, P Di Trapani, A Couairon, and S Tzortzakis. Terahertz pulse emission optimization from tailored femtosecond laser pulse filamentation in air. *Optics Letters*, 34(14):2165–2167, 2009.

[27] J-M Manceau, M Massaouti, and S Tzortzakis. Strong terahertz emission enhancement via femtosecond laser filament concatenation in air. *Optics letters*, 35(14):2424–6, jul 2010.

[28] Jiayu Zhao, Lanjun Guo, Wei Chu, Bin Zeng, Hui Gao, Ya Cheng, and Weiwei Liu. Simple method to enhance terahertz radiation from femtosecond laser filament array with a step phase plate. *Optics Letters*, 40(16):3838, 2015.

[29] Xiuxiang Chu. Evolution of an Airy beam in turbulence. *Optics letters*, 36(14):2701–3, 2011.

[30] Dai Jianming, Liu Jingle, and Zhang Xi-Cheng. Terahertz Wave Air Photonics: Terahertz Wave Generation and Detection With Laser-Induced Gas Plasma. *Selected Topics in Quantum Electronics, IEEE Journal of*, 17(1):183–190, 2011.

[31] Ido Dolev, Ido Kaminer, Asia Shapira, Mordechai Segev, and Ady Arie. Experimental observation of self-accelerating beams in quadratic nonlinear media. *Physical Review Letters*, 108(11):1–5, 2012.

[32] Q Wu and X C Zhang. Ultrafast electro-optic field sensors. *Applied Physics Letters*, 68(12):1604–1606, 1996.

[33] Jianming Dai and X C Zhang. Terahertz wave generation from thin metal films excited by asymmetrical optical fields. *Optics Letters*, 39(4):777–780, 2014.

[34] K. Y. Kim, A. J. Taylor, J. H. Glownia, and G. Rodriguez. Coherent control of terahertz supercontinuum generation in ultrafast laser–gas interactions. *Nature Photonics*, 2(10):605–609, jul 2008.

[35] M D Thomson, M Kress, T Loffler, and H G Roskos. Broadband THz emission from gas plasmas induced by femtosecond optical pulses: From fundamentals to applications. *Laser & Photonics Reviews*, 1(4):349–368, 2007.

[36] T I Oh, Y S You, N Jhajj, E W Rosenthal, H M Milchberg, and K Y Kim. Scaling and saturation of high-power terahertz radiation generation in two-color laser filamentation Scaling and saturation of high-power terahertz radiation generation in two-color laser filamentation. *Appl. Phys. Lett.*, 102:201113, 2013.

[37] Y. S. You, T. I. Oh, and K. Y. Kim. Off-Axis Phase-Matched Terahertz Emission from Two-Color Laser-Induced Plasma Filaments. *Physical Review Letters*, 109(18):183902, oct 2012.

[38] Andrei Gorodetsky, Anastasios D Koulouklidis, Maria Massaouti, and Stelios Tzortzakis. Physics of the conical broadband terahertz emission from two-color laser-induced plasma filaments. *Physical Review A*, 89(3):33838, 2014.

[39] V. Blank, M. D. Thomson, and H. G. Roskos. Spatio-spectral characteristics of ultrabroadband THz emission from two-colour photoexcited gas plasmas and their impact for nonlinear spectroscopy. *New Journal of Physics*, 15(7):75023, 2013.

[40] Jianming Dai, Jingle Liu, and Xi-Cheng Zhang. Terahertz Wave Air Photonics: Terahertz Wave Generation and Detection With Laser-Induced Gas Plasma. *IEEE Journal of Selected Topics in Quantum Electronics*, 17:183–190, 2011.

[41] Xi-Cheng Zhang and Jingzhou Xu. *Introduction to THz Wave Photonics*, volume 53. Springer US, Boston, MA, 2010.

Chapter 5

Novel approaches for enhancing the THz emission

In Chapter 2 we described in detail some of the most efficient and most commonly used THz generation techniques. All of them had in common the utilization of ultra fast laser pulses in order to generate THz pulses either in solid media through photo-carriers generation in semiconductor antennas and through optical rectification in non-linear crystals or in gases using laser generated plasma channels. Advantages and drawbacks appear in all of them regarding the desirable application. For example, photo-conductive antennas although they generate relatively low power THz pulses, they are ideal for spectroscopic studies where the large bandwidth is not of much interest. They can work even with relatively small pump energies easily available nowadays by laser oscillators working at high repetition rates. This, on one hand increases dramatically the signal to noise ratio of the system while at the same time reduces the total size of the system making it ideal for mobile applications. THz market today is mainly orientated in portable and reliable THz systems for commercial THz spectrometers. Moreover, when intense THz pulses are needed, optical rectification is the best choice, limited though by the narrow bandwidth and the damage threshold of the crystal, when considering further increase in the output. Two-color filamentation on the other hand can supply intense and ultra-broadband THz pulses but amplified femtosecond laser pulses are needed in order to ionize air (or any other gas). Investigating the possibility to develop a technique that could eventually combine the advantages of all the techniques is a challenging topic. In this final part of the thesis, preliminary results will be presented paving the way for THz generation in solid media using the two-color filamentation scheme.

5.1 Enhanced emission of THz pulses in fused silica

The main drawback in two color filamentation in air, is the high ionization threshold. On the other hand in solids this threshold is lower while at the same time linear and non-linear refractive indexes are higher resulting in a smaller P_{cr} and thus in an easier filament formation. For example in fused silica (SiO_2) for 800 nm 6 photons are needed in order to generate an electron while its non-linear refractive index is of the order of $10^{-16} cm^2/W$, three orders of magnitude higher than air. Moreover, fused silica is transparent to THz radiation up to 7 THz making it an excellent candidate for THz generation through two color filamentation. This enables the use of less powerful laser pulses in order to generate a filament inside the SiO_2 material allowing one even to switch to just an oscillator without the need of an amplifier. This could result in a THz source capable to emit broadband THz pulses at high repetitions rates.

The only problem that needs to be resolved, is dephasing between the fundamental and the second harmonic inside the material. In air-plasma the length after which two 35 fs pulses of 800 nm and 400 nm will be completely separated in time, is around 4 meters [1]. On the other hand, in SiO_2 this length is only 200 μm limiting this way the maximum available plasma length. Nevertheless, recently THz emission from laser-induced micro-plasma in air was reported [2]. Buccheri et.al, presented THz pulses generated by a single color micro-plasma of 40 x 40 μm dimensions generated by laser pulse energies as low as 700 nJ. This implies that even smaller in dimensions plasma distribution can emit sufficient THz pulses.

Next we will present the first ever reported results of THz generation though two color filamentation in fused silica. Enhanced THz emission up to 19% is observed under specific conditions when a SiO_2 plate is inserted in front of a plasma distribution in air. A systematic study for various focusing conditions reveals the role of the plasma formation inside the material.

5.1.1 Experimental setup

A Yb:KGW 6 W femtosecond laser system delivering 150 fs pulses at 1032 nm central wavelength. The repetition rate is tunable from single shot to 600 kHz. In this study, the repetition rate was fixed at 1 kHz. The long laser pulses together with the longer wavelength increases the length in which ω and 2ω overlap in time inside fused silica to 1.5 mm. The laser beam was focused by different focal lenses to form a plasma in air after it was passed through a 50 μm thick beta Barium Borate crystal that generated the second harmonic. THz radiation emitted from plasma was collected and guided to the electro-optic sampling detection using off-axis parabolic mirrors. A schematic representation of the experimental

setup can be seen in Fig.5.1. A part of the initial beam was used for the electro-optic sampling scheme and two crystals were utilized, a 1 mm thick ZnTe and a 100 μm thick GaP crystals in order to validate the spectrum of the new generated signal. A 1 mm fused silica plate was inserted after the plasma and was scanned around the propagation direction of the laser beam. In the beginning the plate is far beyond the plasma region and acts only

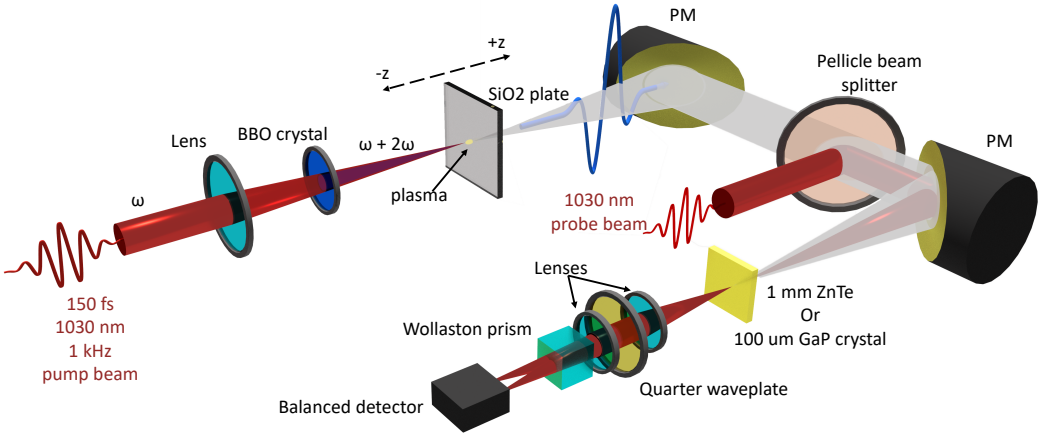

Fig. 5.1 Schematic representation of the setup used. PM: parabolic mirror.

as an absorbing material on the THz radiation. When gradually it is positioned closer to the plasma, an enhancement of the recorded signal is observed reaching a maximum value and then gradually decreases again when reaching the plasma region. At the same time, inside the SiO_2 plate becomes visible a nice filament (not shown here) showing a maximum supercontinuum generation at the peak of the enhancement of the THz signal.

5.1.2 Results

Fig. 5.2 shows the above behavior for three different focusing conditions presenting the THz amplitude normalized to the maximum value that was recorded for each focusing geometry versus the position of the plate around the plasma. The region in the graphs where there is a plateau is when the SiO_2 plate is far beyond the plasma region. One can clearly see, that the focusing geometry strongly affects the enhancement of the THz signal. Stronger focusing leads to higher gain on the THz signal up to 24% for the case of 30 mm lens and while the effect decreases for looser focusing conditions as can be seen in Fig. 5.3 (a). Another interesting observation is that the longer the focusing lens is, the longer the region around the plasma in which the enhancement occurs. At the same time, the phenomenon is energy dependent and this dependence on the laser pulse energy, can be seen in Fig.5.3 (b) for the 50 mm lens. As we can see, as the energy of the input pulse decreases, an extra increase in the enhancement is observed and then gradually decreases.

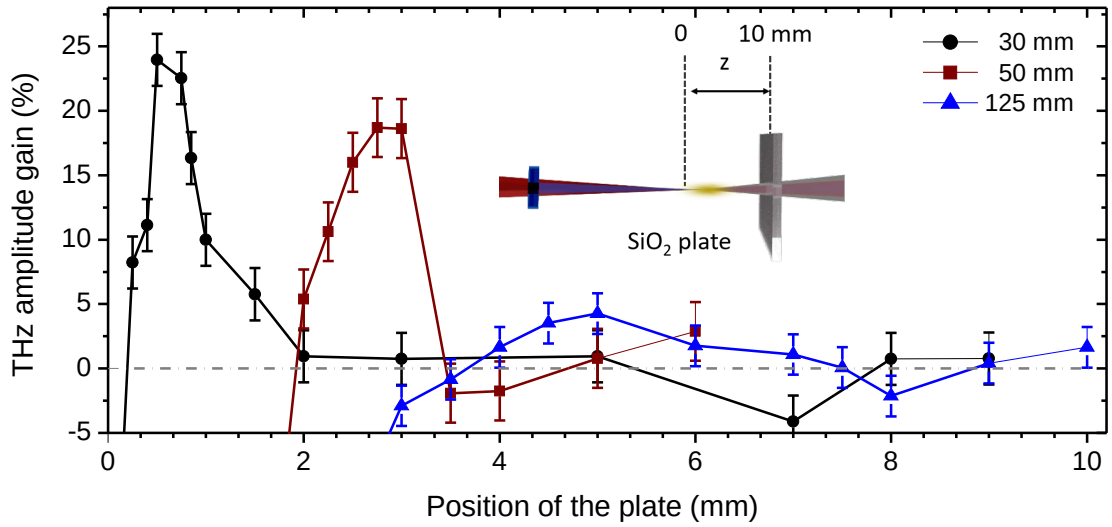

Fig. 5.2 THz amplitude gain versus position of the SiO2 plate around the plasma for three different focal lengths: 30 mm, 50 mm and 125 mm. Insets shows a schematic representation of the way the plate was scanned around the plasma region.

The observed increase in the THz signal, is attributed to the filament formation inside the SiO_2 plate. The extra emission in the signal, is strongly dependent on the beam characteristics exactly after the plasma in air. We believe that the beam is in the appropriate condition at the

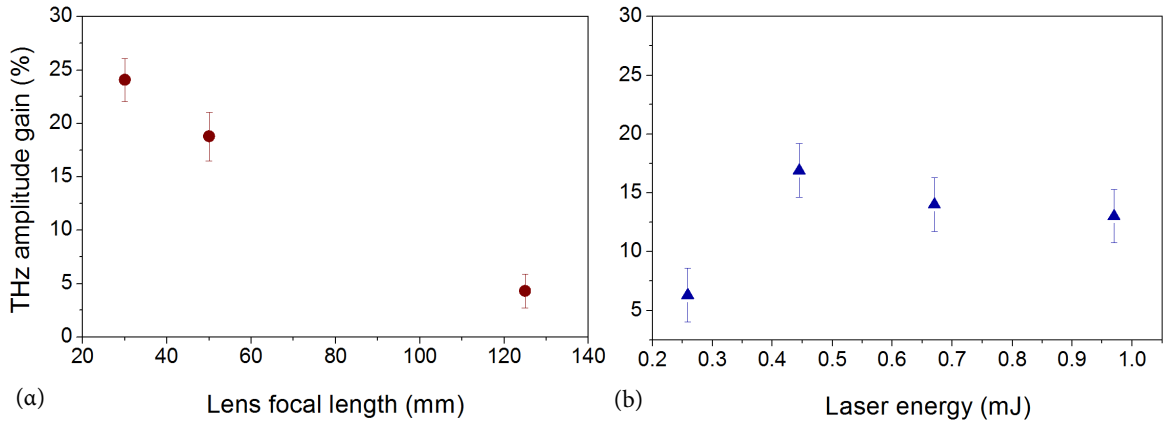

Fig. 5.3 Enhancment of THz signal depending on (a)focal length for a constant laser pulse energy of 1 mJ and (b) on the laser pulse energy for the case of 50 mm lens.

entrance of the SiO_2 plate concerning its size as well as its intensity. This explains why the focusing conditions affect both the length of the region around the plasma distribution that the phenomenon occurs and the laser pulse energy at which the effect becomes more prominent. In order to further validate this hypothesis the plate was moved before the plasma in air (when the position of the plate is close to zero in Fig. 5.2) and the beam is still converging.

Theoretically we could be able to find an optimum position where the size and the intensity of the beam will be the same as the one on the other side of the plasma resulting in a clear signal emerging from the plate. Unfortunately the results were not clear. In Fig.5.2 we can see that even when the plasma is fully within the SiO_2 plate, there is still some signal recorded. Due to the nature of the experiment, THz emission from two color filamentation in air can occur even for the very low plasma density of the plasma before the plate. Thus one cannot easily distinguish whether the emission that is recorded comes from the SiO_2, the air plasma or both. Later we will discuss briefly the way to overcome this problem and isolate only the emission from the filament inside the SiO_2. Our statement about the

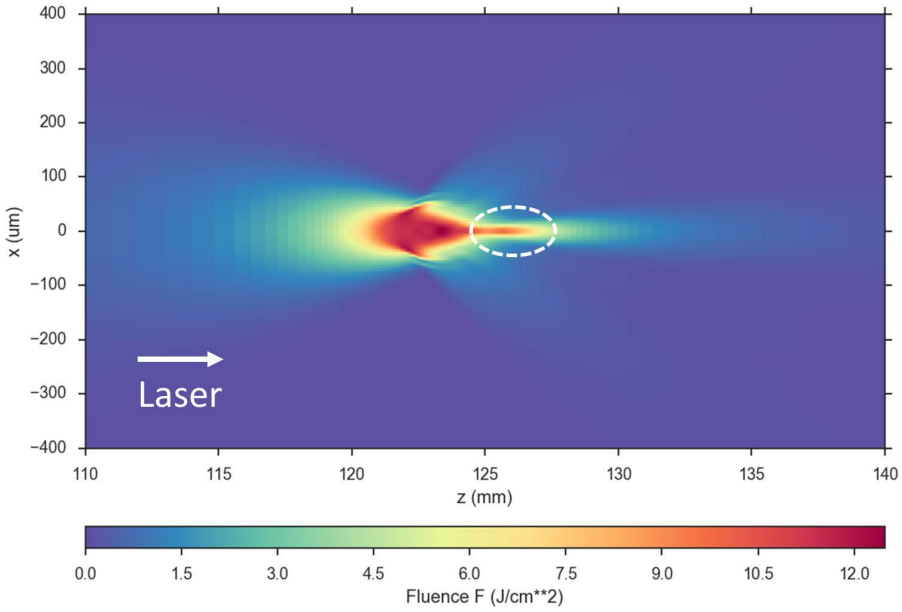

Fig. 5.4 Simulated fluence distribution generated with a 125 mm lens for a laser beam with our initial conditions.

filament formation inside the plate is validated by the numerical simulation shown in Fig.5.4, where the focusing of our laser beam is simulated for the case of the 125 mm lens. As one can see, there is an intense elongated tail after the main plasma. We believe that this tail generates the filament inside the fused silica plate and results in the enhancement of the THz generation. This becomes even more clear if we plot these simulation results together with our experimental data of the 125 mm lens. As we can see in Fig.5.5,the region in which we observe the THz amplitude enhancement overlaps with the intense tail of the plasma in air. For stronger focusing conditions, we expect that this tail will become shorter and more intense resulting in higher plasma density inside the plate and consequently in stronger THz emission as observed in our experiment. At the same time a shorter tail length could also validate our observations on the width of the region over which the enhancement occurs.

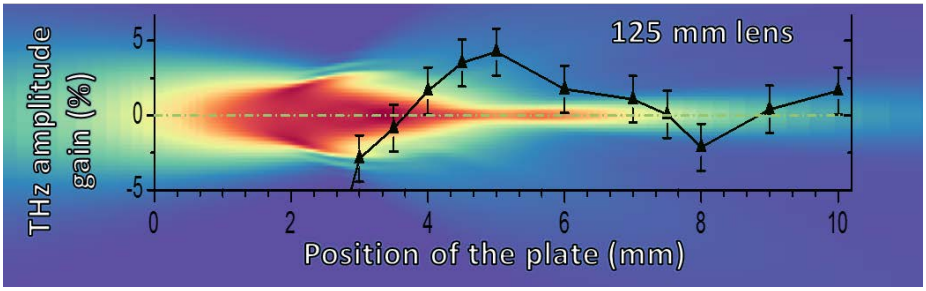

Fig. 5.5 Comparison of simulation results in Fig.5.4 with the experimental data of Fig.5.2 for the 125 mm lens.

Finally, in order to investigate the spectral nature of the THz radiation emitted from the SiO_2 we performed experiments using a GaP crystal that extents the detection bandwidth of our system to 8 THz. As we described in Chapter 3 and since our pulse duration is 150 fs we expect that the emitted radiation from the plasma in air is fully covered by the detection bandwidth of this crystal. This can give us information on whether the extra emitted radiation occurs at higher frequencies or not. In Fig.5.6 (a) can be seen the THz signal along with its corresponding spectrum Fig.5.6 (b) for two different positions of the SiO_2 plate in the case of the 50 mm lens. With black color is shown the signal recorded when the plate is

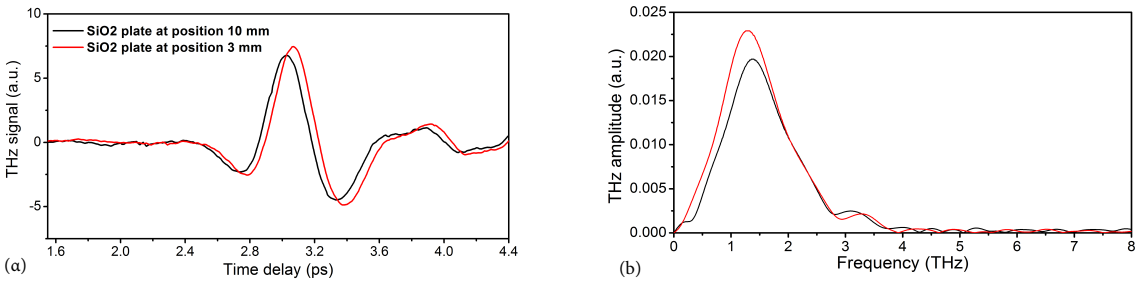

Fig. 5.6 THz electric fields (a) and their corresponding spectra (b) for two different positions of the SiO_2 plate for the case of 50 mm lens.

far from the plasma and with red color the one recorded at the position where we get the maximum enhancement in the signal (points 10 mm and 3 mm respectively in Fig.5.2(b)). We can see, that the SiO_2 signal contributes mainly to the lower part of the spectrum, below 2 THz. Taking into account the two mechanisms of THz generation in two-color filamentation (see Chapter 2) this contribution to the lower frequencies allows us to attribute the emission from SiO_2 at a plasma contribution rather than a FWM process.

5.1.3 Current and future plans

In order to better characterize this new source one should perform the experiment in a slightly different way. As mentioned before there are two different ways to utilize THz generation through two-color filamentation. The first is the in-line scheme where ω and 2ω are co-propagating after the BBO crystal and is the one that we used here, and the other one is when the two frequencies are split and recombined again. The latter one allows one to properly adjust the temporal delay of the two frequencies. Thus enables the possibility to use a much thicker SiO_2 plate and generate the whole filament inside it and then properly adjust the delay in order to compensate the dispersion of the material. This will eliminate any THz signal coming from low density plasma before the focus since the sample can be thick enough to cover that region. We are currently working on this setup along with numerical simulations that will strength our statements above.

Moreover at the same time, we will perform experiments under the same idea using even longer wavelengths in other materials like silicon. Silicon (Si) is a semiconductor and has a huge transparency window in the THz region. Longer wavelengths are ideal for plasma generation inside bulk Si with extremely high plasma densities of the order of $10^{20} cm^{-3}$ using relatively low laser energies. The mid-IR beams will generate a plasma distribution inside the bulk Si and then the field symmetry will have to be broken. As a first step, we will induce this asymmetry by applying an external DC electric field into the Si and in a further step, two-color generation scheme will be introduced by properly choosing the two wavelengths while at the same time the above technique of splitting and recombining the two wavelengths will be used in order to control the temporal overlap of the two pulses inside the filament as well as their polarizations. Ideally this could lead to even broader THz generation than SiO_2 because of the wider transmission window of Si.

5.2 Effect of the repetition rate in THz generation through two-color filamentation

Establishing a broadband, efficient and portable THz plasma source requires, as mentioned before, switching to laser oscillators without the presence of an amplifier. This will increase also the repetition rate of the source. Thus, studying the behavior of a plasma source when switching to higher repetition rates is essential and interesting. In 2013 Cheng et.al [3] reported that femtosecond laser pulses filamenting in various gases are shown to generate long-lived quasi-stationary cylindrical depressions or ‘holes’ in the gas density that gradually dissipate via thermal diffusion on a millisecond timescale. Thus, repetition rate of the driving

laser appears to be crucial. Next we will present some preliminary results of our current work on the dependence of the laser repetition rate to the THz emission though two color filamentation in air. We observe an increase in the THz signal reaching 77% with increasing repetition rate under the same laser pump energy.

5.2.1 Experimental setup

For the experimental realization we adopt the laser system that we used in the previous section. The tunability of the laser system regarding the repetition rate makes it ideal for the specific experiment. Again the laser beam is focused by a lens to generate the THz plasma source after is passed through a 50 μm BBO crystal. The pulse energy was kept constant at 150 μJ for all the studied repetition rates. The THz beam is guided by two off-axis parabolic mirrors to a 1 mm ZnTe crystal for electro-optic detection. At the same time a CCD camera is used to record the fluorescence images of the plasmas in each case adjusting the exposure time so that the same amount of pulses are captured for each repetition rate. Fluorescence images were analyzed in order to correlate the plasma dependence with the different repetition rates and with the THz signal.

5.2.2 Results

Nine different repetition rates were used, 250 Hz, 500 Hz, 1 kHz, 4 kHz, 6 kHz, 8 kHz, 10 kHz, 20 kHz and 25 kHz. In Fig.5.7 are shown the THz electric fields recorded as a function of the repetition rate along with their corresponding spectra. We can see that increasing the repetition rate results in an increase in the THz signal that gradually saturates. This becomes

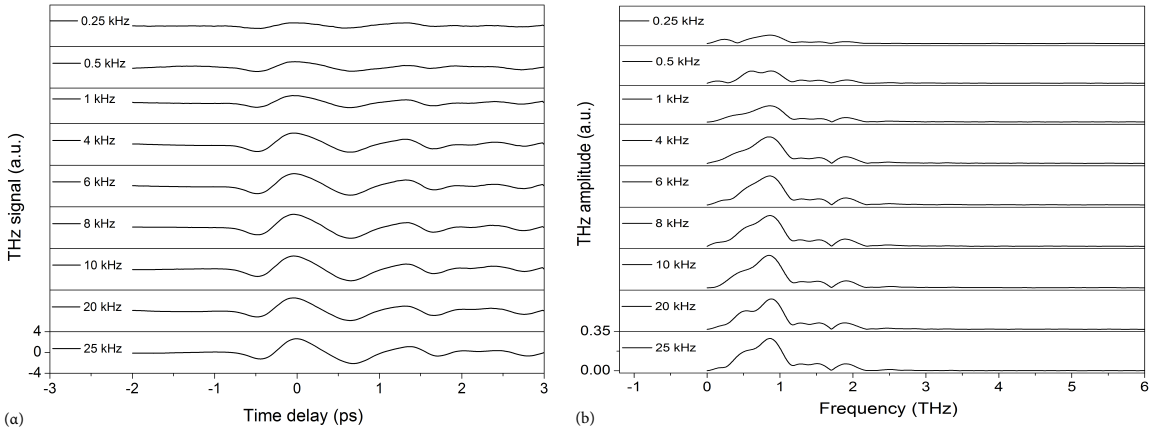

Fig. 5.7 THz electric fields (a) for various laser repetition rates together with their corresponding spectra (b).

more obvious in Fig.5.8 where one can see the normalized to the maximum value integrated THz amplitude versus the repetition rate. Saturation indeed occurs at 8 kHz. We can see an impressive increase on the THz generation reaching the value of 77% for the same pulse energy. Correlating this behavior with the plasma distribution dependence on the repetition rate is going to explain the above observations.

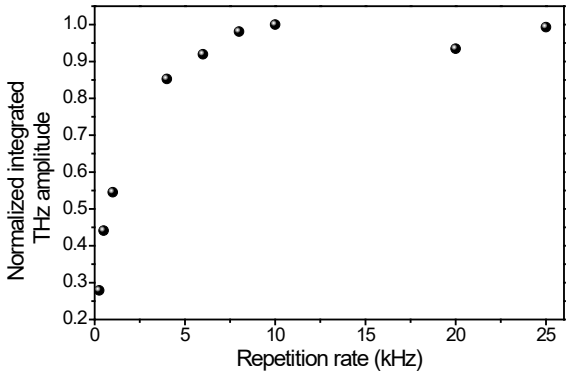

Fig. 5.8 Normalized integrated THz amplitude as a dependence of laser repetition rate.

Fig.5.9 shows the fluorescence distribution emission for all the studied cases, along with their corresponding cross section profiles. Although fluorescence distribution cannot be used to directly measure the plasma density, it can be used as an indicator when comparing the distributions for the various repetition rates. We can see that increasing the repetition rate

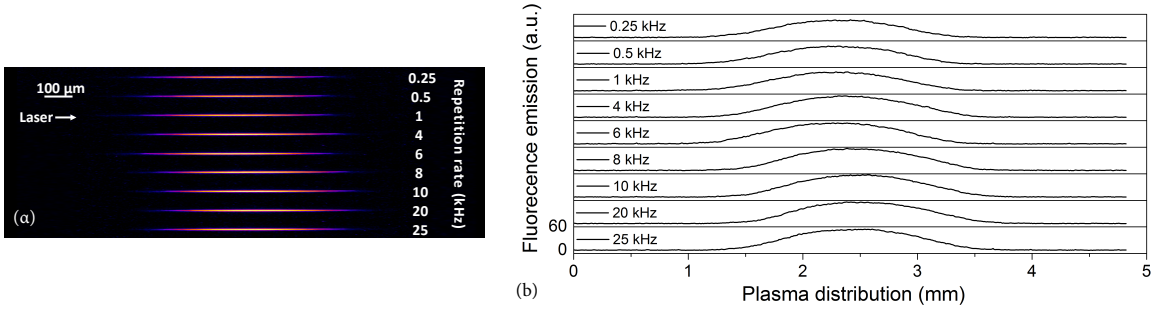

Fig. 5.9 Fluorescence images of plasmas generated using a lens with focal length of 125 mm (a) and their cross section profiles (b) for all the repetition rates used.

results in an increase in the fluorescence accompanied with an increase in the length of the plasma channel. Moreover, we observe that the plasma channel shifts back and forward. In ref. [3], authors reported a shift of the plasma channel away from the lens and they explain this as follows. The effect of the long timescale gas density hole left by a pulse or sequence of pulses is to reduce the index of refraction near the center of the beam seen by the next

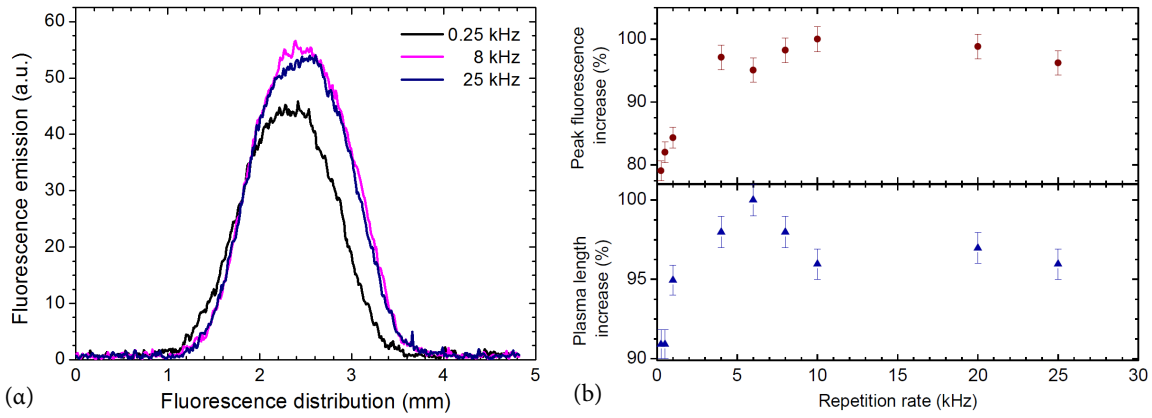

Fig. 5.10 Normalized integrated fluorescence of plasmas (a), plasma length (b) and peak fluorescence (c) versus laser repetition rate.

pulse in the sequence. This will have a defocusing effect on the next pulse and depends of course on the repetition rate. Moreover, their study was focused on repetition rates up to 1 kHz, this effect is expected to become more prominent for even higher repetition rates.

Normally, this implies that increasing the repetition rate should result in a more prominent defocusing of the laser beam. One expects that plasma density should also drop due to the same effect. But our experimental observations are presenting an opposite behavior. Fig.5.10 (a) shows the integrated fluorescence of plasma distributions normalized to the maximum value versus repetition rate. It is clear that there is an increase in the overall fluorescence that follows the THz increase.

Both fluorescence and the THz signal begin to saturate at 8 kHz allowing us to correlate the observed THz enhancement to the increase in the plasma length and density. Fig.5.10 (b) shows peak fluorescence and fluorescence length at FWHM. As we can see both increase and saturate with the repetition rate and according to our interference model described in

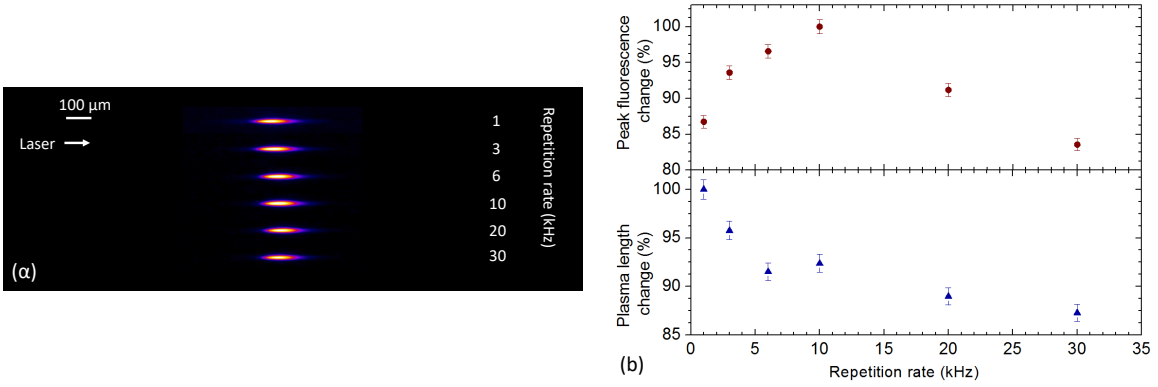

Fig. 5.11 Fluorescence images of plasmas generated using a lens with focal length of 50 mm (a) and normalized integrated fluorescence of plasmas (b).

Chapter 2 both of these parameters enhance THz emission.

An interesting result of this study is how this phenomenon scales with the focusing conditions of the pump pulse. The previous results were obtained for a focusing lens with focal length of 125 mm resulting in a plasma channel of a couple of millimeters. Performing experiments with a shorter focal length lens of 50 mm and analyzing the corresponding fluorescence images an opposite behavior is observed. The repetition rates used this time were 1, 3, 6, 10, 20 and 30 kHz. Fig.5.11 (a) shows fluorescence images of the plasma distribution for that case. We can see that the plasma length is almost ten times smaller that the previous case reaching 200 microns. In Fig.5.11 (b) becomes obvious that increasing the repetition rate, results in a more expected behavior of the integrated fluorescence decrease. Unfortunately for this case we do not have corresponding THz signals. Nevertheless, we expect that the THz emission would also be suppressed with this focusing geometry.

5.2.3 Current and future plans

At this point we are performing theoretical simulations that will allow us to better understand and explain these observations. We need to mention that although these long timescale gas density dynamics were investigated before, our experimental conditions are very different. We believe that this work can open up new prospects towards miniaturizing THz sources based on filamentation in gases. Emission form micro-plasmas in air is very low and being able to efficiently enhance that emission by using laser pulses with higher repetition rates could be extremely beneficial.

References

[1] Y. S. You, T. I. Oh, and K. Y. Kim. Off-Axis Phase-Matched Terahertz Emission from Two-Color Laser-Induced Plasma Filaments. *Physical Review Letters*, 109(18):183902, oct 2012.

[2] Fabrizio Buccheri and Xi-Cheng Zhang. Terahertz emission from laser-induced microplasma in ambient air. *Optica*, 2(4):366–369, 2015.

[3] Y H Cheng, J K Wahlstrand, N Jhajj, and H M Milchberg. The effect of long timescale gas dynamics on femtosecond filamentation. *Optics Express*, 21(4):4740–4751, 2013.